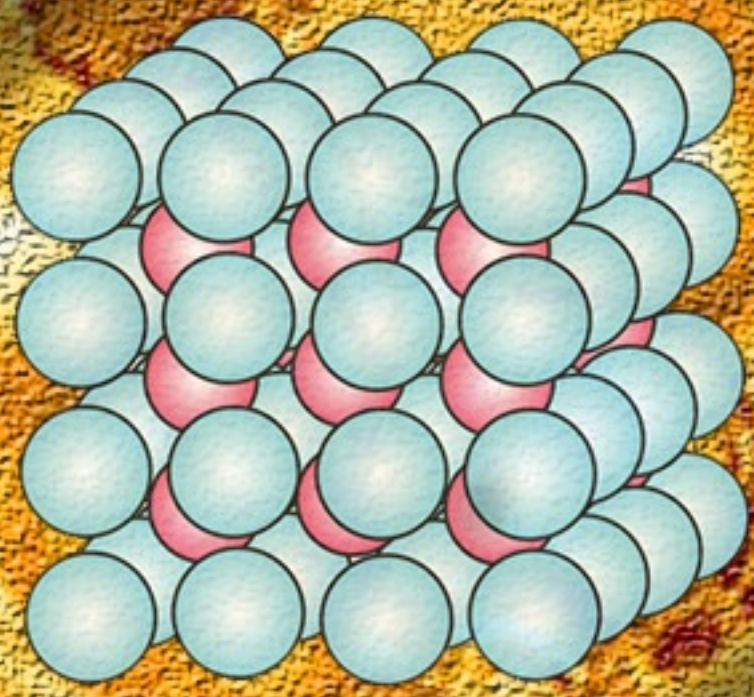
SCIENTIFIC TECHNICAL JOURNAL

"MATERIAL SCIENCE"



„NONEQUILIBRIUM PHASE TRANSFORMATIONS"

ISSUE 4/2016

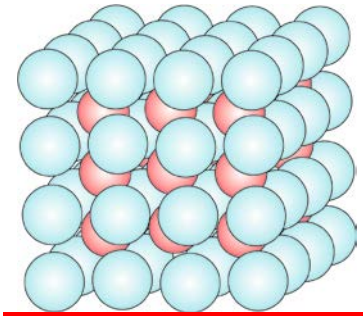
YEAR II, ISSN PRINT 2367-749X, ISSN WEB 2534-8477

PUBLISHER: SCIENTICIC TECHNICAL UNION OF MECHANICAL ENGINEERING

108 Rakovski str., 1000 Sofia, Bulgaria

tel./fax (+359 2) 986 22 40, tel. (+359 2) 987 72 90, www.mech-ing.com

office@stumejournals.com, www.stumejournals.com



INTERNATIONAL JOURNAL

MATERIALS SCIENCE. NON-EQUILIBRIUM PHASE TRANSFORMATIONS

PUBLISHER:

SCIENTIFIC TECHNICAL UNION OF MECHANICAL ENGINEERING

108, Rakovski Str., 1000 Sofia, Bulgaria
tel. (+359 2) 987 72 90,
tel./fax (+359 2) 986 22 40,
office@stumejournals.com

ISSN PRINT 2367-749X, ISSN WEB 2534-8477
YEAR II, ISSUE 4 / 2016

EDITORIAL BOARD

CHIEF EDITOR
Prof. Dimitar Stavrev – Bulgaria

DEPUTY EDITOR:
Dr. Alexander Krugljakow, Germany
Prof. Sergey Dobatkin, Russia
Prof. Sergey Nikulin, Russia
Prof. Victor Anchev, Bulgaria

RESPONSIBLE SECRETARY:
Assoc. Prof. Tsanka Dikova, Bulgaria

MEMBERS:

Prof. Adel Mahmud, Iraq
Prof. Anna Proikova, Bulgaria
Prof. Bekir Sami Yilbas, Saudi Arabia
Prof. Dermot Brabazon, Ireland
Prof. Dipten Misra, India
Assoc. Prof.Eugeniy Grigoriev, Russia
Prof. F. W. Travis, United Kingdom
Prof. Gennagiy Bagluk, Ukraine
Assoc. Prof. Ibrahim E.Saklakoglu, Turkey
Prof. Iis Sopyan, Malaysia
Prof. Ivan Parshorov, Bulgaria
Prof. Ivanja Markova, Bulgaria
Prof. Janez Grum, Slovenia
Prof. Jens Bergstrom, Sweden
Prof. Leszek Dobrzanski, Poland
Prof. Ludmila Kaputkina, Russia
Prof. Nikolai Dulgerov, Bulgaria
Prof. Omer Keles, Turkey
Prof. Plamen Danev, Bulgaria
Prof. Rui Vilar, Portugal
Prof. Rusko Shishkov, Bulgaria
Prof. Saleem Hashmi, Ireland
Dr. Sefika Kasman, Turkey
Prof. Seiji Katayama, Japan
Prof. Souren Mitra, India
Dr. Sumsun Naher, United Kingdom
Prof. Svetlana Gubenko, Ukraine
Prof. Sveto Cvetkovski, Macedonia
Prof. Ventsislav Toshkov, Bulgaria
Prof. Yovka Dragieva, Bulgaria

C O N T E N T S

THE INFLUENCE OF THE HEATING RATE IN THE PROCESS OF SPARK-PLASMA SINTERING ON THE KINETICS OF COMPACTION, STRUCTURE FORMATION AND PROPERTIES OF THE MATERIALS OF Fe – Ti – C – B SYSTEM
Sizonenko Olga Nikolaevna, DrSc Eng., Professor, Zaichenko Andrey Dmitrievich, PhD Eng., Pristash Nikolay Sergeevich, Torpakov Andrey Sergeevich 3

MECHANOCHEMICALLY INDUCED PHASE TRANSFORMATION AND LEACHING OF DECAY PRODUCTS FROM U(IV, VI) OXIDE
Assoc. Prof. Dr. Kovacheva P. G., Prof. D. Sc. Todorovsky D. S. 6

HARDENING LOW CARBON STEEL 10 BY USING OF THERMAL-CYCLIC DEFORMATION AND SUBSEQUENT HEAT TREATMENT
D.Sc. (Eng.), Prof. Prudnikov A., D.Sc. (Eng.), Prof. Popova M., Ph.D. student Prudnikov V. 10

PRODUCTION OF HIGH SOLID CONTENT POLYMER/YSZ COMPOSITES AND FREE FORM YSZ FIBERS
M.Sc. D. Yilmaz Cakta, Assoc. Prof. Dr. B. Ozkal 14

THE EXPLOSIVE CRYSTALLIZATION OF AMORPHOUS MICROWIRE
Borisenko I. Yu., Tulin V. A. 18

RESEARCH OF PHASE TRANSFORMATION PRODUCTS IN HIGH STRENGTH STEELS BY ELECTRON BACKSCATTER DIFFRACTION (EBSD)
E.A. Yashina, A.A. Zisman, D.Sc., S.N. Petrov, Ph.D. 22

SYNTHESIS AND CHARACTERIZATION OF ZnO NANOCRYSTALS IN STARCH MATRIX
Assos. Prof. Dr. Vasileva P. 26

ANALYSIS OF THE EUTECTOID TRANSFORMATION INTO CARBON STEEL ON THE BASIS OF POSITIONS OF NON-EQUILIBRIUM THERMODYNAMICS
Dr. S. V. Bobyr, Prof. V. I. Bol'shakov, S.A. Sharfnadel 30

FORMATION OF COMPOSITE STRUCTURES BASED ON TETRAGONAL ZIRCONIA DOPED BY D-ELEMENTS OF I GROUP
Ass. Prof. Dr. Gorban O., M.Sc. Kharchenko M., M.Sc. Bryukhanova I.I., Ass. Prof. Dr Gorban S., M.Sc. E. Sinelnikova 34

THERMAL EXPANSION OF CARBON MATERIAL FOR SUPERCAPACITOR ELECTRODS
Dr.Sc. T. Kompan, Dipl. Ing. N. Pukhov 38

FORMATION OF STRUCTURE IN THE TINIHF SURFACE LAYERS WITH THE ASSESSMENT OF THEIR DURABILITY
Conf. dr. Rusinov P.O., Prof. dr. Blednova Zh.M. 41

STRUCTURE AND PROPERTIES HARD ALLOYS T5K10 WITH BORIDE COATINGS FORMED IN A MAGNETIC FIELD
Prof. Dr. Chernega S., Poliakov I., Grinenko E., Krasovskiy M. 45

SPARK PLASMA SINTERING THE COMPOSITES OF BIMODAL COPPER POWDERS
Prof. Grigoryev E. PhD., P.G. Nefedova E. 49

REGULARITIES OF INFLUENCE OF NICKEL AND CHROMIUM ON STRUCTURE FORMATION OF ELECTRODEPOSITED IRON
Ph. D. Kolesnyk Ie.V., Dr.Sc. (Eng.) Bagliuk G.A. 52

THE EFFECT OF FLUORIDE ON CORROSION BEHAVIOUR OF AUSTENITIC STAINLESS STEEL
RNDr. Viera Zatkalíková, PhD., Ing. Lenka Markovičová, PhD., Ing. Monika Oravcová 56

THE INFLUENCE OF THE HEATING RATE IN THE PROCESS OF SPARK-PLASMA SINTERING ON THE KINETICS OF COMPACTION, STRUCTURE FORMATION AND PROPERTIES OF THE MATERIALS OF Fe – Ti – C – B SYSTEM

Sizonenko Olga Nikolaevna, DrSc Eng., Professor, Zaichenko Andrey Dmitrievich, PhD Eng., Pristash Nikolay Sergeevich, Torpakov Andrey Sergeevich
Institute of Pulse Processes and Technologies of NAS of Ukraine – Mykolaiv, Ukraine, E-mail: sizonenko43@rambler.ru

Abstract: Regularities of the influence of spark plasma sintering heating rate on the structure and properties of dispersion-strengthened materials based on Fe – Ti – C – (B) system are studied. Increasing heating rate of the samples from 10 °C/s to 20 °C/s induced by increasing current rise rate leads to decrease the average grain size in the material matrix of the Fe – Ti – C – B system from 2.5 to 1.5 microns. This allows to increase hardness from 48 HRC up to 70 HRC and wear resistance 7 times compared to R6M5 (full analog of HSS M2) steel during SPS consolidation in the mode with a heating rate of 20 °C/s and isothermal exposure 1100 °C for 180 s.

Keywords: spark plasma sintering, high voltage electric discharge, consolidation, hardness, wear resistance, powder, carbide steel

1. Introduction

The contemporary industry needs the structural materials with high hardness and wear resistance which could replace the costly tungsten-containing materials. This can be achieved by creating composite materials with heterogeneous structure being a plastic metal matrix with hard inclusions. Such materials include metal-matrix composites, including carbide steels, which are obtained by powder metallurgy methods [1 – 4]. The Institute of Pulse Processes and Technologies of NAS of Ukraine (IPPT NASU) developed the technology of producing carbide steels of the Fe – Ti – C – B system with levels of hardness and wear resistance similar to tungsten-containing alloys. Improved physical and mechanical characteristics were obtained by changing the dispersion and phase composition of the initial powders using the high-voltage electric discharge (HED) treatment in the hydrocarbon liquid and their subsequent spark-plasma sintering (SPS) [5 – 7].

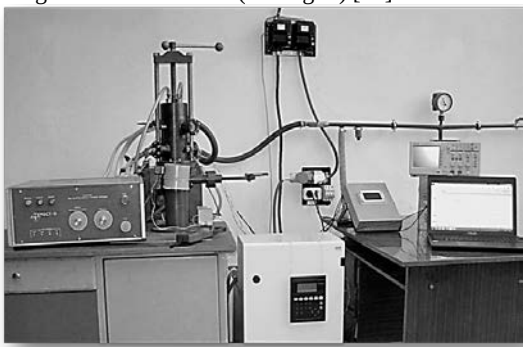
2. Problem discussion

It is known that physical and mechanical and functional properties of powder compacts largely depend on the porosity and grain structure [8], and that SPS provides rapid consolidation of powder materials and in many cases restricts the grain growth compared to conventional sintering [9]. Therefore, the study of the influence of the heating rate of SPS consolidation on the structure and properties of dispersion-strengthened materials based on Fe – Ti – C – (B) system is an urgent task.

Objective of this paper is to establish regularities of the influence of SPS heating rate on the structure and properties of dispersion-strengthened materials based on Fe – Ti – C – (B) system.

3. Objective and research methodologies

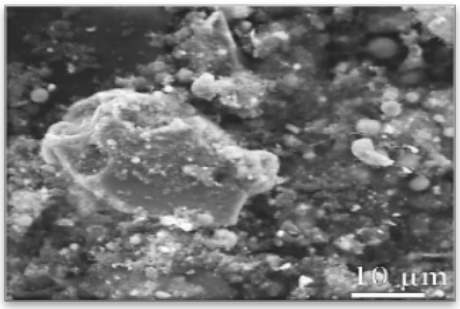
The SPS was carried out using experimental complex, designed at IPPT NASU (see Fig. 1) [10].



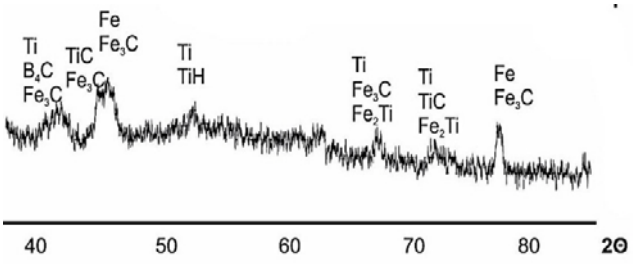
The atmosphere	Vacuum 10^{-4} MPa
The matrix material	Graphite MPG-3
Axial pressure	60 MPa
The amplitude of the superposition	1.1 kA

Fig. 1. *SPS complex and its parameters*

The mixture of powders of initial mass composition of 75% Fe – 20% Ti – 5% B_4C was chosen as the charge for sintering to be treated by the HED with a specific energy of 6.25 MJ/kg, which provided the content of the strengthening phase to 25% sized from 100 nm to 600 nm and an average metal-matrix particle diameter of ~ 15 μm (see Fig. 2) [6, 7].



a



b

Fig. 2. *Electron micrograph ×1700 (a) and the phase composition (b) of the charge of Fe – Ti – C – B system*

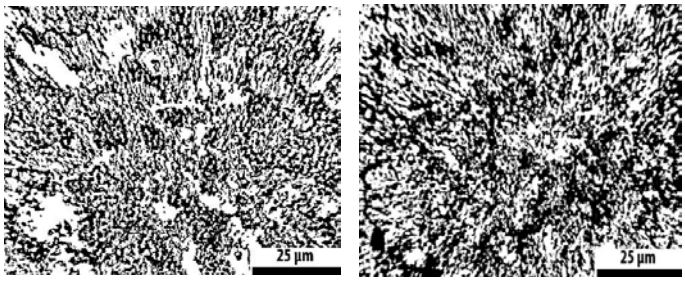
Consolidation was carried out at a heating rate of 10 °C/s at a temperature of isothermal aging of 1100 °C, holding time τ = 180 s, cooling rate 10 °C/s. The heating rate was varied in the range of 10 °C/s to 20 °C/C by increasing the current strength amplitude rise from 14 A/s to 30 A/s.

The experimental analysis of changes in the structure of the consolidated compacts was carried out by means of computer metallography according to DSTU ISO 643:2009 using the Biolam-I optical microscope and ImageJ software. Phase analysis was carried out on DRON-3 diffractometer according to ref. [11].

Hardness of samples was measured according to ISO 6508-1:2013. Wear resistance was investigated by SMC-2 friction machine based on the "roller-pad" pattern. The counter-body was the 1A1 diamond grinding wheel with grain size of AC80/63. The results were compared with test results of the sample of steel R6M5 (GOST 19265-73, full analog of HSS M2 steel).

The average grain size of the matrix of the Fe – Ti – C – B system after HED treatment is ~ 0.5 μm. In the process of SPS at heating rate of 10 °C/s its average size increased to ~2.5 μm. Increasing the heating rate to 20 °C/s allowed to reduce the average grain size of the matrix after sintering to ~1.5 μm.

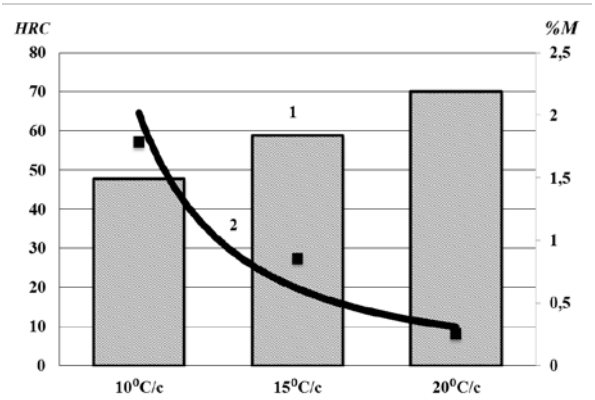
The increase of the heating rate of SPS also led to increasing hardness from 48 HRC up to 70 HRC and wear resistance; the mass loss for the samples consolidated with a heating rate of 20 °C/s was 0.2 %, which is 7 times lower than that of samples of R6M5 (full analog of HSS M2) steel (hardness of 60 HRC). It is assumed that this is due to the decay of residual boron carbide and occurrence of the carbide and boride formation process during heating, which is characterized by heat release, as evidenced by the heating curves obtained during the experiment (see Fig. 4, b).



a b

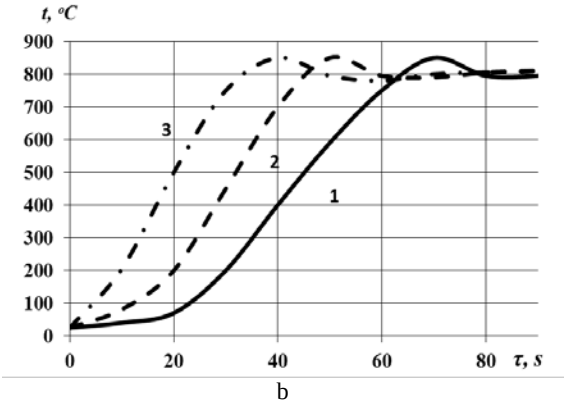
a – 10 °C/s; 2 – 20 °C/s;

Fig. 3. *Optical microphotographs of samples (×450) consolidated with different heating rates during SPS*



1 – hardness; 2 – mass loss

a

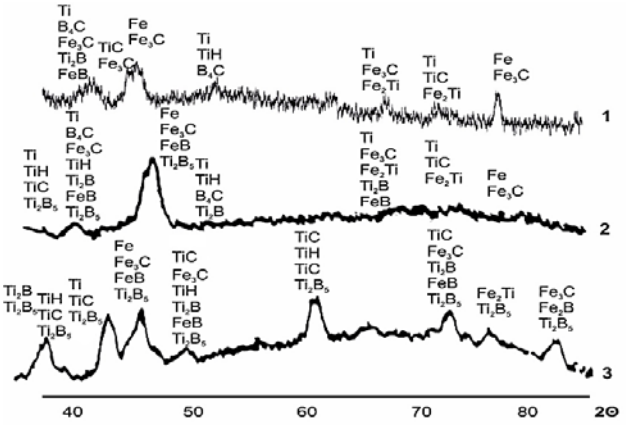


b

1 – 10 °C/s; 1 – 15 °C/s; 1 – 20 °C/s

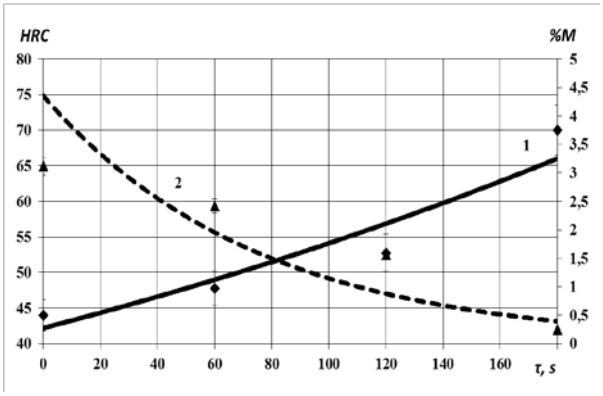
Fig. 4. *Changes in mechanical characteristics (a) and heating curves (b) of the consolidated samples*

Additionally, a set of experiments on the consolidation of powder mixture of Fe – Ti – C – B system with a heating rate of 20 °C/s was conducted to achieve a temperature of 1100 °C and subsequent holding from 0 to 180 s with a step of 60 s. The analysis of experimental data allowed us to establish that with the increasing holding time to 180 s the content of the boride phase of source metals is increasing in the composition of the sample (see Fig. 5), which leads to increased hardness and wear resistance (see Fig. 6).



1 – 0 s; 2 – 120 s; 3 – 180 s

Fig. 5. *X-ray diffractograms of samples of the Fe – Ti – C – B system consolidated with different holding time at a heating rate of 20 °C/s*



1 – change of hardness; 2 – mass loss

Fig. 6. *Hardness and mass loss of samples of the Fe – Ti – C – B system consolidated at heating rate of 20 °C/s vs. holding time*

3. Conclusions

1. It is established by experiments that increasing heating rate of the samples from 10 °C/s to 20 °C/s induced by increasing current rise rate allows to decrease the average grain size in the material matrix of the Fe – Ti – C – B system from 2.5 to 1.5 microns.

2. It is established that increasing heating rate from 10 °C/s to 20 °C/s affects the flow of diffusion processes in the material during SPS, i.e. slowing them, and helps to increase hardness from 48 HRC up to 70 HRC and wear resistance 7 times compared to R6M5 (full analog of HSS M2) steel during SPS consolidation in the mode with a heating rate of 20 °C/s and isothermal exposure 1100 °C for 180 s, which is connected with intensification of carbide and boride formation processes.

References

1. Panov, V. S. Technology and properties of sintered hard alloys and products from them / V. S. Panov, A. M. Chuvilin. – M.: MISIS, 2001, 428 p. (Rus)

2. Babich, B. N. Metallic powders and powder materials: reference book / B. N. Babich, E. V. Vershinina, V. A. Glebov. – M.: EKOMET, 2005, 520 p. (Rus)

3. Baglyuk, G. A. Features of the structure of hot formed carbide steel "quick-cutting steel – Ti carbide" / G. A. Baluk, I.D. Martyukhin, T. M., Pavligo, G. G. Serdyuk, V. M. Tkach in Powder metallurgy (2009), No. 1/2. (Rus)

4. Gurevich, Yu. G., Narva, V. K., Frage N. R. Carbide steels. – M.: Metallurgy, 1988, 144 p.

5. Zaichenko, A. D. Improvement of the process of electrodischarge treatment of charge and spark-plasma sintering for obtaining highly wear-resistant carbide steels: abstract of dissertation for the PhD degree: specialty 05.16.06 “Powder Metallurgy and Composition Materials” / A. D. Zaichenko. – Kyiv, 2015, 24 p. (Ukr)

6. Sizonenko, O. N. Features of electric discharge treatment of mixtures based on Fe and Ti powders of different composition / O. N. Sizonenko, N. S. Pristash, E. I. Taftai, A. S. Torpakov, A. D. Zaichenko, E. V. Lipyan, A. A. Zhdanov // Visnyk ukrainskogo materialoznavchogo tovarystva. Issue No. 6. – Kyiv: Ukrainske materialoznavche tovarystvo, 2013, P. 104 -111 (Rus)

7. Sizonenko, O. N. The influence of the high-voltage treatment of the powder compositions of the Fe-Ti-C and Fe-Ti-B-C composition on the change in their electrical resistance / O. N. Sizonenko, N. S. Pristash // Proceedings of I. N. Frantsevich Institute of Problems of Materials Science of NAS of Ukraine. Series “Composite, lamellar and graded materials and coatings”. Electrical contacts and electrodes. – Kiev: I. N. Frantsevich Institute of Problems of Materials Science of NAS of Ukraine, 2014, P. 129 – 133. (Rus)

8. Kang S.-J. L. Sintering. Densification, Grain Growth and Microstructure. – Amsterdam: Elsevier, 2005, 265 p.

9. Grigoriev E. G. Electropulse technology of forming the materials from powders / E. G. Grigoriev, B. A. Kalin // Tutorial. Moscow: MIFI, 2008, 152 p.

10. Pat. 101575 Ukraine, 12006.01 IPC B22F 3/14, B22F 3/105, B30B 15/02. Device for spark-plasma sintering of powders / Sizonenko O. N., Ivlev A. I., Raichenko O. I. [et al.], No. a201200957; Appl. 30.01.2012; publ. 10.04.2013, bull. No. 7. (Rus)

11. Technical description. The general purpose diffractometer DRON-3. – Leningrad: Burevestnik, 1983, 376 p. (Rus)

MECHANOCHEMICALLY INDUCED PHASE TRANSFORMATION AND LEACHING OF DECAY PRODUCTS FROM U(IV, VI) OXIDE

МЕХАНОХИМИЧНО-ИНДУЦИРАНИ ФАЗОВО ПРЕВРЪЩАНЕ И ИЗВЛИЧАНЕ НА ПРОДУКТИТЕ НА РАДИОАКТИВНО РАЗПАДАНЕ ОТ U(IV, VI) ОКСИД

Assoc. Prof. Dr. Kovacheva P. G., Prof. D. Sc. Todorovsky D. S.
Faculty of Chemistry and Pharmacy – St. Kliment Ohridski University of Sofia, Bulgaria

nhpk@wmail.chem.uni-sofia.bg

Abstract: *Depleted U_3O_8 was mechanically activated in suspension with tributyl phosphate (TBP), trioctylamine (TOA) and ethylenglycolmonomethylether (EGME) in planetary ball mill with stainless steel vessels and balls. X-ray diffractograms and IR spectra of the activated solid samples were taken. The radioactivities of ^{238}U and ^{234}Th in the leaching solutions were determined by α/β liquid scintillation spectrometry. The reduction degree of the oxide, the mean crystallite size of U_3O_8 and U_3O_7 and the leaching of ^{238}U and ^{234}Th as a result of the mechanoactivation were determined. Higher degree of ^{238}U and ^{234}Th leaching was achieved when mechanoactivation with TBP was performed. No leaching of ^{238}U daughter product (^{234}Th) proceeded at mechanoactivation with TOA and EGME. The role of the solvents complexation ability, milling induced increase of crystal defect concentration and $UO_2 – ThO_2$ solid solution formation is discussed. Further studies have to be made to elucidate the potential of the applied approach as a step in spent nuclear fuel processing.*

Keywords: URANIUM OXIDES, THORIUM, MECHANOACTIVATION, EXTRACTION, XRD, IR-SPECTROSCOPY, LIQUID SCINTILLATION SPECTROMETRY

1. Introduction

The application of solvent extraction is recognized for a long time to play important role in actinides recovery and purification, radionuclide production, preparation of the reactor materials and other aspects of the nuclear technology [1]. Plenty of scientific efforts are spent to develop solvent extraction processes that display selectivity, simplicity and speed.

The effects of the mechanoactivation on the compounds of 5f-elements were reported in series of papers [2-9]. It was shown that uranium oxides and salts are comparatively stable upon mechanical treatment. The main effect of the mechanoactivation on the U_3O_8 and UO_3 is the reduction of U(VI) with the formation of UO_2, U_3O_7 and U_2O_5; the degree of reduction is found to depend on the treatment conditions [2-4]. Mechanochemical synthesis of $NO[UO_2(NO_3)_3]$ is proven in the course of $UO_2(NO_3)_2.6H_2O$ milling [5]. Mixed U-Th [6] and U-Ce [7] oxides are prepared by sol-gel method followed by mechanoactivation and a solid $(U,Pu)O_2$ solution is obtained by co-milling of UO_2 and PuO_2 [8].

U-leaching from $UO_2(CH_3COO)_2.2H_2O$, due to transformation of bidentate bonding of the CH_3COO^- in monodentate one in the course of mechanical activation with toluene and benzene was registered [9]. Of special interest are the results for the influence of the high-energy ball milling of U_3O_8 in air and in suspension (with thionyltrifluoroacetone, TTA) on the migration of ^{238}U and its daughter product ^{234}Th [2].

Taking into account the wide and successful application of tributyl phosphate (TBP) [10], trioctylamine (TOA) [11, 12] and ethers and ketones [1, 13] in the radionuclide extraction for the reactor technology, TBP, TOA and ethylenglycolmonomethylether (EGME) were used in the present paper as media to investigate the degree of leaching of ^{238}U and its daughter product ^{234}Th from U(IV, VI) oxide by mechanochemical activation in suspension. The structural changes and the degree of reduction of the initial oxide were also studied.

2. Experimental

Approx. 2 g of U_3O_8 (Koch-Light, depleted, ^{235}U content 0.375%; it was shown that the product is a mixture of α-U_3O_8 and U_3O_7 [3] and has to be described as U_3O_{8-x}) were mechanically activated in stainless steel vessels in suspension with 5 ml TBP or TOA or EGME in planetary ball mill (Pulverisette 5, Fritch).

Stainless steel vessels of 80 cm^3 volume and balls from the same material (7-15 mm in diameter) were used. The activation was performed for 5 h at mechanical load of 12g.

After the mechanoactivation 70-80 cm^3 benzene (p.a.) was added to each suspension and the latter was filtered (fine porous filter). The solid phase was rinsed with benzene (5 times with total volume of 20 cm^3) and filtered again. The joint filtrates were analyzed by IR- and liquid scintillation spectrometry.

The X-ray diffractograms of the activated solid samples were taken by a powder diffractometer Siemens D500 using CuK_α radiation filtered by a secondary monochromator (40 kV, 30 mA, 0.05^o 2Θ/2 s for the interval 5–45^o 2Θ. Relative content and mean crystallite size of U_3O_8 and U_3O_7 were determined from XRD pattern using the program POWDER CELL for Windows, version 2.4 [14].

The IR spectra in the range 2500-400 cm^{-1} were recorded by a Bruker spectrometer in capillary layer.

The radioactivity of ^{238}U and ^{234}Th in the leaching solutions were determined by α/β liquid scintillation spectrometry (LSC) measuring the alpha-activity of U–isotopes and beta-activity of ^{234}Th via ^{234m}Pa in optimized regions of interest. The radiometric procedure was performed by α/β liquid scintillation spectrometer Tricarb-2550 TR/LL, using scintillation cocktail Packard Ultima Gold AB. The quench level of each sample was determined by the ^{133}Ba external standard of the spectrometer before each counting. All measured activities were recalculated to the moment of separation of leaching solution from the residue.

3. Results and Discussion

3.1. Phase transformation, crystallites size

The mechanoactivation of U_3O_{8-x} in suspension with the three abovementioned organic reagents leads to the clearly expressed reduction process, already observed in different degree in all the experiments including mechanochemical stress of U_3O_{8-x} [2-4].

The X-ray powder diffractogrammes of the initial product and of the mechanoactivated samples are presented in Fig. 1a-d. The quantitative changes, occurred as a result of the mechanoactivation process, are shown in Table 1.

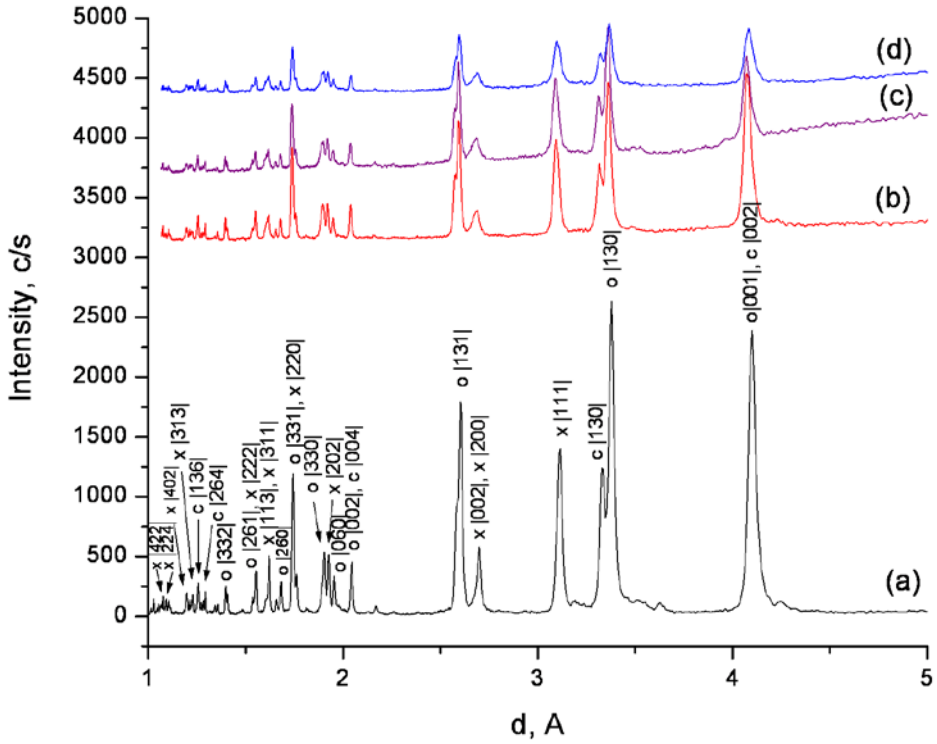


Fig. 1 *X-ray diffractogrammes of U_3O_8 before (a) and after 5 h milling in stainless steel vessel in TBP (b), TOA (c) and EGME (d). Miller índices are shown: o - α-U_3O_8, c - β-U_3O_8, x - U_3O_7.*

The data, presented in Table 1 show that the highest degree of reduction is reached when mechanoactivation in suspension with EGME is performed.

Table 1: *Relative content of U_3O_8 and U_3O_7, crystallites sizes of the U_3O_{8-x} and ^{238}U and ^{234}Th leaching*

Sample	U_3O_{8-x} (fresh)	Mechanoactivation		
		U_3O_{8-x}+ TBP	U_3O_{8-x}+ TOA	U_3O_{8-x}+ EGME
Content, %:				
U_3O_8	81.4	72.8	67.3	63.3
U_3O_7	18.6	27.1	32.7	36.7
U_3O_8/U_3O_7	4.4	2.7	2.1	1.7
Crystalite size, nm				
U_3O_8	51	46	41	34
U_3O_7	83	35	59	18
Leached, g/g U_3O_8				
^{238}U		7.0×10^{-2}	1.9×10^{-3}	$<1.6\times10^{-5}$
^{234}Th		5.5×10^{-14}	$<3.5\times10^{-17}$	$<3.5\times10^{-17}$

The reduction process can be explained by the triboemission of electrons, taking place during the high-energy ball milling. The low specific electroconductivity of the reaction media prevents their dissemination within its volume. They stay in close proximity of the solid substance and can be easily accepted by the oxidized form [4]. This hypothesis is supported by the data for the dielectric constant of the studied media. Their values for $C_6H_5CH_3$ and CCl_4 are rather close (2.328 and 2.238) and the reduction degrees are similar (100%, 93.4%, respectively [4]. The constant of TTA is higher (≈7 [15]) and the reduction degree is lower.

It is worth to mention that the order of increase of the reduction degree in the different media is opposite to the order of increase of the degree of ^{238}U and ^{234}Th leaching from the matrix. However compared to the result for the treatment of U_3O_8 at the same conditions in air, CCl_4 and $C_6H_5CH_3$ (in these media U_3O_8/U_3O_7 is 0.35, 0.07 and 0, respectively [4]), the reduction resulted in the milling in suspension in the investigated complexing agents is, in fact, suppressed as far as the above mentioned ratio in the present study is significantly higher (1.7 - 2.7, Table 1) for all the samples.

Decrease of the particle size of both U_3O_8 and U_3O_7, provoked by the mechanochemical treatment is observed for all the samples. The effect is stronger revealed for the U_3O_7 phase - the new formed particles, result of reduction and the respective phase transformation, have smaller crystallites. As a tendency, the decrease of the crystallites size follows the increase of the reduction degree. These observations are in agreement with the data for the samples milled in CCl_4 and $C_6H_5CH_3$ [4].

3.2. Uranium and thorium leaching

The quantities of U and Th in the liquid phase were calculated on the basis of their radioactivity in the organic solutions, measured by LSC. The obtained results are presented in Tables 1, 2.

Table 2: *Leaching of ^{238}U and ^{234}Th*

Activation medium	Mass ratio $^{238}U/^{234}Th$, $n\times10^{11}$	Leached nuclide/ nuclide in the sample, %		Enrichment in Th of the extract
		^{238}U	^{234}Th	
TTA-stirring [2]	19±9	6.0	10.4	1.7
TTA [2]	4.4±1.2	9.8	74.1	7.6
TBP	12.7	8.3	21.6	2.6
TOA		0.22	$<1.4\times10^{-2}$	
EGME		<0.002	$<1.4\times10^{-2}$	

Significant leaching of ^{238}U (8.3% from the ^{238}U and almost 22% of ^{234}Th present in the solid matrix) is achieved as a result of the mechanochemical activation in suspension with TBP. Much smaller is the quantity of uranium, leached from U_3O_{8-x} by TOA and practically no ^{234}Th is found in the organic extract. Only traces

of uranium and no ^{234}Th are registered in EGME phase (Tables 1, 2).

The presence of UO_2^{2+} in the solutions of the activated media (TBP and TOA) in benzene can be observed on the IR spectra (Fig. 2a,b) with the appearance of the bands for υ_s(U-O) at 886 cm^{-1} (TBP) and 826 cm^{-1} (TOA) and for υ_{as}(U-O) at 932 cm^{-1} (TBP) and 938 cm^{-1} (TOA).

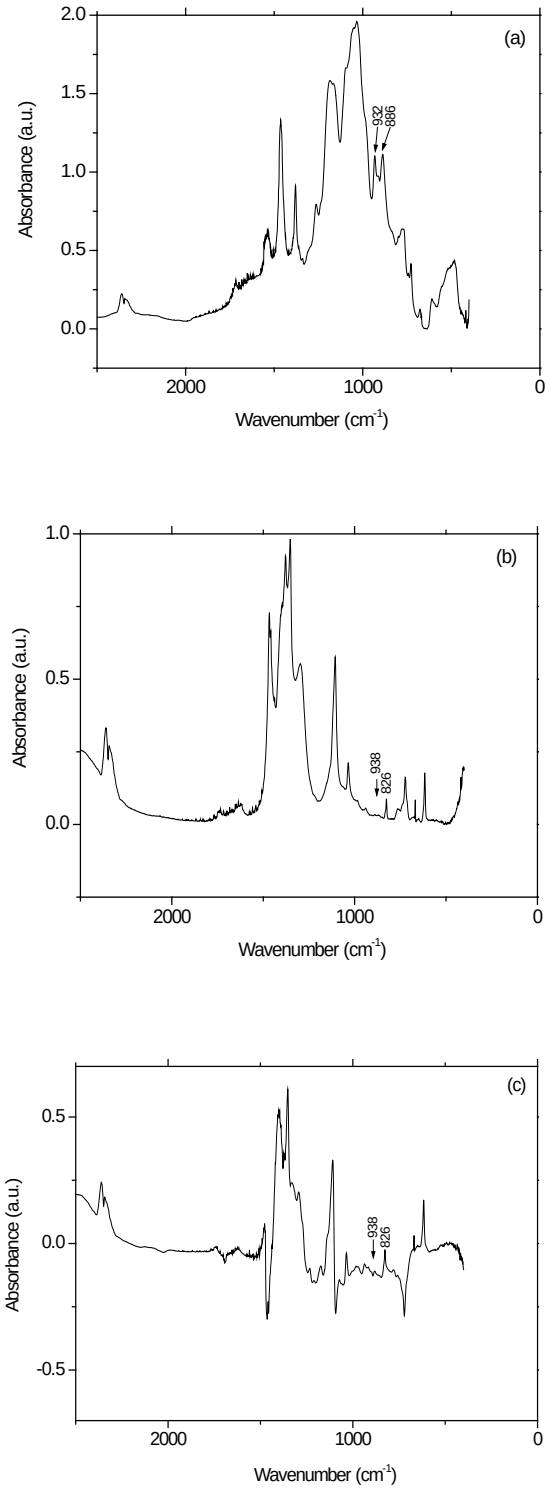


Fig. 2 *IR-spectra (2500 – 400 cm^{-1}) of the product obtained after milling of U_3O_{8-x} in stainless steel vessel in TBP (a) or TOA (b), dissolved in benzene, the spectrum (b) after subtraction of IR bands of TOA (c).*

Because of the lower uranium concentration in the TOA extract the abovementioned bands are very weak and better observable on the differential IR spectrum (Fig. 2c), where the IR bands of TOA are subtracted from the IR spectrum of the UO_2^{2+} - TOA phase.

Table 2 gives the possibility to compare the results obtained in the present work with those reported in [2] concerning U_3O_8 treatment with 0.25 M benzene solution of TTA.

3.2.1. Leaching of uranium

The leaching of a component is due to desorption of its particles from the crystal surface. The increase of the specific surface, due to mechanoactivation, will enhance the leaching of uranium which is readily available on the sample surface. Furthermore, the formation of insoluble U-TTA-complexes suppresses the extraction [15] and the continuous formation of new, fresh surface (result in the milling) partially overcomes this effect (for both uranium and thorium). These expectation are confirmed (for the TTA-system) by the data in Table 2.

The degrees of the uranium leaching (as percent from the uranium content in the milled sample) in the course of the mechanoactivation in suspensions in TTA and in TBP are rather similar. Much less U is leached as a result of the milling the oxide in TOA or EGME medium. The difference in the stability constants of the respective extractable forms could be a reason (or one of the reasons) for the difference in the leaching capability of the studied solvents. Indeed, regarding uranium, oxygen-containing solvents and especially ethers have high selectivity but rather low extraction ability; amines are effective extracting reagents for metals when they exist as anions and anionic complexes [15]. The leaching of the impurities (Th in the studied system) is closely connected with their migration from the bulk of the crystal to its surface as a result of diffusion, mainly via crystal defects. Producing a new surface and a wide spectrum of crystal defects, the mechanoactivation will enhance the diffusion and, respectively, the leaching of the Th. The results for TTA-system confirm this expectation.

3.2.2. Leaching of thorium

The most interesting result is the prevailing leaching of Th (in comparison with U) observed in non-activated and activated TTA- and activated TBP- systems. Factors that could be responsible for the easier leaching of Th are discussed in [2]: the higher energy of U-O bonds in U_3O_8 than of Th-O in ThO_2; the relaxation of Th recoil atoms as Th^{4+} in a highly disturbed zone; the higher value of the stability constant of Th complex with the studied reagent. These factors could explain the enrichment (comparatively low) of the TTA-extract obtained from non-activated U_3O_8 (Table 2).

It can be expected that the mechanoactivation will enhance preferable leaching of Th: (i) the disintegration of the solids during the milling goes preferably along the places with higher impurities concentration due to their weaker bonding with the matrix; (ii) the crystal defects (point defects and dislocations) are thermodynamically favourable places for the impurities, their concentration in these places increases and they diffuse through them to the crystal surface. The later effect was confirmed for a system, similar to the one studied in this paper in relation to the amount of the impurity (ultramicro amount of radiosulphur in ionic single crystal) [16]. The increase of the crystal defect concentration as a result of the mechanoactivation will make this mechanism rather important. The effect is already used in practice to enhance the extraction of valuable components from ores and other materials.

The significant difference in the Th leaching in the course of milling in TTA and in TBP (Table 2) is not surprising - the chelating agent TTA will be much more effective extracting agent than TBP, the later most probably forming less stable adducts with the extractable forms. Such an advantage of TTA will be more significant when extraction of the much less available impurity (Th) is concerned.

The two other studied complexing agents practically do not extract Th at conditions applied in the present work. In the same time they manifest highest (for the systems studied in this work) degree of reduction of uranium (Table 1). In [2] it was discussed and grounded a potential role of the mechanochemically induced solid solution formation⇄destruction processes taking place in the course of the mechanoactivation [17]. These processes are stronger expressed at milling in air but they can proceed in suspension, also. New-formed UO_2 can form solid solution UO_2-ThO_2. In the presence of strong complexing agents (TTA, TBP) the ThO_2 can be removed from the equilibrium and formation of solid solution will be less probable. TOA and EGME have not such ability, solid solution can be formed and Th^{4+} (stronger bonded in it, comparing to the bonding in U_3O_8 - ThO_2 system) will remain in the matrix.

4. Conclusion

The mechanical activation of U_3O_{8-x} in planetary ball mill in suspensions with TBP, TOA and EGME leads to:

- clearly pronounced reduction; the content of U_3O_7 increasing in the above mentioned order of media with, respectively, 46%, 76% and 97%, compared to the fresh product,
- decrease of the crystallite sizes of both the U_3O_8 (with 10%, 20% and 30% for the studied media) and the U_3O_7, (with 58%, 29% and 78%), compared to the fresh product,
- leaching of ^{238}U and its daughter product ^{234}Th; the degree of leaching strongly depending on the nature of the used liquid reagents,
- prevailing leaching of ^{234}Th, achieved when mechanoactivation in TBP (and in TTA [2]) is performed; the later effect is ascribed to the increase of ^{234}Th concentration at defect places and the preferable disintegration of the samples along these places as result of the mechanical loading,
- practically no leaching of ^{234}Th is observed at activation in TOA and in EGME, possibly due to the formation of UO_2 – ThO_2 solid solution.

Further studies have to be made to elucidate the potential of the applied approach as a step in spent nuclear fuel processing aiming separation or stronger bonding of uranium fission products.

5. Acknowledgment

The work is performed with the financial support of the Bulgarian National Science Fund under Contract X-1409/2004.

6. Literature

1. Navratil, J. D. Solvent extraction in nuclear technology. - Pure&Appl. Chem., 58, 1986, 885.
2. Kovacheva, P., D. Todorovsky, D. Radev, V. Mavrudiev, R. Petrov, D. Kovacheva. Mechanochemical effects in U_3O_8. - J. Radioanalyt. Nuclear Chem., 262, 2004, 573.
3. Kovacheva, P., D. Todorovsky, D. Radev, N. Minkova. Mechanochemistry of the 5f-elements compounds. 4. Mechanochemistry of uranium (IV and VI) oxides. - J. Radioanalyt. Nuclear Chem., 274, 2007, 481.
4. Kovacheva, P., D. Todorovsky, D. Radev. Mechanochemistry of the 5f-elements compounds. 5. Influence of the reaction medium on the mechanochemically induced reduction of U_3O_8. - J. Radioanalyt. Nuclear Chem., 287, 2011, 193.
5. Kovacheva, P., N. Minkova, D. Radev, D. Todorovsky. Mechanochemistry of the 5f-elements compounds. 3. Mechanochemicaly stimulated formation of nitrosyl uranyl nitrate. - J. Radioanalyt. Nuclear Chem., 274, 2007, 473.
6. Kovacheva, P., G. Avdeev, D. Todorovsky. Mechanochemically induced synthesis of UO_{2+x} and uranium-thorium mixed oxides from sol-gel produced precursors. - J. Radioanalyt. Nuclear Chem., 287, 2011, 519.
7. Kovacheva, P., Avdeev, G., Application of mechanochemical activation for synthesis of uranium-lanthanoid mixed oxides. - J. Radioanalyt. Nuclear Chem., 288, 2011, 221.
8. Kleykamp, H. Post-irradiation studies on LWR-MOX fuel fabricated by the optimized co-milling process. - J. Nucl. Mater., 324, 2004, 198.
9. Kovacheva, P., N. Minkova, D. Todorovsky, D. Radev. Mechanochemistry of the 5f-elements compounds. 2. Mechanochemicaly induced change in coordination mode of $UO_2(CH_3COO)_2.2H_2O$. - J. Radioanalyt. Nuclear Chem., 274, 2007, 465.
10. Cox, P. P., H. C. Peterson, G. H. Beyer. Separating hafnium from zirconium. Solvent extraction with tributyl phosphate. - Ind. Eng. Chem., 50, 1958, 141.
11. Turanov, A. N., V. K.Karandashev, N. A. Bondarenko, E. M. Urinovich, E. N Tsvetkov. The extraction properties of phosphoryl-containing aza-podand in hydrochloric acid media. – Zh. Neorganicheskoj Khimii, 41, 1996, 1742 (in Russ.).
12. Cerrai, E., C. Testa. Extraction and separation of zirconium and hafnium by means of liquid anionic exchangers in a hydrochloric acid medium. I. Behavior of some primary, secondary and tertiary amines. - Energia Nucleare (Milan), 6, 1959, 707.
13. Fischer, W., H. P. Pohlmann, M. Beiträgen, K. Adam. Über die Trennung anorganischer Stoffgemische durch Verteilen zwischen zwei flüssigen Phasen. 14. Über die Trennung des Hafniums vom Zirkonium durch Verteilen ihrer Thiocyanate. – Z. anorg. Allg. Chem., 328, 1964, 252.
14. Kraus, W., G. Nolze. PowderCell – a program for the representation and manipulation of crystal structures and calculation of the resulting X-powder patterns. – Acta Appl. Cryst., 29, 1996, 301.
15. Shevchenko, V. B., B. N. Sudarikov. Technologiya urana (Uranium technology). Moskwa, Gosatomizdat, 1961 (in Russ.).
16. Argo, J. P., D. S. Todorovsky, A. G. Maddock. Some autoradiographic observations on alkali chloride crystals containing ^{35}S. – J. Radioanal. Nucl. Chem. Articles, 98, 1986, 365-370.
17. Todorovsky, D., A. Terziev, N. Minkova. Mechanosynthesis and mechanolysis of solid solutions of La_2O_3 with some rare earth oxides. - Cryst. Res. Technol., 31, 1996, 1059.

HARDENING LOW CARBON STEEL 10 BY USING OF THERMAL-CYCLIC DEFORMATION AND SUBSEQUENT HEAT TREATMENT

УПРОЧНЕНИЕ НИЗКОУГЛЕРОДИСТОЙ СТАЛИ 10 С ПОМОЩЬЮ ТЕРМОЦИКЛИЧЕСКОЙ ДЕФОРМАЦИИ И ПОСЛЕДУЮЩЕЙ ТЕРМИЧЕСКОЙ ОБРАБОТКИ

D.Sc. (Eng.), Prof. Prudnikov A., D.Sc. (Eng.), Prof. Popova M., Ph.D. student Prudnikov V.
Siberian State Industrial University, Russia
E-mail: a.prudnikov@mail.ru, m.popova@rdtc.ru, vladpr88@gmail.com

Abstract: *The results of the influence of preliminary thermal-cyclic deformation and subsequent hardening heat treatment on the microstructure and mechanical properties of hot-rolled sheet steel 10 are presented. It is shown that the use of preliminary thermal-cyclic deformation of the steel 10 stock material results in a fine-grained structure of a hot-rolled sheet (3 mm thick) produced by an industrial technology.. Deformation occurred at a temperature above A_{C3} (1250 °C), with cooling to 200-300 °C during 10 cycles and the deformation ratio per cycle being 6-8 %. The magnitude of the overall reduction ratio was 1.90 and the total amount of deformation was 65÷68 %. Such a treatment before sheet hot-rolling allows increasing the strength characteristics (tensile strength, yield strength) by almost 30 %. It has been established that the use of subsequent heat treatment (quenching, 900 °C, water and tempering 1 h, 600 °C) leads to a further increase in strength characteristics by 15-20 % while maintaining a sufficient level of ductility of sheet steel.*
***KEYWORDS**: STRUCTURE, STEEL, DEFORMATION, MECHANICAL PROPERTIES, THERMAL-CYCLIC DEFORMATION, HARDENING*

1. Introduction

To improve the quality, reliability and durability of parts, components and mechanisms it is necessary to use a comprehensive approach that includes both the creation of new materials as well as the development and implementation of efficient technologies that harden metallic materials. Traditional methods of hardening are often not sufficiently effective. This led to the development of technologies based on methods and modes that allow intensifying a number of physical and chemical processes through the use of features of structural transformations occurring in metals and alloys. Such technologies include deformation thermal-cyclic treatment (DTCT), which is a thermal-cyclic treatment combined with various types of deformation at low or high temperatures. Such a complex treatment leads to an intensification of diffusion processes at specified temperature oscillations with the application of stress and strain, the accumulation of structural changes occurring in the cycles and associated with volume effects of phase transformations, the difference in thermal characteristics of the phases, etc. as well as a change in the gas content in the alloys including hydrogen. As a result, these processes can form an optimal structure and improve physical and mechanical properties of the material [1-6]. The number of thermal cycles, the ranges of temperature, holding at extreme temperatures, heating and cooling rates of parts and pieces as well as the parameters of the deformation process such as form, temperature, the deformation ratio in the cycle and its total value can be used as the process control parameters to obtain fundamentally different structures, and, therefore, different material properties, while applying such treatments. Deformation thermal-cycling treatment can not only improve a number of physical and mechanical characteristics of metals and alloys, but obtain a deformed semi-finished products made of hypereutectic silumins with low plasticity through the use of thermal cycling deformation combined with annealing [7-10]. The development of heat treatment modes followed by DTCT modes is peculiar for each particular steel, cast iron, aluminum alloy grade and cannot be mechanically transfered from one material to another. There are no principal contraindications to the use DTCT for different materials hardened and not hardened by heat treatment. Therefore, the aim of the work was to study the effect of DTCT on mechanical properties of hot-rolled low-carbon steel 10 including preliminary thermal-cyclic deformation at a temperature above A_{C3} followed by rolling and heat treatment

2. Material and methods

Low-carbon fine steel 10 was used as a material in the study. The steel was made at the Novokuznetsk Iron and Steel Plant JSC (Novokuznetsk, Russia). The chemical composition of steel was defined using the emission spectrometer ARL 4460 and is shown in Table 1.

Table 1. Chemical composition of steel 10

Steel grade	Element concentration, [%] (wt.)					
	C	Si	Mn	P	S	Cu
10	0.13	0.22	0.42	0.014	0.018	0.20

A slab of steel 10 with the sizes of 900×700×500 mm was subjected to hot cyclic forging through single-pass broaching by flat backups at the forge-thermal shop of the West Siberian Metallurgical Plant (Novokuznetsk, Russia) using a hydraulic forging press with the load of 2000 ton-force. The heating temperature for forging was 1250 ± 10 °C, the holding time in the furnace was 2 hours without preheating. The heating for deformation was carried out in a continuous gas furnace. Forgings were cooled in the air to a temperature of 200-300 °C. There were 10 cycles of forging with a deformation ratio in each cycle 6 ÷ 8 %. The average reduction ratio was 1.066. The reduction ratio for each cycle was calculated using the formula (1) [11].

$$K = F_0 / F_k \quad , \tag{1}$$

where F_0, F_k are initial and final values of the forgings cross-section area.

The overall reduction ratio determined using the formula

$$K_{overall} = K_1 \times K_2 \times K_3 \times \ldots \times K_n \quad , \tag{2}$$

where K_1, K_2, K_3,…K_n are the reduction ratio per cycle of deformation.

The magnitude of the overall reduction ratio was $K_{overall.}$ = 1.90 and the total amount of deformation was 65 – 68 %. The workpiece height after thermocyclic forging was 365 ± 5 mm and the width was 500 ± 5 mm. Process parameters of thermal-cycling forging of steel 10 blanks for each deformation cycle are shown in Table 2.

Further the blanks were rolled to sheets 3 mm thick at theA.N. Kuzmin Novosibirsk metallurgical plant (Novosibirsk) using the hot-rolling combination mill 810 in according with TI 138-PZ-24-85 for hot-rolled sheet carbon steel 10. Before rolling the blanks were cut in the cutting slabs bay to obtain the desired thickness of 180 mm. Heating of the test blanks was carried out in the continuous gas furnace. The heating temperature for rolling was 1120 - 1250 °C and the holding time in the furnace was 2-2.5 hours. The billets were cogged through 5 passes in a two-roll reversing stand with horizontal rolls after pre-cleaning of the metal from slag and aligning of the strip in width in the roughing stands with vertical rolls. After finishing descaling in a two-roll mill the

resulting tackle was fed to a group of continuous finishing stands through a roller conveyor. This group consisted of five successive four-high stands where the stripe was pressed up to the preset thickness of 3 mm. The rolling speed was 4.5 m/s. The rolling mill 810 was equipped with a control system to monitor the rolled strips temperature and thickness. The rolling finishing temperature of steel 10 was 800 - 860 °C for a sheet 3-4 mm thick and 820-880 °C for a strip with a thickness greater than 5 mm. After rolling, coiling into a roll sheet was carried out on a floor type reel.

Mechanical characteristics of the rolled sheet was evaluated in the static tensile test of the plane specimens with a thickness of 3 mm and a working part length of 70 mm on the Instron 3369 machine according to GOST1497-84.

3. Results and discussion

The contamination of sheet specimens from steel 10 produced by an industrial mode and using thermal cycling forging to obtain

Table 2. Parameters of thermal cycling forging of steel 10 billets

Cycle	$T_{forging.}^{initial}$, [°C]	$T_{forging.}^{final}$, [°C]	$S_{initial}$, [mm]	S_{final}, [mm]	K_n
1	1250	1100	500×700	500×655	1.069
2	1250	1100	500×655	470×655	1.063
3	1250	1100	470×655	470×615	1.065
4	1250	1100	470×615	440×615	1.068
5	1250	1100	440×615	440×575	1.069
6	1250	1100	440×575	415×575	1.060
7	1250	1100	415×575	415×540	1.065
8	1250	1050	415×540	390×540	1.064
9	1250	1050	390×540	390×505	1.069
10	1250	1050	390×505	365×505	1.069
Comments: $T_{forging.}^{initial}$, $T_{forging.}^{final}$ are initial and final forging temperatures; $S_{initial}$, S_{final} are cross-sectional dimensions of the initial billet and the billet after forging; K_n is a reduction ratio in the n-cycle; $K_{overall.} = 1.90$ is an overall reduction ratio					

Heating for quenching and tempering of the specimens cut from sheets, was carried out in resistance furnaces SNOL 2.2, 5.2 / 12.5-I1, and to measure the temperature a chromel-alumel thermocouple potentiometer DC PP-63 was used. An optical microscope OLYMPUS-GX51F was used to investigate the microstructure of the steel. Metallographic methods for determination the contamination of steel 10 sheets with nonmetallic inclusions was used in accordance with GOST 1778-70 [12].

an intermediate and final thickness of the rolled metal was evaluated. Grades of line and point oxides (alumina Al_2O_3, silica SiO_2, and the iron-manganese spinel $MeO \cdot Al_2O_3$ type), brittle, non-deformable and plastic silicates (aluminosilicates, silicates, iron, manganese and more complex compositions), and sulfides (mainly double sulfide of iron and manganese (FeMn)S) located in the rolled metal of varying thickness (see Table 3) are defined by

Table 3. Assessment of contamination of hot-rolled sheet steel 10 made by an industrial mode and using DTCT with non-metallic inclusions

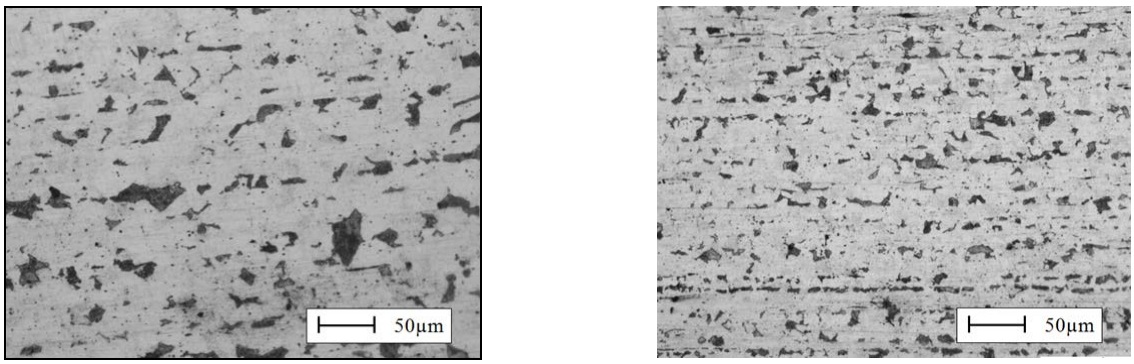
Sheet thickness, [мм]	Slice place	Score					
		Oxides		Silicates			sulfides
		line	point	non-deformable	brittle	plastic	
6	middle of the sheet	3/1	0/1	1/1	0/0	0/0	2.5/3
	edge of the sheet	0/1	3/2	0/0	0/0.5	0/0	1.5/1
5	middle of the sheet	0/2	3/3	0/1	1/0	0/0	2/1.5
	edge of the sheet	0/0.5	3/2	0/1	0.5/1	0/0	1/1.5
4	middle of the sheet	0/1	3/3	1/0	0/0	0/0	1.5/2
	edge of the sheet	1/0	0/1	1/1	0/0	0/0	1/1
3	middle of the sheet	0/0	2/1	1/1	0/0	0/0	1/1
	edge of the sheet	1/0	0/1	0/1	0/0	0/0	0.5/0.5
Average grade		0.6/0.7	1.8/1.8	0.5/0.8	0.2/0.2	0/0	1.4/1.5
Comments: the numerator shows the data for rolled sheet steel 10 manufactured using DTCT; the denominator - for sheet produced by an industrial mode.							

This method involved the study of not-etched metallographic specimens cut along the rolling direction from the middle and end sections of the hot-rolled sheet of various thicknesses from 6 to 3 mm. Inclusion in microsections were viewed through an optical microscope at a magnification of 100 with a field of view diameter of 0.8 mm in one direction - from the end to the central area of the sheet. A score of nonmetallic inclusions in the samples was carried out for each type separately (oxides, sulfides and silicates) by comparison with standard scales for steels.

standard scales of nonmetallic inclusions (GOST 1778). It can be seen that, most of oxide inclusions including silicate and located along the rolling direction. The findings suggest that the hot deformation ratio and preliminary thermal-cyclic forging of billets has virtually no effect on the contamination and distribution of non-metallic inclusions in the cross section of strips of varying thickness. The distribution of inclusions in the rolling metal is mostly random and is determined by the part of the ingot a

particular slab is made of as well as by the steelmaking technology.

The preliminary thermal-cyclic forging that reduces the size of



a b

Fig.1. Microstructure of hot-rolled sheet steel 10 (thickness: 3 mm) manufactured by industrial technology (a) and using the preliminary thermal -cyclic forging (b)

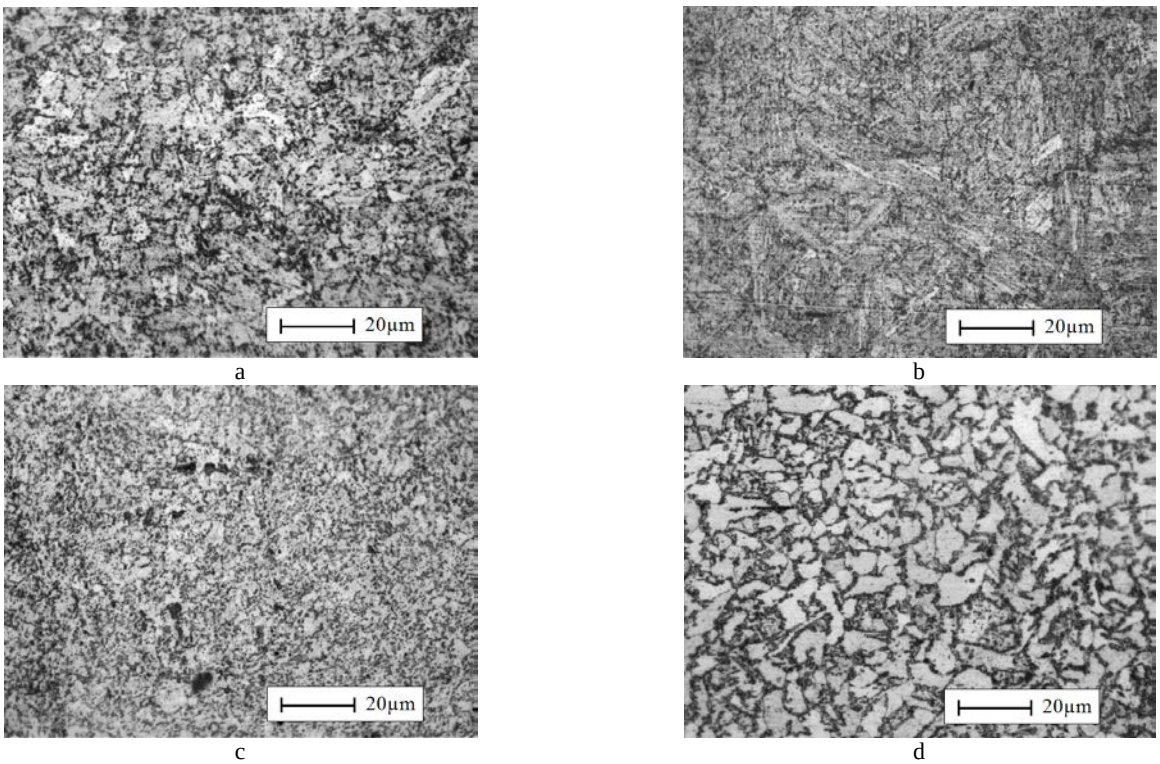
A metallographic analysis of steel 10 specimens rolled using an industrial technology and using the DTST mode showed that preliminary thermal-cyclic deformation led to a decrease in the size and volume fraction of pearlite colonies as well as the degree of misorientation in the direction of rolling. The microstructure of hot-rolled steel 10 depends on the mode of production and is shown in Fig. 1. Obviously, the quantitative structure characteristics are largely determined by the scheme and mode of deformation. Thus, the use of preliminary thermal-cyclic forging prior to sheet hot rolling allows reducing the size of the steel 10 structure. The maximum size of pearlite colonies in the sheet with a thickness of 3 mm is reduced from 22×60 to 7×19 mm, and their average size decreased nearly 3-fold from 7 ± 2 to 20 ± 2 microns.

the steel 10 structure, increases the strength characteristics (tensile strength - σ_{ts}, yield strength - σ_{ys}) of hot-rolled sheet steel 10 by almost 30 % with a slight decrease in ductility (Table 4).

Further hardening of hot-rolled sheet steel may be associated with a subsequent heat treatment of an optimal mode. Therefore, the effect of the quenching temperature (holding time 0.5 hours) and subsequent high-temperature tempering (600 °C, 1 h) on the microstructure and mechanical properties of hot-rolled steel 10 subject to DTTSO was investigated. The microstructure of the steel after hardening heat treatment is shown in Fig. 2. It was established that increasing the heating temperature for quenching from 860 to 900 °C led to a significant refinement of the ferrite-cementite mixture in the structure of steel – sorbite formed after high-

Table 4. DTST influence on mechanical properties of hot-rolled sheet steel 10

State	Mechanical characteristics				
	σ_{ts}, [MPa]	σ_{ys}, [MPa]	δ, [%]	Ψ, [%]	Hardness, [HB]
Hot-rolled by industrial technology	370	305	26	42	127
Hot-rolled using the DTCT mode	478	390	24	38	170



a b

c d

Fig. 2. The effect of the quenching temperature for 0.5 h and subsequent annealing at 600 °C for 1 h on the microstructure of hot-rolled sheet steel 10 (3 mm thick) made with a preliminary thermal-cyclic forging: a - 880 °C; b - 900 °C; c - 920 °C; d - 940 °C

temperature tempering. When quenching the specimens from 920 °C there are the first signs of coagulation and coarsening of cementite precipitates and, after hardening from 940 °C and tempering their size increases several times. Mechanical properties of hot-rolled sheet steel 10 made by DTST quenched from different temperatures and tempered at 600 °C for 1 hour are shown in Table 5.

Table 5. The effect of a quenching temperature (holding time 0.5 hours) and tempering (600 ° C, 1 h) on the mechanical properties of hot-rolled steel 10 subjected to DTCT

Quenching temperature, [°C]	Mechanical properties				
	σ_{ts}, [MPa]	σ_{ys}, [MPa]	δ, [%]	Ψ, [%]	Hardness, [HB]
–	478	390	24	38	170
860	438	360	29	44	168
880	510	458	21	37	182
900	545	470	21	36	183
920	520	468	23	42	181
940	450	383	30	46	174

Data in Table 5 shows that the most optimal combination of strength and plastic characteristics of sheet steel 10 made using the preliminary thermo-cyclic forging mode is provided by hardening heat treatment: quenching, 900 °C, 0.5 hours, water and tempering 600 °C, 1 h. And after the above hardening mode the deformation resistance (σ_{ts}, σ_{ys}) of sheet steel increased by 15-20 % while the elongation reduced by 12 % remaining at a high level (over 20 %). At higher heating temperatures for quenching strength characteristics of steel are impaired, but ductility increases significantly. Such a change in the properties is associated with an increase in the size of cementite precipitates and their coagulation in the steel structure during tempering. Thus, the elongation of the specimens after quenching from 940 °C and tempering increased by 25 % compared to hot-rolled steel.

4. Conclusions

1. The preliminary thermal-cyclic forging does not increase the contamination of hot-rolled sheet steel 10 with nonmetallic inclusions whose number and distribution is determined by the slice place and steelmaking technology.

2. The use of preliminary thermal-cyclic forging for the production of hot-rolled sheet steel 10 provides a more fine-grained structure and improves its strength characteristics by almost 30 %.

. 3. Application of a rational mode of hardening and tempering (hardening at 900 ° C for 0.5 h, water and tempering at 600 ° C, 1 h) allows increasing strength characteristics (σ_{ts}, σ_{ys}) by 15-20 % while maintaining sufficient ductility of hot-rolled sheet steel 10 manufactured using DTCT.

5. Literature

1. Fedyukin, V. Thermocyclic processing of metals and details of cars. Leningrad, Mashinostroenie Publ., 1989, 255 p. (Fedyukin, V., M. Smagorinskij).

2. Furuya, Y. Thermal Cyclic Deformation and Degradation of Shape Memory Effect in Ti-Ni Alloy.– Nondestructive testing and evaluation, vol. 8(1), 1992, pp. 541-554 (Furuya, Y.,Y. Park).

3. Prudnikov, A. Assessment of impact of thermocyclic deformation and the subsequent heat treatment on electrophysical properties of low-carbonaceous steel.– Actual problems in machine building, v. 2, 2015, pp. 396-400 (Prudnikov, A., В. Попова, В. Прудников).

4. Afanas'ev, V. Influence of thermocyclic deformation and annealing on the structure and specific electrical resistivity steel grade Ст3пс.– Actual problems in machine building, v. 1, 2014, pp. 431-434 (Afanas'ev, V., А. Прудников, М. Попова, В. Прудников).

5. Prudnikov, A. Influence of thermocyclic forging and subsequent annealing on the coercive force and linear expansion of steel 10.– Actual problems in machine building, v. 3, 2016, pp. 451-456 (Prudnikov, A., В. Прудников).

6. Okajama, J. A thermal cycling and super plastic of steel.– J. Iron and Steel, v. 68 (12), 1982, P. 1248 (Okajama, J).

7. Prudnikov, A. Production, structure and properties of engine pistons made from transeutectic deformable silumin. – Steel in Translations, v. 39, 2009, pp. 391-393 (Prudnikov, A.).

8. Prudnikov, A. The complex effect of annealing and thermal cycling forging on the structure and properties of hypereutectic silumins. – Deformatsiya i razrushenie materialov, v. 2, 2014, pp. 14-20 (Prudnikov, A.).

9. Ehskin, G. Issledovanie tekhnologii izgotovleniya polufabrikatov iz zaehvtekticheskogo silumina 01392 s ispol'zovaniem poperechno-vintovoj prokatki. – Tekhnologiya legkikh splavov, №. 1, 2008, ss. 83-89 (Ehskin, G., А. Артес, Е. Панов, Л. Бер, С. Бочвар, В. Ялфимов).

10. Prudnikov, A. Piston deformable hypereutectic silumin. – Tekhnologiya metallov, v. 2, 2014, pp. 8-11 (Prudnikov, A.).

11. Okhrimenko, YA. Teoriya protsessov kovki. Moskva, Vysshaya shkola, 1977, s. 274 (Okhrimenko, YA., В. Тюрин).

12. GOST1778-70. Stal'. Metallograficheskie metody opredeleniya nemetallicheskikh vklyuchenij (s izmeneniyami). Moskva, Standartinform, 2011, s. 34.

PRODUCTION OF HIGH SOLID CONTENT POLYMER/YSZ COMPOSITES AND FREE FORM YSZ FIBERS

M.Sc. D. Yilmaz Cakta[1], Assoc. Prof. Dr. B. Ozkal[2]

[1] Eskisehir Osmangazi University, Eskisehir, [2]Istanbul Technical University, Istanbul, Turkey.

E-mail:dcakta@ogu.edu.tr, ozkal@itu.edu.tr

Abstract: *With 65 wt% solid content, Polymer/YSZ composites have been produced via extruder by using of PP, PMMA and TPU. With pyrolysis process, physical stability conditions of continuous YSZ free form fibres have been investigated according to type of polymer and pre-sintering temperature. In addition to this, melt flow rate values and thermal analysis investigations of PP, PMMA, TPU, PP/YSZ, PMMA/YSZ, TPU/YSZ were determined by melt flow rate analysis and TGA. Compared to unreinforced polymers (PMMA, PP and TPU) the melt flow rate of the composites containing YSZ powder has decreased approximately 15 %. From TGA results it was also found that the contribution of the yttria stabilized zirconia changed the decomposition temperature of the polymer part.*

KEYWORDS: POLYMER/YSZ COMPOSITES, MELT FLOW RATE, PYROLYSIS, FREE FORM FIBERS

1. Introduction

Polypropylene is one of the most popular thermoplastics, due to its high isotacticity, enhanced mechanical properties, narrower molecular weight distribution and increased clarity lead to a balance of physical and mechanical properties, and its environmental friendliness (recyclability) and low cost. However, with these advantages, there is also a handicap. Although its resistance to crack initiation is very high, especially at low temperatures, resistance for crack propagation of the PP matrix is very low. To optimize this behaviour, PP is usually modified with some reinforcements. PMMA is also one of the most popular thermoplastic materials with properties such as optically clear amorphous view, perfect transparency, higher impact strength. However, its application is limited at elevated temperature due to its relatively poor thermal stability [1].

Polyurethanes appear in a variety of forms: foams, elastomers, adhesives, coatings, shape memory applications, also, their elastomers (TPU) can be repeatedly melted and processed due to the absence of the chemical networks. In recent years, TPU was used in the spindle and shrink-proof processing [2-5].

In polymer matrix composites, fillers have a substantial role in developing the properties of thermoplastics and with their addition, improved mechanical properties can be obtained on polymeric materials [1].

In recent years, studies about the addition of fillers to polymers increase due to effect of fillers on composites thermal stability [6].

Yttria stabilized zirconia (YSZ) is recognized as one of the most suitable electrolyte material in solid oxide fuel cell technology (SOFC) and due to its stability in cubic structure, it can be used as fillers in applications which needs ionic conductivity and oxygen vacancies. With pyrolysis of polymers in PMC, porous materials can be obtained [7].

Porous materials are important in many industries and applications which needs high surface area, filtration ability and tendency to control over optical properties such as adsorbants, sensors and catalysts, electrodes for fuel cells [8-17].

In this study, with high solid content (65 wt%) composites free form fibers were produced with using extruder and to create continuous YSZ fibers, polymer parts of composites were pyrolyzed under an Argon atmosphere.

2. Experimental Procedure

For production of PP/YSZ, PMMA/YSZ, TPU/YSZ composites, commercial PP (Borealis), PMMA (Acrytex), TPU (Bayer Desmopan) polymers and 8-YSZ which we synthesized via high energy milling were used. To cover polymer granules with YSZ, powders and granules milled together 30 minutes in polypropylene jars with planetary mill.

With 65 wt% solid content, PMMA/YSZ, PP/YSZ, TPU/YSZ composites have been produced with two different diameters (2 and 5 mm, averagely) of cylindrical form via extruder. Amount of solid that can be feeded to the system homogenously was determined according to sustainability of product which was taken from extruder. Samples which have 2 mm diameters, pressed at 150 MPa during 2 minutes to observe physical stability of YSZ fibers after pyrolysis.

TGA investigations of PP, PMMA, TPU, PP/YSZ, PMMA/YSZ,TPU/YSZ were done in order to search out effect of YSZ on decomposition temperature of system. Effect of YSZ powders on PP, PMMA, TPU, PP/YSZ, PMMA/YSZ, TPU/YSZ systems were also investigated by melt flow rate analysis. Pyrolysis temperature was kept at 450˚C and heating/cooling rate were determined at 2˚C/min and 5˚C/min, respectively. After pyrolysis, sintering was carried for each system at 700, 900 and 1100˚C. Information about samples are given by Table 1.

With pyrolysis process, stability conditions of continuous YSZ have been investigated according to type of polymer and pre-sintering temperature.

During pyrolysis process, stability of continuous structures have been supported by alumina powder bed in a alumina crucible.

Table 1: *Sample name and operations*

Sample Name	Raw materials	Diameter (mm)	Sintering Temperature (°C)
PMMA/YSZ-700(5)	PMMA/YSZ	5	700
PMMA/YSZ-900(5)	PMMA/YSZ	5	900
PMMA/YSZ-1100(5)	PMMA/YSZ	5	1100
PP/YSZ-700(5)	PP/YSZ	5	700
PP/YSZ-900(5)	PP/YSZ	5	900
PP/YSZ-1100(5)	PP/YSZ	5	1100
TPU/YSZ-700(5)	TPU/YSZ	5	700
TPU/YSZ-900(5)	TPU/YSZ	5	900
TPU/YSZ-1100(5)	TPU/YSZ	5	1100
PMMA/YSZ-900(2)	PMMA/YSZ	2	900
PP/YSZ-900(2)	PP/YSZ	2	900
TPU/YSZ-900(2)	TPU/YSZ	2	900

3. *Results and Discussion*

In Figure 1-3, TGA investigations showed that YSZ reinforcements effect on decomposition temperature of TPU, PP and PMMA. YSZ reinforcement increased decomposition temperature of PMMA and decrease decomposition temperature of PP and TPU. It is known that, high solid content gets higher heat resistance to the polymer matrix composites. But in soft polymers, when temperature gets higher, solid content comes together due to the melting of polymer part of the system. In this way, structure becomes non-homogeneous and thermal stability decrease due to the decomposition of surface which is in contact with solid part.

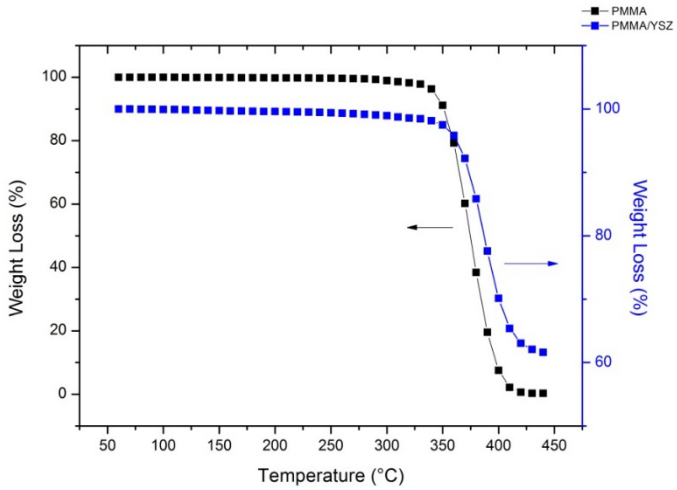


Figure 1. *TGA analysis of PMMA and PMMA/YSZ.*

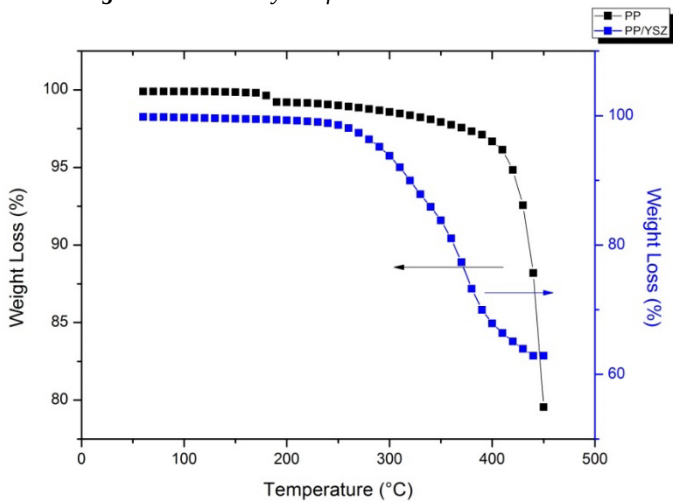


Figure 2. *TGA analysis of PP and PP/YSZ.*

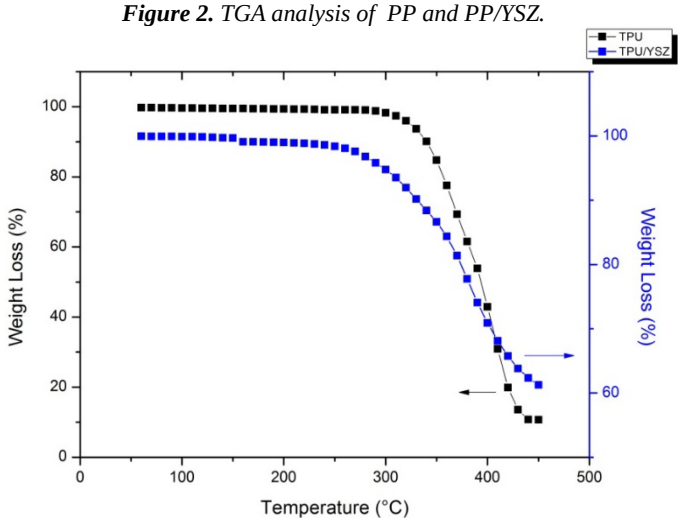


Figure 3. *TGA analysis of TPU and TPU/YSZ.*

Melt flow rates of PP, PMMA, TPU, PP/YSZ, PMMA/YSZ and TPU/YSZ are given by Table 2. Compared to unreinforced polymers (PMMA, PP and TPU), melt flow rate of the systems containing YSZ powder has decreased approximately 15% at PMMA/YSZ and PP/YSZ and TPU/YSZ systems. According to these results, it can be verified that due to filler effect of YSZ, polymer chains mobility has decreased with similar other studies.

Table 2: *Melt flow rate values of samples.*

	Melt Flow Rate (g/10 min)
PMMA	19,8
PMMA/YSZ	16,8
PP	20,0
PP/YSZ	17,2
TPU	17,7
TPU/YSZ	17,0

It is also determined that disc structures which pressed into disk from fibers that have 2 mm diameters and consisting of only composite fibers formed in the original shapes and in these systems, TPU/YSZ system preserved the shape of the YSZ fibers after pyrolysis. It can be clearly seen that YSZ fibers keep their structure after pyrolysis of TPU/YSZ due to elastomeric nature of TPU. In figure 4-6, it can be seen that samples which have 5 mm diameter, keep their cylindrical forms after pyrolysis. At TPU/YSZ disk, one receives that for YSZ fibers in TPU matrix were kept their continuous order after pyrolysis of TPU (Fig. 7). Some of them were formed as cylindrical tubes as same with fibers which have 5 mm diameter. Around YSZ body, spherical alumina powders can be seen obviously that used for powder bed.



Figure 4. *Stereomicroscope image of YSZ samples after pyrolysis of PMMA/YSZ-900(5).*

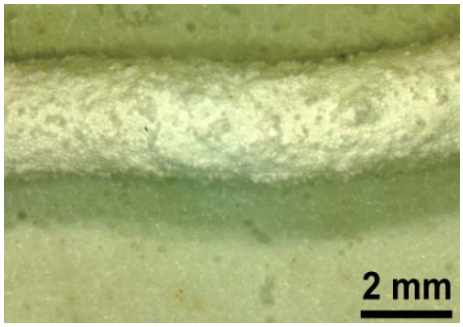


Figure 5. *Stereomicroscope image of YSZ samples after pyrolysis. of TPU/YSZ-900(5).*

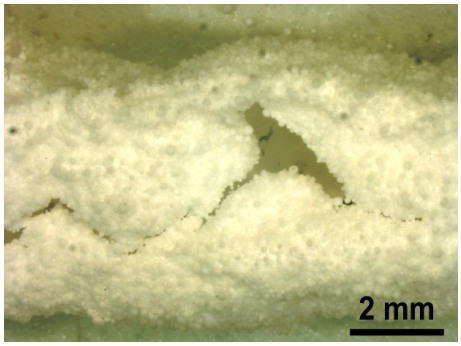


Figure 6. *Stereomicroscope image of YSZ samples after pyrolysis of PP/YSZ-900(5).*

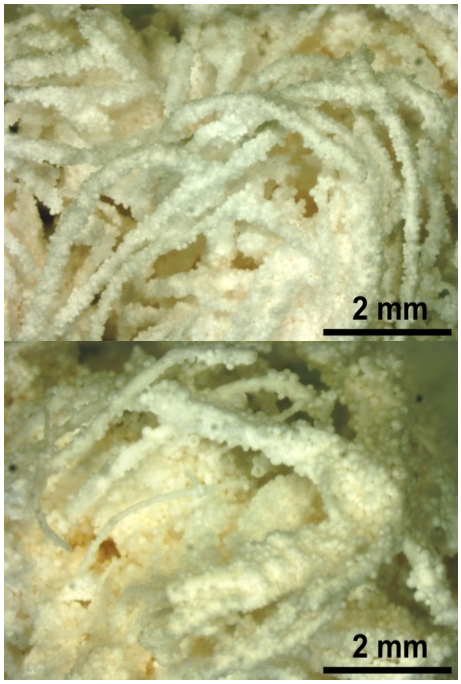


Figure 7. *Stereomicroscope images of YSZ samples after pyrolysis of TPU/YSZ-900(2).*

After pyrolysis of the extruded products, YSZ system was formed as hollow cylinder or more intensive of porous cylinders depending on the polymer and their shapes dependent on both polymer type and sintering conditions which have been carried out after pyrolysis process.

Particle size, morphologies and structure which depend on polymer type and sintering temperature after pyrolysis can be seen on SEM images in Figure 8-10. Due to the elastomeric nature of TPU, particles comes together by necking mechanism, so structure is coarser than other systems. In PP/YSZ system, due to the low decomposition temperature of PP, particles keep their positions and finer structure can be seen in the system. For PMMA/YSZ, due to the lowest melt flow index of system and different mobility value of methyl and methacrylate group, coarser particles formed by joined particles that comes together and finer particles occurred by unjoined particles.

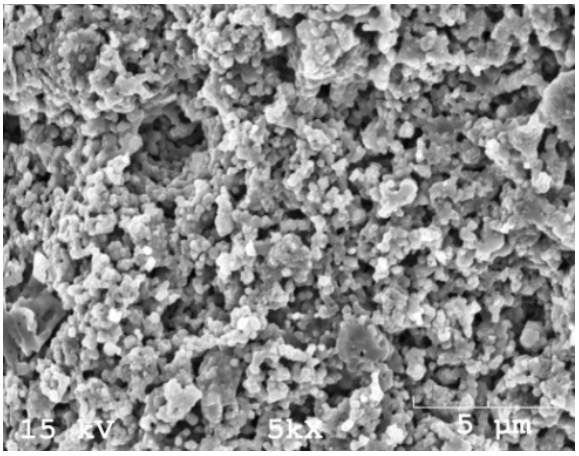


Figure 8. *SEM images of YSZ samples after pyrolysis of PP/YSZ-900(5).*

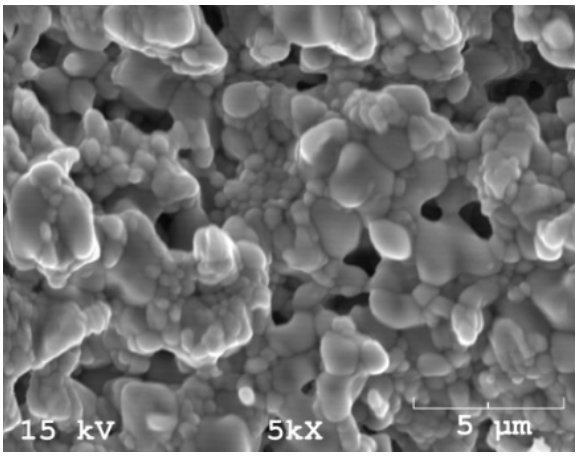


Figure 9. *SEM images of YSZ samples after pyrolysis of PMMA/YSZ-900(5).*

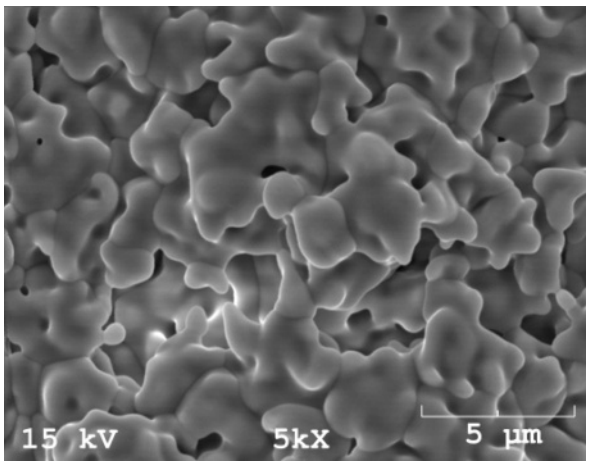


Figure 10. *SEM images of YSZ samples after pyrolysis of **T**PU/YSZ-900(5).*

In Figure 11, SEM images of YSZ fibers after pyrolysis can be seen. YSZ fiber after pyrolysis of PP/YSZ composite fiber had averagely 200 µm diameter and from SEM image it can shown that YSZ fiber can keep its shape after pyrolysis of PP. In mid of the fiber, alumina granules can be seen around YSZ fiber.

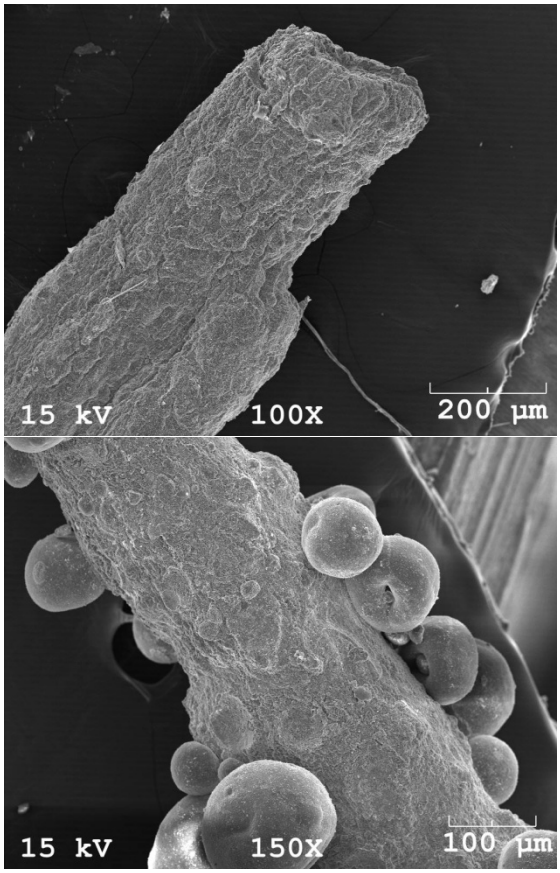


Figure 11. *SEM images of YSZ fibers after pyrolysis (tip and middle part of fiber).*

4. Conclusion

PP/YSZ, PMMA/YSZ and TPU/YSZ composites were produced via extruder. TGA, MFR analysis was carried out to investigate the thermal and melting behaviour of YSZ on PP, PMMA and TPU's. From TGA results and melt flow analysis, it was found that the contribution of the YSZ changed the decomposition temperature and melt flow rate of the polymer part. Melt flow rate of systems were decreased with YSZ reinforcement to the polymers. For TGA investigations, it is concluded that both for TPU and PP, decomposition temperatures were decreased although for PMMA's was increased.

After pyrolysis, shape stability on pressed samples was seen on YSZ fibers that formed from TPU/YSZ composites. During stereo microscope studies it was observed that the prevention of initial form after pyrolysis is possible. Degree of prevention was found higher in TPU/YSZ system. YSZ fibers also kept their initial forms after pyrolysis and tube formation was observed. Although diameter of these tubes are fluctuating along to fiber axis, initial results were evaluated quite motivating for the formation of differen hollow forms having desired diameter and length.

Acknowledgement

This work was funded by ITU-BAP under project number 34011.

References

[1] Chrissafis, K., D. Bikiaris, Thermochimica Acta, 523, 2011, 1–24.

[2] Woods, G., The ICI Polyurethanes Book, 2nd ed., John Wiley & Sons, Chichester, 1990.

[3] Wirpsza, Z., Polyurethanes; Chemistry, Technology and Applications, Ellis Horwood, New York, 1993, 1-6.

[4] Frick, A. and A. Rochman, Polymer Testing, 23, 413, 2004.

[5] Kim, S. M., N. S. Kwak, Y. K. Yang, B. K. Yim, B. Y. Park, and T. S. Hwang, Polymer (Korea), 29, 253, 2005.

[6] Katsikis, N., F. Zahradnik, A. Helmschrott, H. Munstedt, A. Vital, Polymer Degradation and Stability, 92, 2007, 1966-1976.

[7] Singhal, S. C., Science and Technology of Solid-Oxide Fuel Cells. MRS Bull., 2000, 25, 16-21.

[8] Madhavi, S., C. Ferraris, T.J. White, Journal of Solid State Chemistry 178, 2005, 2838.

[9] Wang, C., A. Geng, Y. Guo, S. Jiang, X. Qu, L. Li, Journal of Colloid and Interface Science 301, 2006, 236.

[10] Yurii, N.Y., A. Vlasov, David J. Norris, Advanced Materials 11, 1999, 165.

[11] Im, S.H., Y.T. Lim, D.J. Suh, O.O. Park, Advanced Materials 14, 2002, 1367.

[12] Wijnhoven, J.E.G.J., W.L. Vos, Science 281, 1998, 802.

[13] Zhang, Y., S. Zha, M. Liu, Advanced Materials 17, 2005, 487.

[14] Chen, F., C. Xia, M. Liu, Chemistry Letters 30, 2001, 1032.

[15] Ruiz-Morales, J.C., J. Canales-Vazquez, J. Pena-Martinez, D.M. Lopez, P. Nunez, Electrochimica Acta 52, 2006, 278.

[16] Ruiz-Morales, J.C., J. Canales-Vazquez, J. Pena-Martinez, D. Marrero-Lopez, J.T.S. Irvine, P. Nunez, Journal of Materials Chemistry 16, 2006, 540.

[17] Boaro, M., J.M. Vohs, R.J. Gorte, Journal of the American Ceramic Society 86, 2003, 395.

THE EXPLOSIVE CRYSTALLIZATION OF AMORPHOUS MICROWIRE

ВЗРЫВНОЙ ПЕРЕХОД В АМОРФНОМ МИКРОПРОВОДЕ

Borisenko I. Yu., Tulin V. A.
Institute of Microelectronics Technology and High Purity Materials, the Russian Academy of Sciences, Chernogolovka, Moscow region, Russia.
E-mail: eagle@iptm.ru

Abstract: *Amorphous microwire in a glass shell has low thermal inertia and can be rapidly heated to the crystallization temperature. We observed the transition process of the microwire from amorphous to microcrystalline state during its heating by pulse current of different amplitudes and durations. The crystallization of amorphous state proceeded in two ways depending on a pulse parameters: "slow" and explosive. In the second case electromagnetic waves emission (light flash) and burst of resistance were observed. The propagation velocity of the crystallization front in our experiments was 1 m/s.*
KEYWORDS*: AMORPHOUS MICROWIRE, EXPLOSIVE CRYSTALLIZATION.*

The phenomenon of explosive crystallization (EC) of amorphous materials gains much attention of researchers in chemistry, physics, materials science and other disciplines. Amorphous materials are non-equilibrium "frozen" metastable states. As temperature increases, energy barrier separating this state from the equilibrium microcrystalline state, can be surmounted, and a possibility appears of transition into equilibrium nanocrystalline state. A distinctive feature of this transition is a possibility of existence, in parallel with slow processes, the fast ones associated with phase decomposition and with the crystallization front driving due to its substantial self-heating [1].

The growth rate of the crystalline phase in the initial regime associated with surmounting of the potential barrier is described by its Arrhenius dependence

$$U = U_0 \exp(-E/kT) \qquad (1),$$

where U_0 is a constant, E is activation energy, k is Boltzmann constant, and Tis absolute temperature. According to this equation, the crystallization temperature is not strictly specified. The growth process goes with rather high rate in some temperature range. Since the reaction of transition from amorphous to micricrystalline material is exothermal, it is characterized by some specific heat release Q. The scale of this heat release plays a significant role in specifying of the transition character. If heat release during the transition is lower than heat emission of a sample into atmosphere, the transition goes "uniformly" in a sample volume with gradual decrease in non-equlibrium of amorphous material (the process is similar to isothermal). In the opposite case (explosive crystallization) emission of latent heat of the phase transition brings to local heating of a sample, acceleration of the transition process, decomposition of a phase, and generation of interphase boundaries. Heat emission is focused on the interface, crystallization front is self-heated and moves to amorphous material, transforming it into microcrystalline state. At that, the crystallization front propagation velocity can reach 32 m/s in the self-sustained regime [2, 3].

The EC was observed in amorphous film structures: semiconductors [4-6], metals [7, 8], dielectrics [9]. A significant role in these cases played a substrate, through which the heat emitted during self-heating was prevailingly removed. The samples shaped amorphous films are convenient for studies, since they make it possible to monitor the transition process using different microscopes [5, 10, 11]. Dimensional scales in them are quite macroscopic (millimeters, centimeters). But we have studied the phase transition process in amorphous microwire.

The amorphous microwire obtained by Ulitovskii-Taylor method [] is rather important highly technological material as regards applications. Especially this concerns its magnetic and microwave properties. In the postwar years the technology developed by Ulitovskii provided substantial improvement in quality of galvanometers, which were the main devices for studies of electric and magnetic properties of materials at that time.

In this work we studied the Fe15Co60B10Si15 wire. Some pieces of this wire remained after our work [12] with colleagues from National University of Science and Technology MISiS. Diameter of the metal conductor was 16 micron, diameter of the glass shield (shell) was 26 micron. To heat the microwire we used a pulse current source (rectangular pulse of duration from 20 to 500 ms). A piece of the microwire 6-100 mm in length was mounted in indium-gallium alloy drop (which is liquid at room temperature) being contacts on electric layout made on foiled textolite. During the measurements on an oscilloscope the following characteristics were controlled: a change in voltage drop on a sample (a bridge scheme was used), current through the sample, and the output voltage of a source (a pulse generator).

We used ferromagnetic resonance (FMR) as a method of characterization of the microwire state. For this we observed FMR in the microwire in amorphous or microcrystalline state. In amorphous state FMR is easily detected in some segments of the microwire of 2-3-mm length (with their regular position in the resonator) [12]. In the microcrystalline state FMR is not detected in similar segments during measurements on our ESR-spectrometer.

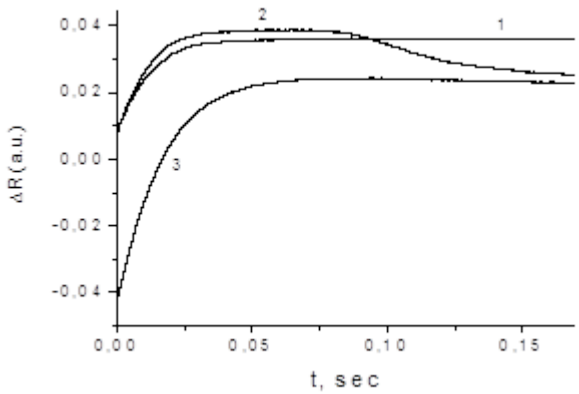


Fig. 1. Examples of recording of the dependence of a change in resistance on time from the beginning of the current pulse.

Fig. 1 shows dependencies of a resistance change value on time counted from the beginning of a current pulse. The curves 1 and 2 response to a current pulse amplitude increment curves 2 and 3 are registered at the same output pulse of the generator. After the process described by curve 1, the sample remains in amorphous state (FMR after this treatment is observed). After passing curve 2 the sample transits into new state (absence of FMR). Curve 3 corresponds to impact of a current pulse on the sample in new state. After pulse switching the microwire begins to heat to the temperature defined by amplitude of the current in the pulse. The heating time of the sample was about 20 ms, thus for 50 ms the sample almost reached the equilibrium temperature corresponding to the current amplitude in the pulse. This is well seen in the

curves, where no radical changes are observed (curves 1 and 3). Curve 2 is noticeably different from the abovementioned curves. It has a break, after which resistance begins to decrease with time. The break in the curve lasts for about 40 ms, after which equilibrium is established in the new system (exponential decrease in temperature with respect to new resistance value). Multiple repetitions of such experiments has shown that as far as we observe the time dependence of type 2 (break) under action of a current pulse, the sample changes its properties. In these measurements it was noticed that at the moment of the abovementioned break during heating, the microwire, if observed within 100 ms from the pulse beginning, shortly (during time far shorter than the current pulse duration) emits light. Surely, the flash duration we estimated already after the respective measurements.

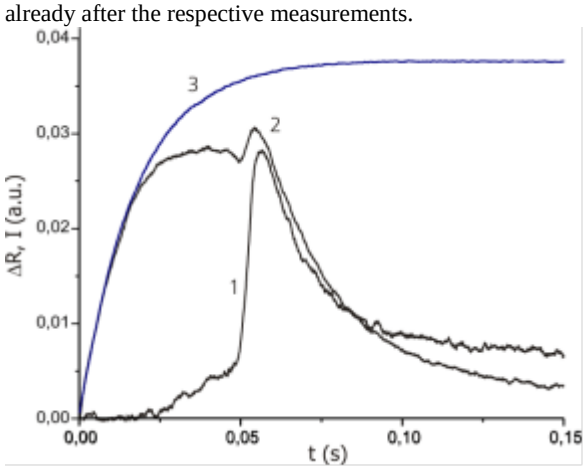


Fig. 2. A change in: (1) brightness of glow, (2) resistance, (3) resistance of the sample earlier undergone the structural transition depending on time from the beginning of the current pulse.

We added fourth channel of measurements, measurements of light intensity. For this purpose at a distance 3-4 mm from the microwire we placed a BURR-BROWN photodiode OPT-211, put the measuring scheme into a closed box, and detected emission from the microwire during action of a current pulse. Fig. 2 shows an example of light emission recording (curve 1) and a change in resistance of the sample (curve 2) under impact of the current pulse. From the beginning of the current pulse the microwire is heated from Joule heat. At that, its resistance increases. In Fig. 2 the dependence of a change in voltage drop of the same sample (its resistance) is shown as a supporting curve (gray curve) at higher temperature of heating, when structural reconstruction are finished (curve 3). The scale of curve 3 is changed to obtain superposition of the initial parts of curves 2 and 3. During heating to a certain temperature a change in the sample resistance is retarded with respect to the supporting curve and even begins to decline. Structural changes take place in the sample, which brings to drop in its resistance. Then a light flash glows, resistance at this moment also shows a burst, and then decreases with time. The flaming time is about 5 ms. Really weaker background glowing begins earlier and remains after the flash extinguishing. This is, probably, an ordinary heat emission corresponding to the temperature of the microwire at approach to the explosive transition of the material into microcrystalline state (~4000 C), which is sensed by a photodiode.

Here it should be noted difficulties, which are encountered during performing these measurements. Though the process of a sample heating by pulse current is rather flexible, the current can be changed quite accurately and gradually, the transition from amorphous state to microcrystalline is irreversible, i.e. on each sample it can be observed only once. Due to the existing spread of the microwire parameters (first of all of the cross section area), it is difficult to establish the desired current value necessary for controlled influence. On the one hand, we need often remount samples, which is by itself rather thorough task, on the other hand, at the initial moment, we do not know the critical current value, at which a sample is heated to or above the temperature of the explosive transition into crystalline state. The value of this current for pieces of the microwire from different parts changed from 50 to 60 mA (density of the critical current was about 2*104 A/cm2). After we exceeded the transition temperature, we have got necessary information, an interest to a sample vanishes, and we need to mount a new one. If a sample could not be transited in the new state by the first pulse, then, as is seen from Fig. 2, there are some structural changes in it, and a fraction of amorphous phase in it decreases.

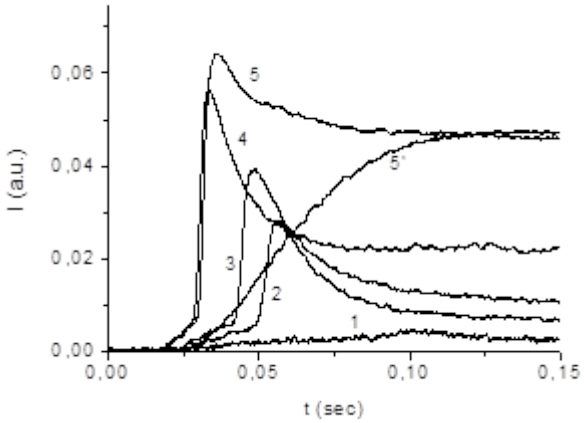


Fig. 3. Examples of changes in brightness of glow during action of the current pulse of over-critical amplitude.

Fig. 3. shows a set of curves detecting signals of surges in glow observed in five samples of the microwire, in which the transition is detected at the first current pulse application. It is seen here that a flash intensity decreases in proportion to time from a pulse beginning, however, time characteristics remain similar (flaming as well as extinguishing). Glow is flared to maximum amplitude for 5 ms, and extinguishes for the time of thermal inertia of a sample. A change in intensity of the background glow for different experiments (a signal amplitude in the right part of the figure) points to a difference between the final temperatures in each measurement. If the break in resistance is in time interval after 100 ms from the beginning of a pulse, there no noticeable light flash is observed (curve 1).

Amorphous state of the material is metastable. Its existence at normal temperatures is determined by presence of quite high energy barrier separating the amorphous state from microcrystalline. As temperature increases, surmounting over the barrier starts in activation way, and the material locally undergoes changes approaching to microcrystalline state. The transition is exothermal and is accompanied by heat emission, which can stimulate propagation of the transition to the adjusted part of a sample. At a certain ratio between heat emission and heat dissipation into atmosphere, self-propagation of the growth front of microcrystalline state begins, and the material transits spontaneously into this state. In literature this phenomenon is called explosive transition. At that, a sample is heated, and additional thermal radiation can arise above the background radiation associated with high starting temperature of the sample. Slightly below this critical condition the transition goes almost isothermally without typical for the explosive transition features. Atoms are driven to their equilibrium positions independently (not avalanche-likely), and the material is crystallized at “slower” rate. Transition from one regime to another can take place at increase in volume crystallization rate (Eq. 1), when heat dissipation cannot absorb emitted heat. AS it can be seen from Fig. 3, background radiation reaches some level before the light flash start. A characteristic of background radiation in our case is response of a photodiode to heat emission of heated microwire, i.e. to its temperature. The explosive transition process in our case begins at some temperature reached by the microwire.

Based on these considerations, most results obtained in this work can be understood. If at the first measurement we set current below the critical value, then there is slow transition to the critical state. Since the temperature of the sample is still near the critical value,

the process goes rather fast, and at the end of the pulse there can be small amount of the amorphous phase. The next pulse will bring to weakened explosive transition or to its slowing-down, to complete absence. Therefore, there are interesting data, when the explosive transition goes at the first applied current pulse. However, in this case also just a part of a sample has time to transit to crystalline state during the time from the beginning of the pulse to the moment of the beginning of the explosive transition. It is well seen from Fig. 2, where resistance begins to decrease actively, despite of temperature rise. This explains the dependence of the light flash on time from the beginning of a pulse, and the reason for the flash not to be seen after 100 ms since the pulse start.

Two observed effects, in our opinion, can be interesting for clarification of the crystallization front structure, this is burst of the sample glow and simultaneous increase in resistance. It is known from observations of the explosive crystallization in amorphous films that the crystallization front looks like a line, its width is far less than its length (in developed state). At that, brightness of its glow is far higher than background glow of the rest of the film (before, as well as after the front propagation). The case of amorphous microwire obtained by Ulitovskii-Taylor method is of a special interest since it is a quasi-one-dimensional object (in our case length is 5-10 mm, diameter is 0.016 mm). The crystallization front in the main stage of development propagates along the microwire axis, the front plane is perpendicular to the axis. This is confirmed by the made measurements. We studied more than ten samples, and most of them showed the same type of behavior (as in Fig. 2). Only in few cases the light flash was double or spread, probably, in these samples there were two or more nucleation centers of the crystalline phase. The problem of heat transfer in the case of the microwire is also simplified, it is reduced to heat exchange between the glass shell and surrounding gas.

Signal of the light flash (more precisely, the photodiode output voltage) first increases with time about 5 ms almost linearly, and then decreases with time of thermal inertia. We believe that this respects to heat accumulation in a sample as the crystallization front propagates, and is followed by the sample cooling after the end of the process. Between the explosive transition process (latent heat emission) and detection signal at the photodiode there are many complicated transformations. But if the crystallization front was responsible for signal from the photodiode, the output voltage would be close to a constant value. It is seen that the character of all observed transitions for different samples at the stage of rise and drop of the signal are similar (Fig. 2). This corresponds for our quasi-one-dimensional samples to the simplest picture of the process. The transition is nucleated somewhere in the middle point of an open wire and is propagated from there to both sides up to entry of the wire into indium-gallium solder. What happens inside the solder is difficult to imagine, since the thermal conditions there differ from the outside. With this regard, we may return to the data in Fig. 1, where smooth transition process without light flash is shown. It is seen that during the transition resistance of the sample decreases below the previous recording, where there was no transition. It seems that Joule heat has become far less than it is necessary for the transition to go on, however, the transition continues going at the same rate. Based on this, it can be assumed that the transition front can also propagate in the microwire being inside the solder. This causes difficulties in estimation of changes in electric resistance of the samples. On the whole, this character of the transition implies that the origin of the light flash (the signal detected by the photodiode) is heating of a sample by heat emitted upon the crystallization front propagation, but not by radiation from the front itself.

Now we shall come to discussion of the results on measuring of electric resistance. Here it will be relevant to present widen data on these measurements. The microwire produced using Ulitovskii-Taylor technique is of some presentation interest for demonstration of temperature change in resistance. The point is that it is coated with a glass shell, which is decomposed at the temperatures above the melting point of the wire material. In Fig. 1 there was no compensation of resistance of the sample at room temperature for recording of curves 2 and 3. It is seen from Fig. 1 that resistance of the sample in microcrystalline state is far lower than the resistance in amorphous state. At the same time, dR/dT (where R is resistance of the microwire and T is temperature) in amorphous state is lower than in crystalline state. A difference in resistance values at room temperature is about 20% from the total resistance of a sample. If, for example, resistance of a sample in amorphous state is 40 Ohm, in microcrystalline state it is 32-34 Ohm. These are typical values.

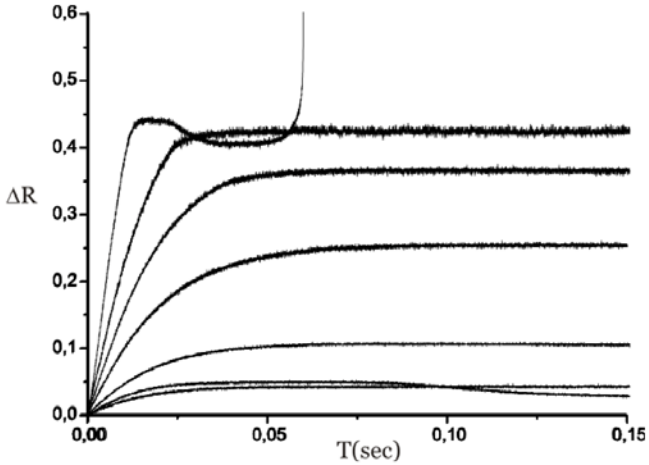


Fig. 4. A change in resistance (in relative units) during applying of current pulses with different amplitudes.

Using these estimations and the circumstance that we did not provide compensation of our measuring bridge scheme for the dependencies shown in Fig. 1, all typical values of changes in resistance can be presented. Fig. 4 presents the results of resistance measurements (in relative units) during applying of current pulses with different amplitudes. The first three curves correspond to the data in Fig. 1, but for another sample. Next curves correspond to increase in current amplitude. In the last figure but one the material is being melted, resistance is the maximum, which does not change (as well as temperature). In the last curve the material is melted (constant resistance range), in liquid state resistance of the sample decreases as temperature increases [13], then the glass shell is decomposed, the liquid material of the wire pours out, breaking continuity of the wire, and resistance rises abruptly. It was possible to get convinced in decomposition of continuity of the sample after the end of the experiment. If now the resistance measurements are used as a thermometer, assuming that resistance of strongly disordered alloy changes linearly with temperature [13], and to suppose roughly that the transition from amorphous to microcrystalline state is at 400ºC, and the melting point for the material of the microwire is 1000ºC, then from surge of the resistance amplitude at the transition, average heating of the sample can be estimated (about 100ºC).

Therefore, observation of the effects of light flash rising and surge of resistance can be simply explained by heating, which does not give us information on structure of the explosive crystallization. The point is that in the first measurements we observed the light flash with a naked eye. The flash was bright white, not red, as it would have been at these temperatures. Unfortunately, we are not ready for these measurements, are not equipped with tool set and devices.

We observed the explosive transition from amorphous to micricrystalline state in the Fe15Co60B10Si15 microwire produced by Ulitovskii-Taylor method at applying current pulse. The explosive character of the transition appears at achievement of a certain temperature by a sample and is accompanied by light flash and short-time increase in electric resistance. The observed features of the transition are: behavior of the average resistance of the sample and radiation detected by the photodiode can be explained by thermal effects associated with exothermal character of the process and the rate of Joule heating of a sample. The propagation velocity of the front in our experiments is about 1 m/s (length 5 mm, time 5 ms). Despite some ambiguity in parameters of the microwire, it is possible to transit quite smoothly from isothermal

regime to the explosive, which provides additional possibilities in studies of the essence of the process.

In conclusion, the authors are grateful to R. V. Kholin for assistance in the experimental work and to A. M. Orlov for development and design of the measuring block.

Literature

1. Шкловский В.А. // ЖЭТФ. 1982. Т.82. стр. 536.

2. Л.С. Палатник, М.Я. Фукс, В.М. Косевич. Механизм образования и субструктура конденсированных пленок. М.: Наука, 1972. 320 с.

3. K. Ohdaira, H. Matsumura. Flash-lamp-induced explosive crystallization of amorphous germanium films leaving behind periodic microstructures. Thin Solid Films. 2012. V. 524. p. 161-165.

4. Л.Н.Александров. Кинетика кристаллизации и перекристаллизации полупроводниковых пленок. Новосибирск: Наука, 1985. 224 с.

5. В.А. Шкловский, В.М. Кузьменко. Взрывная кристаллизация аморфных веществ. УФН. 1989. Т. 157, В. 2. С. 311–338.

6. L. Nikolova, M.J. Stern, J.M. MacLeod, B.W. Reed, H. Ibrahim, G.H. Campbell, F. Rosei, T. LaGrange, B.J. Siwick. In situ investigation of explosive crystallization in a-Ge: Experimental determination of the interface response function using dynamic transmission electron microscopy. J. Appl. Phys. 2014. V. 116. P. 093512.

7. O. Bostanjoglo, R. Liedtke. Tracing Fast Phase Transition Electron Microscopy. Phys. Stat. Sol. Ser. A. 1980. V. 60. P. 451-455.

8. V.M. Kuz'menko, T.P. Chernyaeva. Influence of internal stresses on the superconductivity of nanocrystalline vanadium films. Low Temp. Phys. 2005. V. 31, Is. 2. P. 111-115.

9. В.П. Скрипов, В.П. Коверда. Спонтанная кристаллизация переохлажденных жидкостей. М.: Наука, 1984. 232 с.

10. L. Nikolova, T. LaGrange, B.W. Reed, M.J. Stern, N.D. Browning, G.H. Campbell, J.C. Kieffer, B.J. Siwick, F. Rosei. Nanocrystallization of amorphous germanium films observed with nanosecond temporal resolution. Appl. Phys. Lett. 2010. V. 97, Is. 20. P. 203102.

11. L. Nikolova, T. LaGrange, M.J. Stern, J.M. MacLeod, B.W. Reed, H. Ibrahim, G.H. Campbell, F. Rosei, B.J. Siwick. Complex crystallization dynamics in amorphous germanium observed with dynamic transmission electron microscopy. Phys. Rev. B. 2013. V. 87. P. 064105.

12. V.A. Tulin, M.V. Astahov, A.O. Rodin, J. Magn. Magn. Mater. 258, Sp. Iss SI, p. 201-203, 2003

13. В.Ф. Гантмахер. Электроны в неупорядоченных средах. М. Физматлит, 2003.174 с.

RESEARCH OF PHASE TRANSFORMATION PRODUCTS IN HIGH STRENGTH STEELS BY ELECTRON BACKSCATTER DIFFRACTION (EBSD)

E.A. Yashina, A.A. Zisman, D.Sc., S.N. Petrov, Ph.D.

CRISM "Prometey", St. Petersburg, 191015, Shpalernaya str., 49, npk3@crism.ru

Abstract: *In the present work, in order to evaluate the metastable structural state of high-strength steel immediately after the phase transformation as well as during the following tempering, the SEM-based EBSD is employed. The lattice orientation gradient in the alfa-phase of steel is mapped by a standard GAM function ("grain average misorientation") that makes it possible to identify various types of martensite and bainite distinguishable in the dislocation density and phase stresses. The GAM sensitivity to the crystal curvature not only allows one to tell between different types of alfa-phase in the non-equilibrium quenched state but also reveals their change during tempering.*
KEYWORDS: *NON-EQUILIBRIUM QUENCHED STRUCTURES, HIGH-STRENGTH STEEL, MARTENSITE, BAINITE, EBSD, LATTICE ORIENTATION GRADIENT, GAM*

1. Introduction

Complex bainite-martensitic structure of high-strength cold-resistant steels, which is a result of phase transformation in quenching, provides a unique combination of properties. Analysis of it remains an actual task since some species of α-phase, slightly differing in morphological characteristics, vary considerably in dislocations density and hence their contribution to the strength of material. This applies both to non-equilibrium as-quenched state and the structure evolution during subsequent tempering. Thus, studies of the final structure require new means of objective recognition of the α–phase types, and their volume fractions estimation. Low resolution of optical microscopy does not allow solving this problem, and transmission electron microscopy due to its locality does not provide evaluation on statistically representative volumes of steel.

In recent years the possibilities of panoramic crystallographic analysis based on scanning electron microscopy (SEM) dramatically increased in practical metallography owing to application of electron backscatter diffraction (EBSD) method. It provides a resolution of about 100 nm and an angular accuracy of about 0.1° to map the local crystal orientations on conventional sections [1]. However, in order to distinguish between the types of α-phase with different density of defects in the lattice and degree of its elastic distortion, some alternative functions of EBSD data are used [2, 3].

2. Materials and research techniques

Under consideration is high strength low carbon steel 09CrNi4MoCu with complex bainite-martensitic structure after quenching. By varying the cooling rate of dilatometric samples (diameter 5 mm, length 10 mm) the required structures with different ratios of the structural components were formed. Samples from rolled plates were heated in a vacuum chamber of dilatometer DIL 805 with rate of 5 °C/s to a temperature of 950 °C and kept at this temperature for 300 s and then cooled with rates 1 and 30 °C/s.

Similarly, the sections from rolled steel 09CrNi4MoCu in quenched condition and after tempering at temperatures of 625 °C (8 h) and 660 °C (1 and 6 h) were examined.

The sections were prepared by standard metallographic procedures, and the fine paste of amorphous aluminum oxide was applied at the final stage to reduce surface hardening. Panoramic EBSD analysis was carried out using SEM QUANTA 200 3D with scanning step 0.10 microns, the software EDAX-TSL was applied to determine the local orientations.

The standard option of the software package TSL OIM Analysis, namely the GAM-function, was used to evaluate the lattice curvature in each crystal (laths or blocks) of the transformed structure. This function characterizes the average angle of the lattice rotation between adjacent measurement points within the area, separated from the environments by boundary with misorientation of not less than specified tolerance angle θt. In the present work the value θt=5º was used that is close to the smallest relative rotation angle between the possible variants of orientation relationships (OR) between α–phase and a parent austenite lattice [4, 5]. On the one hand, this excludes the contribution of boundaries between different martensite or bainite crystals to the GAM-value, i.e. reflects only their own curvature; on the other hand, each crystal is characterized as a whole, because low-angle boundaries ($\theta<\theta_t$) inside it are thus ignored.

3. Results and discussion

Dilatometric experiments

Analysis of dilatometric curves (Fig. 1) shows that at a cooling rate 30 °C/s transformation starts at temperature of approximately 400 °C, and the most part of it takes place below Ms (for steel 09CrNi4MoCu martensite start temperature Ms is ~ 390 °C); at a cooling rate 1 °C/s transformation starts in bainite region at 440 °C and finishes at approximately 340 °C.

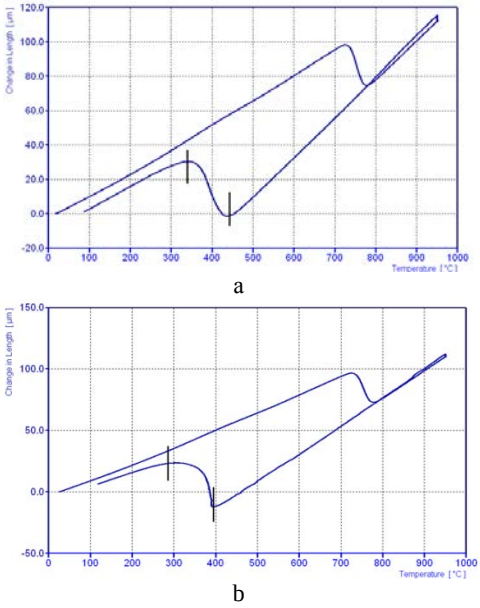
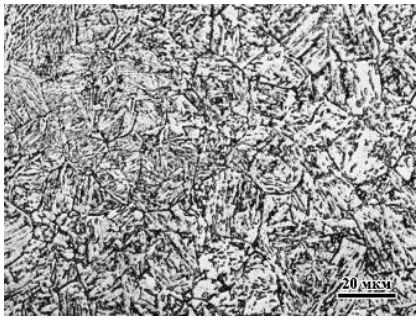
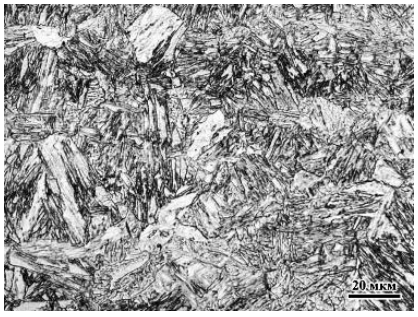


Fig. 1 – *Dilatometric curves of steel 09CrNi4MoCu cooled with rate 1 (a) и 30 °C/s (b)*

Metallographic sections of steel 09CrNi4MoCu proved that at a cooling rate 1 °C/s microstructure consists of bainite and martensite (Fig. 2, a), whereas at a cooling rate 30 °C/s microstructure represents predominately martensite with a small part of bainite (Fig. 2, b).



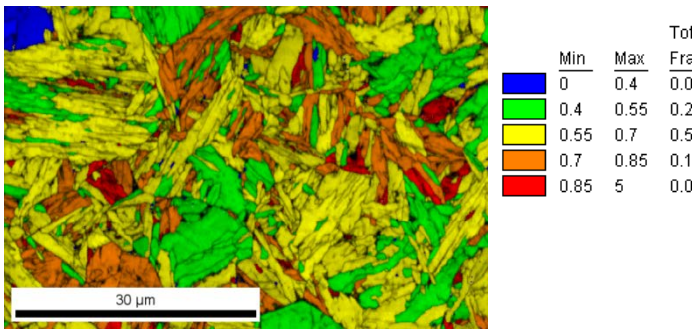
a



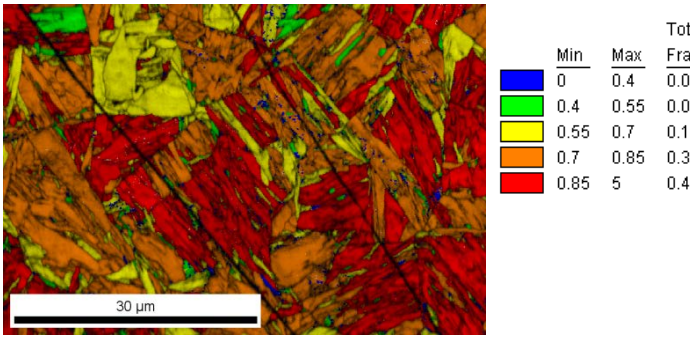
b

Fig. 2 *- Microstructure of steel 09CrNi4MoCu after cooling at a rate 1 (a) and 30 °C/s (b)*

Fig. 3 represents lattice curvature (GAM) maps after cooling of steel at a rate 1 (a) and 30 °C/s (b). To image the lattice curvature, the color scale [3, 6] was used together with previous data on its relation with different types of α–phase after quenching. Typical lattice curvature magnitude lies in ranges 0,4-0,7° and 0,7-1,25° for bainite and martensite, respectively. With this scale it was identified that after quenching with cooling rate 1°C/s, steel 09CrNi4MoCu contains 75% of bainite and 23% of martensite, whereas at cooling rate 30 °C/s – microstructure consists of 78% martensite and 20% bainite.



a



b

Fig. 3 *- Lattice curvature maps of steel 09CrNi4MoCu after cooling at a rate 1 (a) and 30 °C/s (b)*

Detailed research of features of phase transformation products after cooling at rate 1 and 30 °C/s was carried out in terms of lattice curvature spectrum (Fig. 4).

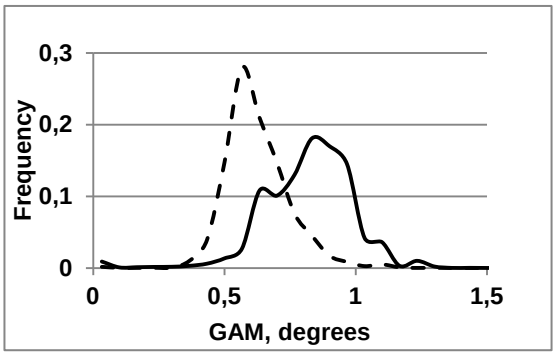


Fig. 4 *– Lattice curvature spectrum of steel structure after cooling at rate 1 (dashed line) and 30 °C/s (solid line)*

One peak, corresponding to bainite-martensite structure is observed for cooling rate 1°C/s. Possibly, high start transformation temperature leads to formation of bainite and so-called 'self-tempered' martensite, both having close dislocation densities. It might be supposed that the specific shape of spectrum is due to overlapping of contributions of two structural components.

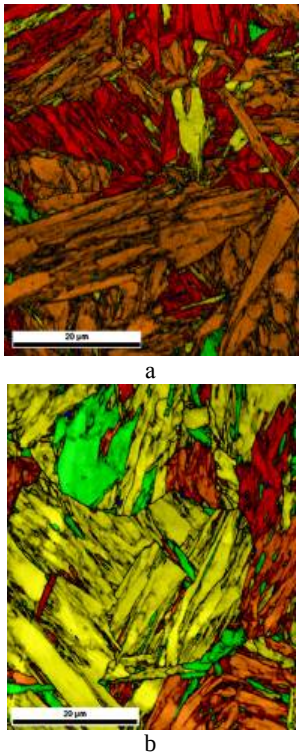
Raise of cooling rate to 30°C/s leads to increase of average lattice curvature from 0,62° up to 0,81°, and the separation of structural components by lattice curvature is observed. This splitting seems to correspond to severely distorted lath martensite, 'self-tempered' martensite and bainite.

Thus, panoramic EBSD analysis proves to be an efficient means for quantitative attestation of bainite-martensitic structures of high strength steels. This permits both to distinguish between structural α–phase species differing in lattice distortion and to study the structural features of phase transformation products in terms of lattice curvature spectrum.

Research of industrial probes

The developed method was verified on specimens cut from 09CrNi4MoCu steel plates after quenching in industrial conditions. Lattice curvature map of steel 09CrNi4MoCu after quenching (Fig. 5, a) reveals the prevalent fraction of martensite in structure. Tempering at 625°C leads to abrupt decrease of lattice curvature level (Fig.5, b), so that the lattice curvature of tempered martensite turns to be close to that of bainite.

For detailed analysis, it should be taken into consideration that structural species of α–phase differing in density of defects and degree of elastic distortion, and consequently in lattice curvature, change during tempering in different ways (Fig.6, a). The quenched microstructure proves to have bimodal distribution with main martensite peak and relatively small peak due to insignificant fraction of bainite.



a

b

Fig.5 *- Lattice curvature maps of steel 09CrNi4MoCu after quenching (a) and tempering at 625°C (b)*

During tempering, the significant change of spectrum shape is observed along with the expected total decrease of lattice curvature. If to ignore the weakest peculiarities, the martensite peak (in contrast with bainite) is splitted by the slow shift of its right part corresponding to the highest dislocation density. It may seem strange because the elastic energy, i. e. *the driving force* for structural evolution must be maximal. At the same time, from the kinetic point of view this split may be expected, since the excessive density of dislocations complicates their rearrangement (annihilation). Along with the influence of initial dislocation density, the observed effect may be explained by different width of martensite laths, resulting in different spectrum evolutions during tempering. Although the result of the competition of all above mentioned factors depending on tempering conditions is still hardly predictable, the example demonstrates efficiency of lattice curvature spectrum as a representative characteristic for structural states of α–phase.

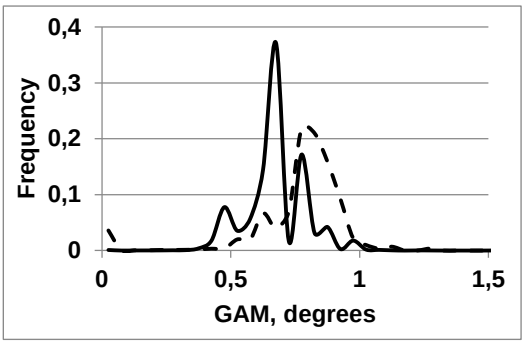
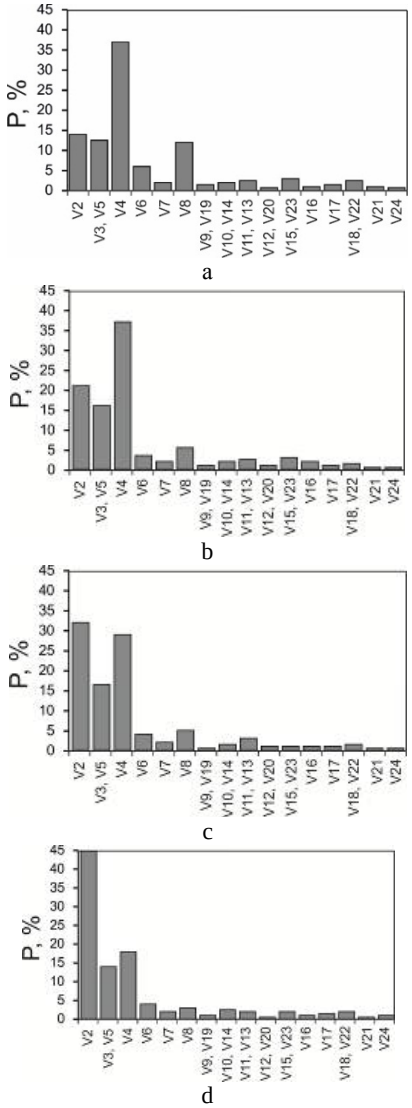


Fig.6 *– Lattice curvature spectrum after quenching (dashed line) and tempering at 625°C (solid line) of steel 09CrNi4MoCu*

Evolution of inter-variant misorientation spectrum in tempering

Martensitic and bainitic microstructures are reliably recognized, according to [4, 5], by spectrum of inter-variant misorientations after quenching, however the research of tempering kinetics in a similar way has not been implemented yet. Seemingly, this approach was ignored due to the common assumption that the tempering effect involves only the reduction of dislocation density and carbon redistribution, whereas the packet-lath structure remains unchanging.

Orientation relationship (OR), determined in steel according to [6] is characterized by Euler angles (27.89° 8.81° 18.25°) for rotation of elementary cubic cells during γ-α transformation and corresponds to inter-phase rotation angles of 1.59° и 2.58° for close-packed planes and directions, relatively. Fig. 7 shows variant pairing frequency diagrams after quenching (a), tempering at 625°C for 8 h (b), at 660°C for 1 h (c) and 6 h (d). After quenching (Fig.7, a) the typical spectrum for martensitic structure was obtained [4, 5], however tempering led to an unexpectedly strong evolution. First of all, increase of variant pairing V2/V1 fraction and decrease of V4/V1 fraction should be mentioned. The longest tempering at 625ºC resulted in the weakest effect comparing to tempering at 660ºC for 1 h. Increase of tempering time up to 6 h at 660ºC (Fig.7, d) led to notable growth of boundaries, corresponding to variant pairing V2/V1.



a

b

c

d

Fig. 7 *- Variant pairing frequency diagrams after quenching (a), tempering at 625°C for 8 h (b), at 660°C for 1 h (c) and 6 h (d)*

The revealed regularities indirectly evidence that tempering leads to the growth of martensitic crystals, which orientation corresponds to V2/V1 variant paring.

4. Conclusions

The present work shows that EBSD analysis is an efficient means for quantitative attestation of complex bainite-martensitic structures of high strength steels. It permits to distinguish between structural species of α–phase differing in lattice distortion and dislocation density. In particular, volume fractions and the distribution of martensite and bainite can be derived from lattice curvature maps. Rate of softening of different types of α–phase in tempering is also manifested by evolution of curvature spectrum. Thus, different resistance of bainite and martensite to tempering (softening) is revealed.

EBSD data processing enables to determine the inter-phase orientation relationship and to analyze variant pairing at the boundaries. On this base, the important tempering effect was discovered in steel under investigation – the increase of grain boundaries with V2/V1 variant pairing.

This work is financially supported by Board of Education and Science of Russian Federation, grant №14.579.21.0003, unique identifier RFMEFI57914X0003.

References

1. Adams B.L., Wright S.I., Kunze K. Orientation imaging: The emergence of new microscopy // Metall. Trans.-A. 1993. Vol. 24 (4). P. 819-831.

2. Wilkinson A.J., Meaden G., Dingley D.J. High-resolution elastic strain measurement from electron backscatter diffraction patterns: New level of sensitivity // Ultramicroscopy. 2006. Vol. 106. P. 307-313.

3. Zisman A.A., Petrov S.N., Ptashnik A.V. Quantitative Verification of High-Strength Alloyed Steel Bainite-Martensite Structures by Scanning Electron Microscopy Methods // Metallurgist. 2014. Vol.11. P. 91–95.

4. Miyamoto G., Iwata N., Takayama N., Furuhara T. Quantitative analysis of variant selection in ausformed lath martensite // Acta Mater. 2012. Vol.60. P. 1139–1148.

5. Takayama N., Miyamoto G., Furuhara T. Effects of transformation temperature on variant pairing of bainitic ferrite in low carbon steel // Acta Mater. 2012. Vol.60. P. 2387-2396.

6. Zolotorevsky N.Yu., S.N. Panpurin S.N., A.A. Zisman A.A., S.N. Petrov S.N. Effect of ausforming and cooling condition on the orientation relationship in martensite and bainite of low carbon steels // Mater. Characterization. 2015. Vol. 107. P. 278-282.

SYNTHESIS AND CHARACTERIZATION OF ZnO NANOCRYSTALS IN STARCH MATRIX

СИНТЕЗ И ОПРЕДЕЛЕНИЕ ХАРАКТЕРИСТИК ZnO НАНОКРИСТАЛЛОВ В МАТРИЦЕ КРАХМАЛА

Assos. Prof. Dr. Vasileva P.
Faculty of Chemistry and Pharmacy, University of Sofia "Saint Kliment Ohridski", Bulgaria
E-mail: pvasileva@chem.uni-sofia.bg

Absract/Резюме: *Gel matrix of the natural polymer starch has been employed as template for the preparation of ZnO nanocrystals via solution-solid technique. The template offers selective binding sites for Zn(II) under aqueous conditions. Controlled solvent-exchange, further isolation of solid product by microfiltration and drying, and subsequent removal of the template backbone enable the synthesis of spatially separated ZnO nanocrystals. The crystalline character and near narrow particle size distribution pattern have been confirmed through powder XRD measurements and TEM with SAED observation. The morphology, surface and optical properties of ZnO sample were characterized by SEM observation, BET-surface area, UV–Vis and PL spectra. The UV photocatalytic activity of ZnO nanocrystals was studied by analyzing the degradation of methylene blue in aqueous solution. The nanosized ZnO sample showed greater photocatalytic activity than commercial TiO_2 (P25) photocatalysts. The size and shape factor seems to be of great importance in the observed photocatalytic performance.*
KEYWORDS: ZINC OXIDE, NANOCRYSTALS, STARCH TEMPLATE, SOLUTION-SOLID TECHNIQUE

1. Introduction/Введение

Nanoparticles of semiconductors such as titanium dioxide (TiO_2), zinc oxide (ZnO), iron oxide (Fe_2O_3), and cadmium sulfide (CdS) have attracted extensive attention as a photocatalyst for the degradation of organic pollutants in water and air [1,2]. The dispersion and surface area of oxide nanomaterials, which depend on the synthesis method, are important factors for determining its photocatalytic activity [3]. The design and synthesis of such nanoparticles have centered on techniques such as sol–gel [4], chemical coprecipitation [5], microemulsion [6] etc. Most of these techniques result in aggregation of nanoparticles during synthesis. Copolymer templates have been efficiently used to host chemical reactions. They have the advantage of avoiding nanoparticle clustering and also providing stable frameworks against chemical degradation [7]. Use of copolymer templates has been reported for the synthesis of iron oxide nanoparticles such as maghemite [8], cobalt ferrite [9] and magnetite [10]. There is an increasing interest in the use of green resources for nanoparticle synthesis. The metal nitrate was added into the starch solution, and heated the mixture to form gel; the porous metal oxide was prepared when the starch was burnt off at air. Starch has been reported as a capping agent during the preparation of iron oxide through the precipitation of ferric salts as its hydroxide using triethylamine [11], or by precipitating amixture of ferric and ferrous salts [12]. Polysaccharides have also been employed to modify the surface characteristics of the nano iron oxides generated [13]. Starch gel has been used as template to obtain macroporous material and film [14, 15].The work presented here reports the use of gel matrix of the natural polymer starch as template for the synthesis of ZnO nanocrystals via solution-solid technique. The template offers selective binding sites for Zn(II) under aqueous conditions. Controlled solvent-exchange, further isolation of solid product by microfiltration and drying, and subsequent removal of the template backbone by controlled heat treatment enable the synthesis of spatially separated ZnO nanocrystals. X-ray Diffraction (XRD), scanning and transmission electron microscopy (SEM and TEM), BET-surface area, UV-Vis absorption and photoluminescent (PL) spectroscopy have been used to characterize the nanoparticles. The UV photocatalytic activity of ZnO nanocrystals was studied by analyzing the degradation of methylene blue (MB) in aqueous solution.

2. Preconditions and means for resolving the problem/Предпосылки и средства для решение проблемы

Synthesis of nanosized ZnO without using a protective agent was a problem. Due to the high polarity of water, ZnO nanoparticles cause an immediate agglomeration during synthesis with water due to the Vander wall forces of attraction. To prevent agglomeration, soluble starch has been used in the literature. The quick helical forms of the soluble starch protect and prevent the ZnO nanoparticles from agglomeration by the action of steric or electrostatic hindrance and stabilizing the ZnO nanoparticles. Unlike earlier reported methodologies where natural polysaccharides and polymers have been employed for encapsulation or capping of metal oxides generated by precipitation methods [10–13], this work reports the binding of the Zn(II) center to sites in the polymer, thereby obtaining a spatial separation of the Zn(II) centers. The long-chain biopolymer forces the nucleation and the initial growth of the crystallites to occur preferentially on polysaccharides backbone, inside regions of high concentrations of starch and Zn(II), controlling the self-assembly of the 3-D architectures (Fig. 1).

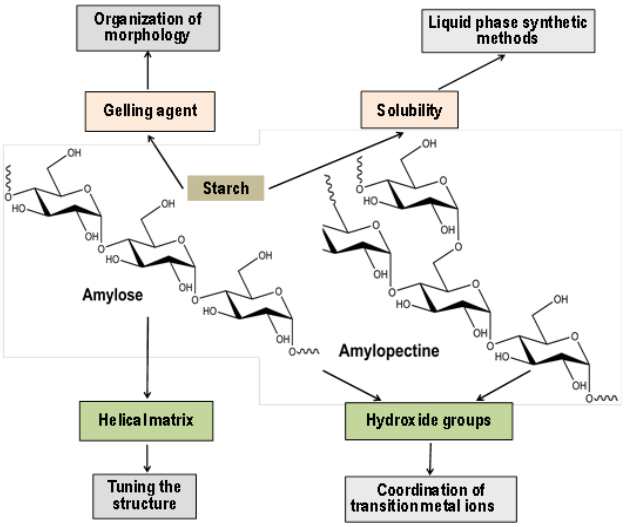


Figure 1. Role of starch template

3. Experimental part/Експериментальная част

3.1. Synthesis/Синтез (Fig. 2)

All reagents and solvents were of analytical grade (Sigma-Aldrich) and were used as received without further purification. In a typical synthesis, soluble starch (30 g) was dissolved in 100 mL hot distilled water. Zinc nitrate, $Zn(NO_3)_2.6H_2O$, 29.749 g (0.1 mol), was added in the above solution. During heating on a

magnetic stirring and heating apparatus at 90-100 ◦C under stirring, the template—zinc(II) mixed solution gradually became highly viscous. The gel solution was maintained at that temperature for 180 min, after which it was cooled to room temperature and aged at 4 °C for 48 h (*solution-phase stage*). Then the solvent was replaced with ethanol and the "solid" formed was separated from the mother solution by microfiltration (MILIPORE 0.2 μm); the sample was denoted ZnO_F. For comparison, other solid sample is obtained by decantation of the mother solution instead of microfiltration; the sample was denoted ZnO_NF. The solid was dried at 80°C for overnight and then calcinated from room temperature to final temperature (600 ◦C) in an air atmosphere. The product was kept at the maximum temperature for 240 min (*solid-phase stage*).

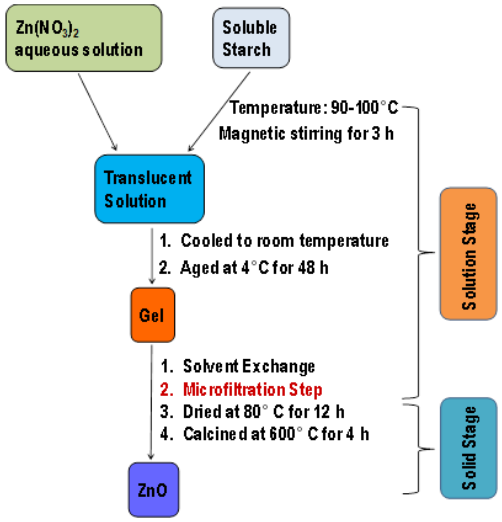


Figure 2. Schematic procedure for synthesis of ZnO

3.2. Characterization/Определение характеристик

The morphological characterization was carried out by scanning electron microscope (SEM) observation using a JEOL JSM-5510 apparatus. The TEM investigations were performed by TEM JEOL 2100 with an accelerating voltage of 200 kV. The specimens were prepared by dispersing the nanocomposite powder in ethanol under ultrasonic treatment for 6 min. The suspensions were dripped on standard carbon/Cu grids. The specific surface area of the sample was determined by nitrogen adsorption at the boiling temperature of liquid nitrogen (77.4 K) using a conventional volume-measuring apparatus. The X-ray diffraction (XRD) analysis was carried out on a Siemens powder diffractometer model D500 using CuKα radiation in a 2Θ diffraction interval of 25° to 85°. The refinement with Powder Cell software was used to identify the crystallographic phases present and to calculate the crystal lattice parameters and crystallite sizes (by Scherrer equation) from the XRD patterns. The UV-Vis absorbance spectra and photoluminescent spectra were recorded using Evolution 300 spectrometer (Thermo Scientifc, USA) and Perkin Elmer MPF44 spectrofluorimeter, respectively. All measurements were performed in a 1 cm quartz cell.

3.3. Photocatalytic test/Фотокаталитический тест

The photocatalytic activities of the obtained ZnO samples was evaluated evaluated in the photocatalytic degradations of methylene blue (MB) dye in aqueous solution. In each experiment, 0.1 g catalyst was dispersed in 100 mL of an aquesous solution of MB (10 mg/L). Prior to UV light illumination, the suspension was magnetically stirred in the dark for 30 min to reach adsorption equilibrium. After stirring in the dark, the suspension was irradiated with 18-W UV light-tube (365 nm) under continuous magnetic stirring. At a given time interval, the suspension solution was collected to measure the UV-Vis absorbance of MB in order to measure the residual concentration of MB. Before analysis, the aqueous samples were centrifuged at 10 000 rpm to remove any suspended solid ZnO particles. As a comparison, the photocatalytic activity of commercially available Degussa P25 TiO_2 was also tested under the same experimental conditions.

4. Results and discussion/Результаты и обсуждение

4.1. SEM characterization/SEM характеристик

SEM analysis of the ZnO_NF and ZnO_F samples was done and the micrographs are presented in Fig. 3a, b and Fig. 3c, d, e, respectively. Fig. 3a clearly indicates that a network formation from agglomerated nanoparticles has taken place at ZnO-NF sample. Similarly, in Fig. 3b shows that a particle aggregation at the sample ZnO_F has been taken place. From the micrographs, it can be guessed that the particles of both samples are irregular in shape with the presence of nanorods in ZnO_F sample, but it is not possible to predict the exact sizes of the individual particles, which can be done through TEM analysis. The surface area studies showed that the prepared ZnO_F and ZnO_NF samples had specific surface area of 49 m^2/g and 29 m^2/g, respectively.

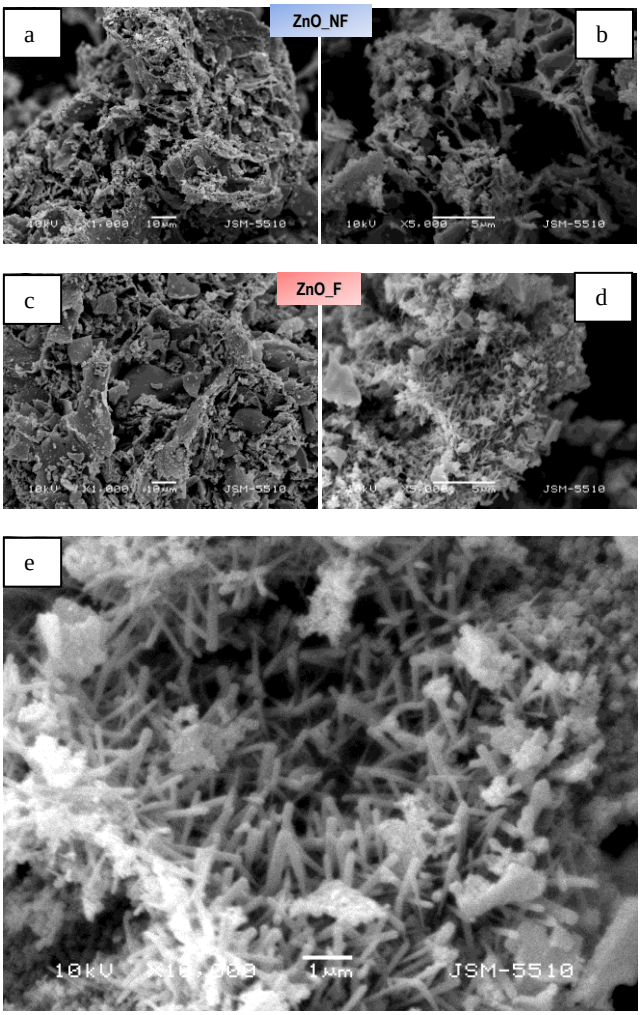


Figure 3. SEM micrographs of ZnO samples obtained with and without microfiltration step

4.2. TEM and XRD characterization/TEM и XRD характеристик

The morphology and structure of the ZnO_F sample were further investigated by TEM. It is clearly seen from the TEM image (Fig. 4) that ZnO_F powder consists of both nanoparticles and nanorods as seen in the SEM. The corresponding selected-area electron diffraction (SAED) pattern shows spotty rings pattern without any additional diffraction spots and rings of second phases, revealing highly crystalline ZnO wurtzite structure. All the XRD peaks in the X-ray diffraction patterns of the ZnO samples are indexed by hexagonal wurtzite structure of ZnO (JCPDS card 36-1451 (Fig. 5), which is in agreement with electron diffraction results (inset in Fig. 5). The peak broadening in the XRD patterns clearly indicates that small nanocrystallites (with average sizes of 21 nm and 24 nm for ZnO_F and ZnO_NF, respectively) are present in the samples. Broadening along with decreasing the intensity of diffraction peaks for the sample obtained with microfiltration step is observed due to the decreased crystallite size of ZnO_F samples.

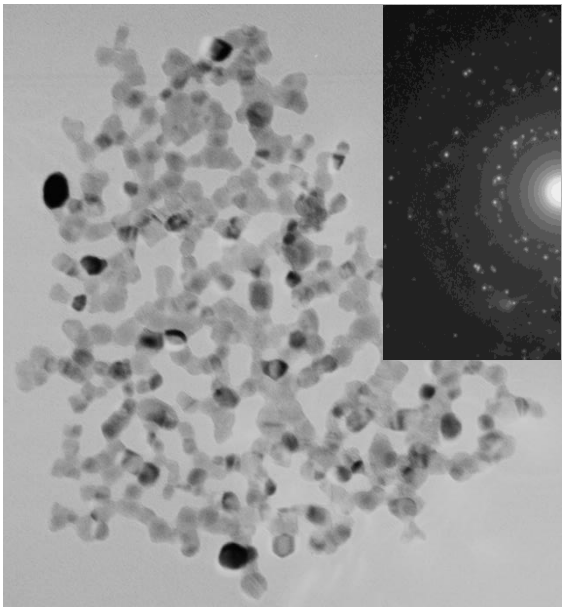


Figure 4. TEM micrograph of ZnO_F sample; inset: corresponding selected-area electron diffraction (SAED) pattern

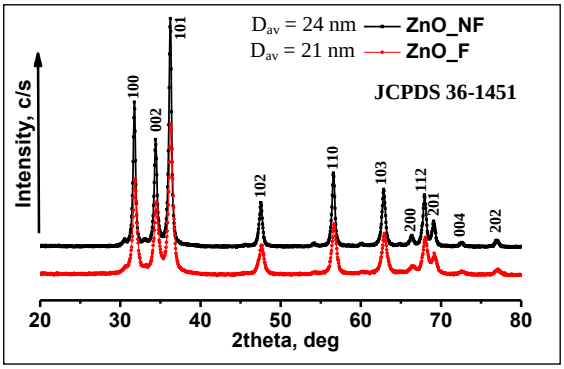


Figure 5. XRD patterns of ZnO samples

4.3. UV-Vis absorption spectra

The prepared ZnO nanopowders were first dispersed in double distilled water and then UV-VIS absorption characteristics of the ZnO nanoparticles were measured (Fig. 6). The excitonic absorption bands is observed due to the ZnO nanoparticles at 369 nm and 374 nm for ZnO_F and ZnO_NF, respectively, which lies below the bandgap wavelength of 388 nm (E_g = 3.2 eV) of bulk ZnO.

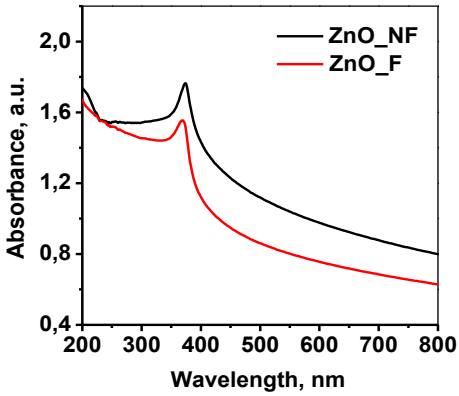


Figure 6. UV-Vis absorption spectra of ZnO samples

4.4. Photoluminescent spectra

Room temperature PL spectra of the nanocrystalline ZnO_F sample measured in dichloromethane and ethanol dispersions are shown in Fig. 7a and Fig. 7b, respectively. Xenon laser of 325 nm was used as an excitation source.

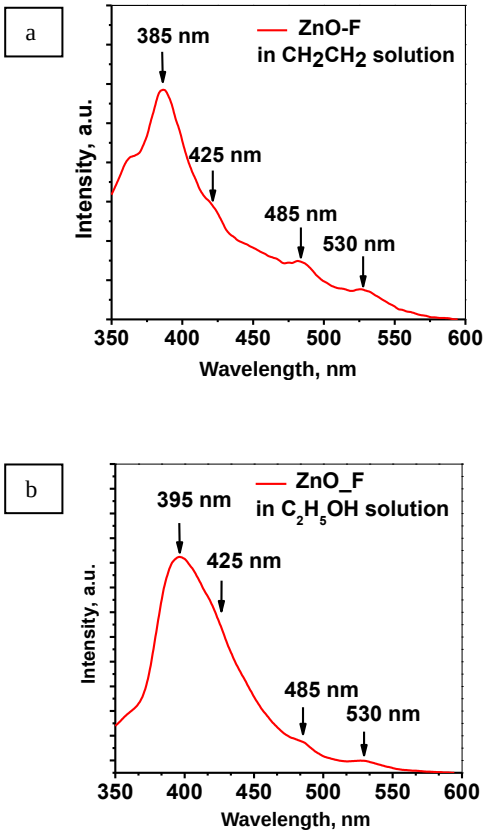


Figure 7. PL spectra of ZnO_F sample

Both PL spectra mainly consists of four emission bands: a strong UV emission band at ~385 nm (for $C_2H_2Cl_2$ dispersion) and 395 nm (for C_2H_5OH dispersion), a weak blue band at ~425 nm, a week blue–green band at 485 nm, and a green band at 530 nm [17]. The strong UV emission corresponds to the exciton recombination related near-band edge emission of ZnO [18-21]. The weak blue and weak blue–green emissions are possibly due to surface defect in the ZnO powders as in the case of ZnO nanowires reported by Wang and Gao [22]. The week green band emission corresponds to the singly ionized oxygen vacancy in ZnO, and this emission results from the recombination of a photo-generated hole with the singly ionized charge state of the specific defect [23–25]. The low intensity of the green emission

may be due to the low density of oxygen vacancies during the preparation of the ZnO powders, whereas the strong room temperature UV emission intensity should be attributed to the high purity with perfect crystallinity of the synthesized ZnO_F sample.

4.5. Photocatalytic performance

With irradiation under UV light (365 nm), the characteristic absorption of MB at λ = 665 nm decreases gradually, and finally disappears within 90 min in the presence of all nanocatalysts studied, while in the absence of light or catalyst, the concentration of MB has no obvious change for long time (Fig. 8a). The results show that both light and catalyst are necessary for the effective photodegradation of MB dye. Photocatalytic tests reveal faster initial degradation with ZnO nanocrystals obtained with microfiltration step than ZnO sample obtained without microfiltration step in spite of higher UV-Vis absorption of ZnO_NF. The ZnO nanocrystals obtained with microfiltration step have shown to be better photocalysts for the degradation of methylene blue dye under UV irradiation, compared to the Degussa P-25 TiO_2 commercial photocatalyst. The degradation percentage of MB is about 60% after irradiation for 30 min, and the total degradation of MB by all nanocatalysts studied is achieved for 90 min (Fig. 8b). The result implies that the ZnO_ F nanocatalyst, prepared with microfiltration step, is a superior photocatalyst to Degussa P25 for photodegradation of the dye.

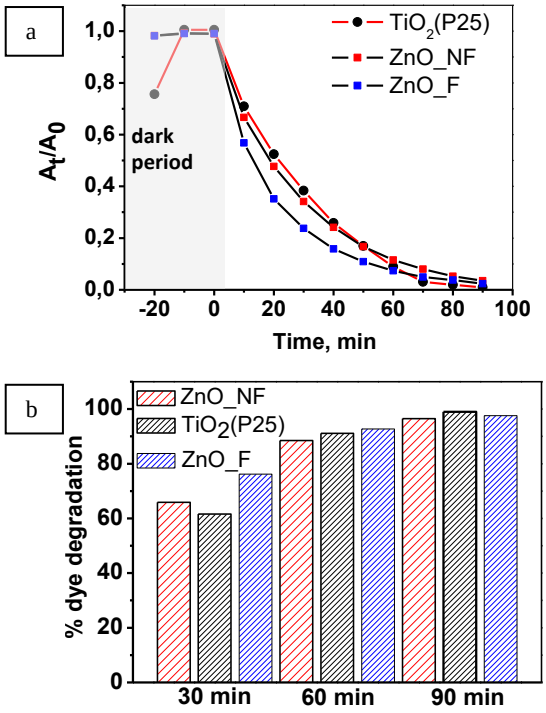


Figure 8. Photodegradation curves of MB by different catalysts

5. Conclusions/Заключения

5.1. Gel matrix of the natural polymer starch has been employed as template for the preparation of ZnO nanoparticles via solution-solid technique. Controlled solvent-exchange, further isolation of solid product by microfiltration and drying, and subsequent removal of the template backbone enable the synthesis of spatially separated zinc oxide nanocrystals with smaller crystallite size and higher surface area.

5.2. The crystalline character of ZnO and near narrow particle size distribution pattern have been confirmed through powder XRD measurements and TEM with SAED observation. The average crystallite size of the particles obtained was found to be in the range of 21-24 nm irrespective of the nature of the template. The morphology, surface and optical properties of ZnO samples were characterized by SEM observation, BET-surface area, UV–Vis and PL spectra.

5.3. The UV photocatalytic activity of zinc oxide nanoparticles was studied and compared with TiO_2 (P25) by analyzing the degradation of methylene blue (MB) in aqueous solution. The nanosized ZnO sample exhibited efficient photocatalytic activities for the degradations of aqueous solution of MB. The size and shape factor seems to be of great importance in the observed photocatalytic performance.

6. Literature/Литература

[1] G. Schmid, Nanoparticles, Wiley–VCH Verlag GmbH & Co. KGaA, 2004.

[2] R. W. Siegel, in: F. F. Fujita (Ed.), Nanophase Materials: Synthesis, Structure, and Properties, Springer Series in Material Science, vol. 27, Springer-Verlag, 1994.

[3] D. Li, H. Haneda, Chemosphere 51 (2003) 129.

[4] M. M. Sagrario, L. A. Gracia-Cerda, T. J. R. Lubian, Mater. Lett. 59 (2005) 1056.

[5] B. R. Galindo, A. O. Valenzuela, L. A. Gracia-Cerda, R. O. Fernandez, M. J. Aquino, G. Ramos, Y. H. Madeira, J. Magn. Mag. Mater. 294 (2005) 33.

[6] Z. L. Liu, X. Wang, K. L Yao, G. H. Du, Q. H. Lu, Z. H. Ding, J. Tao, Q. Ning, X. P. Luo, D. Y. Tian, D. Xi, J. Mater. Sci. 39 (2004) 2633

[7] P. A. Dresco, V. S, Zaitsev, R. J. Gambino, B. Chu, Langmuir 15 (1999) 1945

[8] K. Sunderland, P. Brunetti, L. Spinu, J. Fang, Z. Wang, W. Lu, Mater. Lett. 58 (2004) 3136.

[9] L. A. Gracia-Cerda, R. Chapa-Rodriguez, J. Bonilla-Rios, Polymer Bull. 58 (2007) 989.

[10] H. Lin, Y. Watanabe, M. Kumura, K. Hanabusa, H. Shirai, J. Appl. Polymer Sci. 87 (2003) 1239.

[11] P. S. Chowdhury, P. R. Arya, K. Raha, Synth. React. Inorg. Met. 37 (2007) 447.

[12] D. M. Kim, M. Mikhaylova, F. H. Wang, J. Kehr, B. Bjelke, Y. Zhang, T. Tsakalakos, M. Muhammed, Chem. Mater. 15 (2003) 4343.

[13] Y-Y Liang, L-M Zhang, W. Li, Colloid Polym. Sci. 285 (2007) 1193.

[14] B. J. Zhang, S. A. Davis, S. Mann, Chem. Mater. 14 (2002) 1369.

[15] W. Shen, Z. Li, H. Wang, Y. Liu, Q. Guo, Y. Zhang, J. Hazard. Mater. 152 (2008) 172.

[16] S. Chen, J. Feng, X. Guo, J. Hong, W. Ding, Mater. Lett. 59 (2005) 985.

[17] S. Maensiri, P. Laokul, V. Promarak, J. Cryst.Growth 289 (2006) 102.

[18] K. Vanheusden, W. L. Warren, C. H. Sesger, D. R. Tallant, J. A. Voigt, B. E. Gnage, J. Appl. Phys. 79 (1996) 7983.

[19] V. Stikant, D. R. Clarke, J. Appl. Phys. 83 (1998) 5447.

[20] S. C. Lyu, Y. Zhang, H. Ruh, H. Lee, H. Shim, E. Suh, C. J. Lee, Chem. Phys. Lett. 363 (2002) 134.

[21] L. Bergman, X.B. Chen, J.L. Morrison, J. Huso, A.P. Purdy, J. Appl. Phys. 96 (2004) 675.

[22] J. Wang, L. Gao, Solid State Commun. 132 (2004) 269.

[23] S. Monticone, R. Tufeu, A.V. Kanaev, J. Phys. Chem. B 102 (1998) 2854.

[24] Y. Li, G.S. Cheng, L.D. Zhang, J. Mater. Res. 15 (2000) 2305.

[25] B. D. Yao, Y. F. Chan, N. Wang, Appl. Phys. Lett. 81 (2002) 757.

Acknowledgement: to Sofia University Scientific Fund - Project 37/2016.

ANALYSIS OF THE EUTECTOID TRANSFORMATION INTO CARBON STEEL ON THE BASIS OF POSITIONS OF NON-EQUILIBRIUM THERMODYNAMICS

АНАЛИЗ ЭВТЕКТОИДНОГО ПРЕВРАЩЕНИЯ В УГЛЕРОДИСТОЙ СТАЛИ НА ОСНОВЕ ПОЛОЖЕНИЙ НЕРАВНОВЕСНОЙ ТЕРМОДИНАМИКИ

Dr. S. V. Bobyr [1], Prof. V. I. Bol'shakov [2], S.A. Sharfnadel[3],
Z. I. Nekrasov Institute of ferrous metallurgy[1], Prydniprovska state Academy of building and architecture [2], Department of science of investment trust[3] – Ukraine

Abstract: *The non-equilibrium thermodynamics analysis of the eutectoid transformation is executed into carbon steel. Onsager's equations of motion are built for the model thermodynamics system describing eutectoid transformation. Dependences of basic kinetic parameters of process are expected are speeds of height of pearlite and inter-plates distance from the size of subcooling became for the stationary process of eutectoid transformation.*

Keywords: *Non-Equilibrium Thermodynamics, Eutectoid Transformation, Diffusion, Equations Of Motion, Carbon Steel*

1. Introduction

In steel and cast iron, the kinetics of transformation of austenite largely determined by the diffusion of carbon, which allows them to refer to transformations controlled by diffusion [1-3]. Eutectoid transformation of austenite, as a kind of diffusion transformation, associated with a sharp change in the composition of the phases and the formation of colonies or aggregates of the two phases [3]. The value of S_0 perlite is the most important parameter for most of the steels does not depend on the grain size of austenite and varies from 1000 to 100 nm. (Fig. 1) [1, 8].

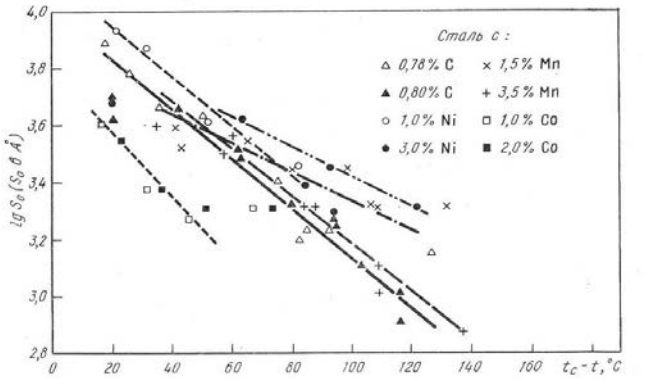


Fig.1. *The dependence of the average inter-plates distance of perlite from the size of subcooling to steels of different composition [1, 8].*

When the eutectoid decomposition of austenite the gain in free energy due to the conversion of austenite into perlite should be sufficient to cover the costs of education developed the interface between ferrite and cementite.

Accordingly, Zener derived the ratio:

$$S_0 = 2T\sigma/\rho Q\Delta T, \qquad (1)$$

An important kinetic characteristic of the eutectoid transformation of austenite is the growth rate of pearlite v. The value of growth rate was obtained by Mail [4] in the form: v = KS0-1. Zener received the expression for the growth rate of pearlite based mainly on considerations of dimensionality and some physico-chemical principles [5]. They were also justified the most general dependence of the rate of growth of pearlite from a temperature:

$$v \sim \Delta T^2 exp(-Q/RT). \qquad (2)$$

Development of the model was performed by Zener Hillerton subject to the conditions of equilibrium defined by surface free energy [6].

Experimental results show, however, that the measured values inter-plates distance perlite is much greater than those values which give the model of Zener and Hillert [4, 7].

Onsager suggested [8] that the determinant of the growth rate of pearlite is diffusion in the ferritic phase, and Turnbull considered the diffusion along the boundaries of the colonies [9]. Kahn found that it is impossible to reach an equilibrium redistribution of the components in the perlite, however it is possible to calculate the growth rate and the degree of redistribution components, if known, the distance between the plates [10]. You still want a physical principle to fix this distance.

2. Preconditions and means for resolving the problem

In [11, 12] as such a principle was used the law of conservation of energy during transformation of austenite and the diffusion of carbon balance. The result is a characteristic equation of the second degree relative to the thickness of the perlite $\Delta = S_0/2$:

$$(\alpha_1 + \alpha_2)q\gamma D_x/\Delta^2 = \alpha\,(T - T_c) - C\gamma dT/dt\,. \qquad (3)$$

From equation (4) imply an expression characterizing inter-plates distance of pearlite in non-equilibrium $\gamma \rightarrow \alpha + c$ – transformation:

$$S_0 = 2\sqrt{[(\alpha_1 + \alpha_2)q\gamma D_x]/(\alpha(T - T_c) - C\gamma dT/dt)}\,, \qquad (4)$$

where $\Delta T = T - T_c$ - is temperature difference between sample and environment;

dT/dt is the cooling rate of the sample;

α – heat transfer coefficient;

q – the specific amount of heat released during the formation of perlite;

γ – the density of iron-carbon steel;

α_1 and α_2 – concentration coefficients.

If the transformation of austenite takes place in isothermal conditions, it can be assumed that dT/dt = 0. In this case, equation (3) takes the following simple form:

$$S_0 = 2\sqrt{[(\alpha_1 + \alpha_2)q\gamma D_x]/(\alpha\Delta T)}. \qquad (5)$$

From equation (5) it follows that inter-plates distance depends on the diffusion coefficient of carbon along the X-axis, hypothermia alloy ΔT and the concentration coefficients α_1 and α_2.

Themselves concentration coefficients are also dependent on the subcooling ΔT. When $\Delta T = 0$, $\alpha_1 + \alpha_2 = 0$. If you increase the subcooling of the concentration ratios increase. The maximum value of the coefficients $\alpha_1 = 1$ and $\alpha_2 = 1$.

At small ΔT one can write approximately:

$$\alpha_1 + \alpha_2 = \alpha'\Delta T, \qquad (6)$$

where α' is some constant value.

Then at low subcooling of the alloy ΔT:

$$S_0 = \sqrt{\alpha' q\gamma D_x/\alpha}. \qquad (7)$$

At deep subcooling $\alpha_1 + \alpha_2 \sim 2$ и $S_0 \sim \sqrt{D_x/\Delta T}$.

The final calculated expression for inter-plates distances has the form: when $\Delta T > \Delta T_0$,

$$\lg S_0 = K_1 - 0{,}5 \lg \Delta T - 0{,}4343Q/2RT;$$

if $\Delta T \le \Delta T_0$,

$$\lg S_0 = K_2 - 0{,}4343Q/2RT, \quad (8)$$

where K_1 and K_2 – are some constants ($K_2 = K_1 - 0{,}5 \lg \Delta T_0$);

ΔT_0 – the point "sewing" of equations.

In this paper, we obtain the following expression for the growth rate of pearlite:

$$v = \sqrt{\alpha(\alpha_1 + \alpha_2)\Delta T D_z / q\gamma} \ . \quad (9)$$

After substitution of the expressions for the diffusion coefficient as a function of temperature, the temperature dependence for the rate of growth of pearlite was found in the form:

$$v = \Delta T \sqrt{\alpha\alpha' A \exp(-Q / R(T_e - \Delta T)) / q\gamma}, \quad (10)$$

where it is considered that the diffusion of carbon occurs in isothermal conditions at a temperature $T_e - \Delta T$ [here T_e = 996 K – the equilibrium temperature of the eutectoid transformation, R = 8,314 J/(mol·K)].

According to the authors built the model, the growth rate of pearlite in the direction of the axis X has a maximum value when the subcooling ΔT = 149,3 ° C, if we assume that the diffusion of carbon occurs in the ferrite. In the Z axis direction, the growth rate of pearlite is theoretically maximum value when the subcooling ΔT = 99,6 ° C, if we consider the diffusion in austenite. Note that the maximum on the experimental dependence of the growth rate of pearlite with a greater degree of accuracy is described by the diffusion of carbon in ferrite than in austenite, which corresponds to the Onsager's conjecture [19]. The calculated dependence of $S_0 \sim \sqrt{D_x / \Delta T}$ coincides with sufficient accuracy with the experimental values of inter-plates distance of perlite.

The comparison of experimental data with results of calculations, however, demonstrates that different authors proposed methods of calculating the growth rate of pearlite colonies require consideration of additional factors [2, 4, 13, 14]. B. Lyubov as such an additional factor used, concentration of stresses occurring in front of the pearlitic transformation [2]. Taking into account the influence of the concentration of stresses significantly increases the calculated value of the speed of lateral growth of pearlite colonies and brings it closer to the experimental value for highly pure of eutectoid steel [2] (Fig.2).

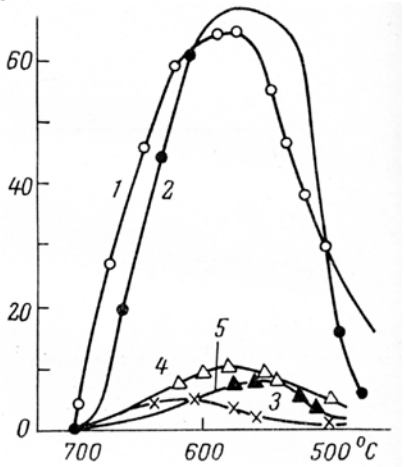


Fig. 2. *The speed of lateral growth of pearlite:*
1 - the estimated data B. Lyubov [2];
2 - experimental data for high purity eutectoid steel;
3 - data calculated by the formula Zener (2);
4 - data calculated by formula (10);
5 - experimental data for industrial steel.

Theory eutectoid transformation continues to evolve recently, see eg. [13-16], however, the pearlite transformation from the basis of nonequilibrium thermodynamics is still not addressed. Consequently, matters of non-equilibrium thermodynamic descriptions of the eutectoid transformation of austenite. The aim of this work is the development of diffusional model eutectoid transformation of austenite on the basis of the positions of nonequilibrium thermodynamics with the finding of the dependence of main kinetic parameters of the process – the rate of growth of pearlite and inter-plates distance – on the magnitude of supercooling of steel for the stationary process.

3. The equations of motion and basic ratios

Nonequilibrium thermodynamics provides the necessary apparatus for the analysis of diffusion processes in iron-carbon alloys [17-19]. In the general case, the thermodynamic equations of motion have the form [18]:

$$J_i = \sum_{\kappa=1}^{N} L_{ik} X_k \ (\text{i=1,..,N}), \quad (11)$$

where Ji – streams, Xk is the thermodynamic force; Lik = Lki – Onsager's kinetic coefficients [19]; i,k – the numbers of charges (substrate transfer).

The main driving forces of phase transitions in nonequilibrium thermodynamics are the gradients of the chemical potentials of the components [17-19]. When considering discontinuous systems as thermodynamic forces are being utilized finite differences of the chemical potentials ($-\Delta\mu_i$,), during the transition from metastable state to stable [20-23]. If, for example, as charges process carbids education to use two quantities, the concentration of carbon and iron, according to (11), the equations of motion take the form:

$$J_1 = L_{11}X_1 + L_{12}X_2 \quad (12.1)$$

$$J_2 = L_{21}X_1 + L_{22}X_2, \quad (12.2)$$

where J_1 is the carbon flux characterizing the rate of formation of carbides; J_2 – flow iron;

$X_1 = (-\Delta\mu_{Fe})$, $X_2 = (-\Delta\mu_C)$ – – thermodynamic forces of the iron and carbon. The difference of potential has the sign "+" in its increase, and the flow is directed in the direction of decreasing potential, so the expression for the forces contain a " – " character.

In the present work the generalization of the equations characterizing the growth of pearlite colonies based on the application of methods of non-equilibrium thermodynamics.

To do this, equation (12) from the work of the authors [12], characterizing the growth rate of pearlite colonies present in the form of:

$$dX/dt = D_x[(C'_ф - C'_ц)/(C'_ф - C_ф) + (C'_ф - C'_ц)/(C_ц - C'_ц)]/\Delta = (D_x/\Delta)(-\Delta\varphi), \quad (13)$$

where D_x is the diffusion coefficient of carbon in austenite along the x axis at a predetermined temperature T;

Δ - the thickness of a layer of austenite have different carbon concentration;

$C'_ф$ и $C'_ц$ – and the concentration of carbon in ferrite and austenite near cementite plates, respectively, at temperature T (Fig.3);

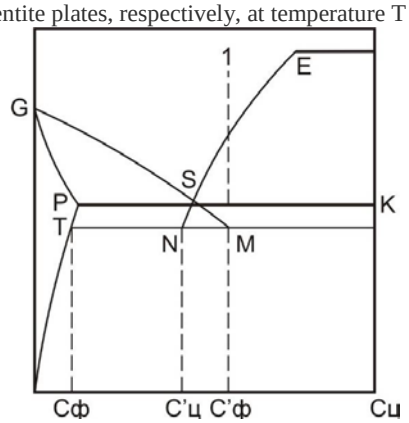


Fig. 3. *Diagram of the eutectoid transformation of steel composition 1.*

$C_ц$ – content of carbon in cementite (~6,67 %);

$C_ф$ - the amount of carbon in the ferrite at a given temperature T;

-Δφ is the thermodynamic force of the lateral growth of pearlite. It is determined by the concentrations of carbon in ferrite and cementite and has a dimensionless size.

The second equation, characterized our system, the balance equation of heat (16) from [12] we written in the form:

$$C\gamma dT/dt = \alpha \Delta T - (q\gamma/\Delta)\, dX/dt, \qquad (14)$$

where α is the transfer coefficient;

ΔT – temperature difference of the sample (T) and the cooling medium;

q – the specific amount of heat released during the formation of perlite; γ – the density of steel.

If the charge process eutectoid pre-rotation of the austenite to use two variables – the temperature of the sample T and the thickness of the plates of perlite X, then, according to (3), Onsager's equations of motion should have the symmetric form (3), where

$J_1 = -\, dX/dt$ is the flow value of the perlite layer (increasing the absolute values of the thermodynamic forces of growth of pearlite stream increases in absolute value);

$J_2 = -\, C\gamma dT/dt$ is the heat flow in the sample (by reducing the temperature of the sample flow positive);

$X_1 = (-\Delta\varphi)$, $X_2 = (-\Delta T/T)$ – thermodynamic forces of growth of pearlite and temperature [24].

In order for equation (13) correspond to equations (12.1), it must contain the additional term $L_{12}(-\Delta T/T)$; the value of the coefficient $L_{11} = (D_x/\Delta)$:

$$J_1 = (D_x/\Delta)(-\Delta\varphi) + L_{12}(-\Delta T/T), \qquad (15.1)$$

where L_{12} is the cross - ratio, whose value is still unknown.

Thus we introduce the (perceived) service dependence of growth rate the pearlite layer not only on the concentrations of carbon in phases, and temperature.

By substituting the expression (51) in energy equation (5), find an expression for the flow of heat J_2:

$$J_2 = (q\gamma/\Delta)((D_x/\Delta)(-\Delta\varphi) + L_{12}(-\Delta T/T)) - \alpha T(-\Delta T/T) =$$
$$(q\gamma D_x/\Delta^2)(-\Delta\varphi) + (q\gamma L_{12}/\Delta - \alpha T)(-\Delta T/T). \qquad (15.2)$$

Comparing between equations (12.2) and (15.2), we get:

$$L_{21} = q\gamma D_x/\Delta^2. \qquad (16)$$

Using the kinetic coefficients of the relations, the Onsager's cross-links Lik = Lki [19], we find, that

$$L_{12} = L_{21} = q\gamma D_x/\Delta^2; \qquad (17)$$

whereas $L_{22} = q^2\gamma^2 D_x/\Delta^3 - \alpha T$. (18)

The system of equations (6) takes the form:

$$J_1 = (D_x/\Delta)(-\Delta\varphi) + q\gamma D_x/\Delta^2(-\Delta T/T) \qquad (19.1)$$

$$J_2 = (q\gamma D_x/\Delta^2)(-\Delta\varphi) + (q^2\gamma^2 D_x/\Delta^3 - \alpha T)(-\Delta T/T). \qquad (19.2)$$

In accordance with (19.1) on the growth rate of pearlite affects not only the thermodynamic power concentration, but the temperature gradient of the sample and the environment.

We next consider the phase transformation of austenite in the special conditions of stationary growth of pearlite colonies when you can accept that ΔT ≈ const, $dT/dt \approx 0$. In this case, equation (19.2) becomes:

$$J_2 = (q\gamma D_x/\Delta^2)(-\Delta\varphi) + (q^2\gamma^2 D_x/\Delta^3 - \alpha T)(-\Delta T/T) = 0. \qquad (20)$$

At small ΔT one can write approximately, as it was done in [12]:

$$\Delta\varphi = \kappa\Delta T/T, \qquad (21)$$

where K – coefficient of proportionality.

By analogy with the previously obtained solutions [25], we introduce the following notation:

$$\Delta_0 = \sqrt{\kappa q\gamma D_x/\alpha T}; \qquad (22)$$

$$\Delta_l = q\gamma/k, \qquad (23)$$

is a characteristic parameter of the system.

Equation (20) can now be represented as:

$$\Delta^3 - \Delta_0^2\Delta - \Delta_0^2\Delta_l = 0. \qquad (24)$$

When Δl=0, as might be expected, the solution of equation (24) $\Delta = \Delta_0$.

We receive known solution for pearlitic transformation of austenite [12].

If $\Delta l \neq 0$, we must find the roots of equations of 3rd degree.

For solutions of equation (15) we introduce the normalization $\Delta_0 = 1$.

Equation (24) then takes the form:

$$\Delta^3 - \Delta - \Delta_l = 0. \qquad (25)$$

The roots of the equation (16) is equal to [25]:

$X_0 = A+B$, $X1,2 = -(A+B)/2 \pm i\sqrt{3}(A-B)/2$

$$A = \sqrt[3]{\Delta_l/2 + \sqrt{Q}}, \quad B = \sqrt[3]{\Delta_l/2 - \sqrt{Q}},$$

where A and B are any values of the cube roots of complex numbers, satisfying the equality $AB = -P/3$; $Q = \Delta_l^2/4 - 1/27$.

If Q>0, then the solution of equation (25) are valid and two complex roots. In our case, in the valid region, there is one root of the equation (25).

To a solution of the equation of state (16) was negled, it can be represented graphically. We introduce two auxiliary functions $У_1$ и $У_2$, where: $У_1 = X^2$, $У_2 = 1 + \Delta l/X$.

The solution of equation (25) can be found graphically in the form of: $У_1 = У_2$. (26)

Plot the graphs of functions $У_1$ and $У_2$on the coordinate axis with different values of Δl (in units of Δ_0) (Fig.4).

Thus, in accordance with expressions (22) and (23), we take into account that Δ_l = const and Δ_0 is changed depending on the temperature of the transformations of austenite.

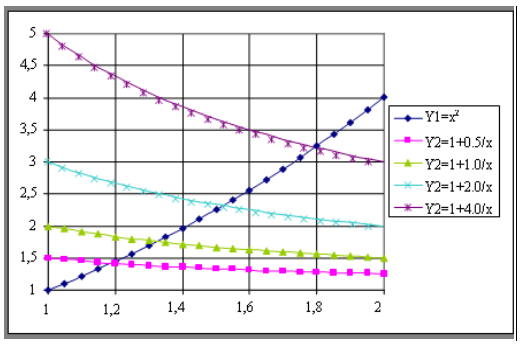


Fig. 4. *Graphical solution of the equation of state (26).*

As can be seen from figure 2, in the valid region sous-exists one solution of equation (3.39). For small Δ_l (<0,5) root Xk is in a region close to 1 ($Xk \to \Delta_0$), at the increase Δ_l (in units of Δ_0) the value of the root increases. . For large values Δ_l is the root *Xk* is approximately equal to

$$Xk \approx \sqrt[3]{\Delta l/\Delta_0}. \qquad (27)$$

Inter-plates distance of perlite at stationary growth process, we find by the formula:

$$S_0 = 2X\kappa \times \Delta_0 = 2\kappa Xk\sqrt{\Delta l D_x/\alpha T}. \qquad (28)$$

Using equations (19.1) and (27) – (28), we find also a refined expression for the rate of growth of pearlite in an isothermal transformation:

$$dX/dt = \frac{kDx}{S_0}\frac{\Delta T}{T}\left(1 + \frac{2\Delta l}{S_0}\right) \qquad (29)$$

Formula (29) is a more accurate expression for determining the rate of growth of pearlite in eutectoid transformation than previously obtained by the authors, the expression (12) in the article [12].

4. DISCUSSION OF RESULTS

Use the known dependence of the diffusion coefficient on temperature [27]:

$$D = A\exp(-Q/RT), \qquad (30)$$

where Q is the activation energy (Q ≈ 134 kJ/mol);

R is constant (R = 8,314 J/(mol·K)).

After substituting known values for the parameters of steel and given that k≈2,0, we find the calculated dependence of the growth rate of pearlite on the magnitude of subcooling of the alloy (Fig. 5). This figure shows for comparison the dependence of the growth rate of pearlite from the size of subcooling, calculated by the formula Zener (1) [4, 5].

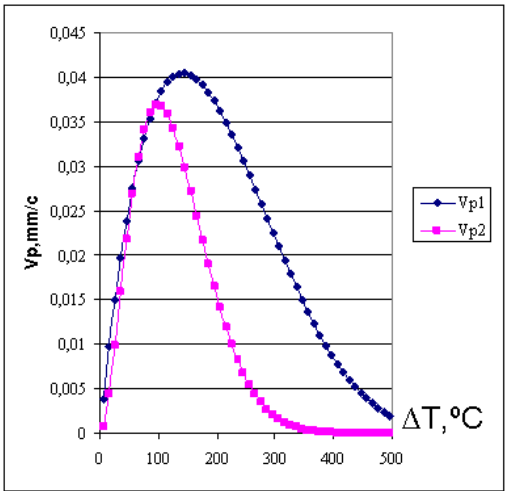


Fig. 5. *The dependence of the growth rate of pearlite from the size of subcooling, calculated by the formula (29) present work (Vp1) and Zener formula (2) [4, 5] (Vp2).*

Consider the change in the growth rate of pearlite (20) if we change the value of the overcooling of the alloy. When $\Delta T = 0$, as it should be, $dX/dt = 0$. If you increase the subcooling, the rate of formation of pearlite increases, passing through a maximum at a certain value of ΔT.

According to the constructed model, the growth rate of pearlite in the direction of the axis X has a maximum value when the supercooling $\Delta T = 140{,}0$ ºC. Calculated according to the formula breakdown, the growth rate of pearlite is theoretically maximum value when the subcooling $\Delta T = 96$ ° C. Therefore, the theoretical expression (29) allows a more accurate way to describe max and the course of the experimental curve for the rate of formation of pearlite, presented in the works [2, 15] for high purity eutectoid steel.

Obtained in this section an expression for the growth rate of the perlite has considerable value when supercooling 300...400 °C, thereby determining the possibility of formation of pearlite in the temperature range. Indeed, in [15] revealed the formation of pearlite in carbon steels in the temperature range 375...325 °C. The calculated dependence inter-plates distance of perlite according to the formula (28) from the size of subcooling of steel is shown in Fig. 6. The same figure shows the experimental points from [15].

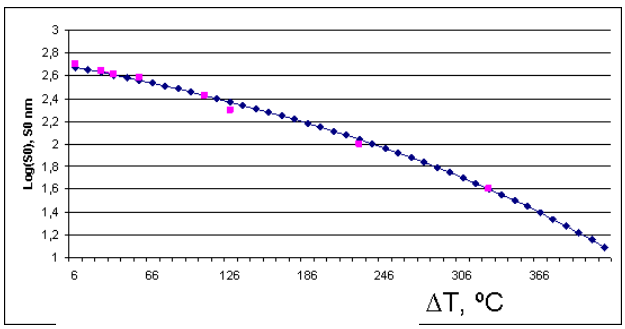


Fig. 6. *The calculated dependence of inter-plates distance of perlite from the size of subcooling of steel (■ – experimental points from [15], p. 122).*

There is quite good agreement of the calculated dependence with the results of recent experiments, indicating the adequacy of the proposed model.

INSIGHTS

1. Application of methods of nonequilibrium thermodynamics to the analysis of the eutectoid transformation of austenite have helped to clarify previously obtained by the authors of the equation of motion of the system and find new, more accurate theoretical expression for the rate of growth of pearlite and inter-plates distance.

2. The theoretical expression for the rate of growth of pearlite, obtained in the present work, allows to more accurately describe the high and the pilot of the curve for the rate of growth of pearlite, presented in the works [2, 15] for high purity eutectoid steel.

3. The obtained dependence for inter-plates distance distances of perlite on the magnitude of subcooling become sufficiently relevant experimental results of work [15] for carbon steel.

REFERENCES

1. G.V. Kurdyumov, L.M. Utevskij, R.I. Enntin, Prevrashcheniya v zheleze i stali (M.: Nauka: 1977).

2. B.YA. Lyubov, Kineticheskaya teoriya fazovyh prevrashchenij (M.: Metallurgiya: 1969).

3. S.V. Bobyr, V.I. Bol'shakov, Uspekhi fiziki metallov, T.15:123(2014).

4. R.F. Mejl, U.K. Hagel', Uspekhi fiziki metallov. T. III. (M: GosNTI: 1960).

5. C. Zener. Trans. AIME, V.167(1946).

6. M. Hillert. Jerncontorets Ann. V.141 (1957).

7. I.L. Mirkin, Trudy Moskovskogo instituta stali, sb.HVIII (M.: MISiS: 1941).

8. L. Onsager. Phase Transformation in Solid. Conference (Cornwell: N.Y.C.: 1951).

9. D. Turnball. Acta Met. V.3:43(1955).

10. J.W. Cahn. Acta Met. V.7:20(1959).

11. S.V. Bobyr. Stroitel'stvo, materialovedenie i mashinostroenie: Sb. nauch. tr. Vyp.22, ch.2: 60(2003).

12. V.I. Bol'shakov, S. V. Bobyr, MiTOM, №8: (2004).

13. V.M. Schastlivcev, D.A. Mirzaev, I.L. YAkovleva. Struktura termicheski obrabotannoj stali. (M.: Metallurgiya: 1994).

14. V. E. Ol'shaneckij. MiTOM, №3:3(2003).

15. V.M. Schastlivcev, D.A. Mirzaev, I.L. YAkovleva i dr. Perlit v uglerodistyh stalyah. (Ekaterinburg: UrO RAN. 2006).

16. YU.I. Kononenko, V. E. Ol'shaneckij. Novi materiali i tekhnologiï v metalurgiï ta mashinobuduvanni, № 1:37(2010).

17. I. Prigozhin, Vvedenie v termodinamiku neobratimyh processov (Moskva: IL:1960).

18. S. de Groot, P. Mazur. Neravnovesnaya termodinamika (Moskva: Mir, 1964).

19. L. Onsager. Phys. Rev., 37: 405 (1931).

20. A.A. ZHukov, R.L. Snezhnoj, Diffuzionnye processy v metallah (Kiev: Naukova dumka: 1966).

21. M.A. Krishtal, A.A. ZHukov, R.L. Snezhnoj, EH.G. Titenskij, Termodinamika, fizicheskaya kinetika strukturoobrazovaniya i svojstva chuguna i stali. Vyp.4. (Moskva: Metallurgiya: 1971).

22. S.V. Bobyr, Metallofiz. novejshie tekhnol., 35, №2:199 (2013).

23. S.V. Bobyr, Metallofiz. novejshie tekhnol., 36, №10:1385 (2014).

24. B.S. Bokshtejn, Diffuziya v metallah (Moskva: Metallurgiya:1978).

25. S.V. Bobyr, V.I. Bol'shakov. Novi materiali i tekhnologiï v metalurgiï ta mashinobuduvanni, №1:21 (2012).

26. G.Korn, T. Korn. Spravochnik po matematike dlya nauchnyh sotrudnikov i inzhenerov. (M.: Nauka,1974).

27. L.N. Larikov, V.I. Isajchev, Diffuziya v metallah i splavah. Spravochnik. (Kiev: Naukova dumka: 1987).

FORMATION OF COMPOSITE STRUCTURES BASED ON TETRAGONAL ZIRCONIA DOPED BY D-ELEMENTS OF I GROUP

Ass. Prof. Dr. Gorban O.[1], M.Sc. Kharchenko M.[1], M.Sc. Bryukhanova I.I., Ass. Prof. Dr Gorban S.[1], M.Sc. E. Sinelnikova[2]

Donetsk institute for physics and engineering named after O.O. Galkin NAS of Ukraine, Ukraine[1]
Municipal educational institution the Gymnasium №4, Russia[2]

oxanag1@ukr.net

Abstract: *The investigation of influence of modified conditions on formation of complex materials based on tetragonal zirconia doped by d-elements of I group (Cu or Ag) was carried out, in particular the routes of synthesis and type of dopant. The kinetic parameters of separated stage of NPs formation (drying of hydrogel under MW irradiation, dehydration and crystallization of amorphous zirconia NPs) were estimated. It was shown, the dehydration of tetragonal zirconia hydrogel in conditions of MW irradiation occurs due in two stage. In contrast for Cu (or Ag) –modified hydrogels only one stage dehydration is observed. The dehydration and crystallization of unmodified and modified xerogel is studied by DSC method. It was shown that the kinetic parameters of dehydration depend as from nature of zirconium salts that were using for synthesis and type of dopant. For crystallization processes the some parameters (crystallization temperature, enthalpy) are saved features of dependence on route of synthesis for unmodified and modified systems. However, the behaviour of dependence of activation energy on route of synthesis is contrast for unmodified and modified systems.*

Keywords: COMPOSITE NANOPARTICLES, DSC, DEHYDRATION, CRYSTALLIZATION

1. Introduction

Complex oxide systems based on zirconia are promising materials in modern material science [1]. Reasons for using of d-elements of I group (Cu, Ag, Au) or their oxides at technology of creation of functional composite oxide structure are next:

-the first these metals and their oxides have bactericide and fungicide properties,

-the second they have some electrical and optical properties,

-the third they can be used as catalysts and

-the fourth they can be used at creation ceramic materials with higher tribological properties [2-3].

Some routes of creation of functional structures are used in material science technology. In practice, the impregnation of Ag or Cu salts in oxide surface is a more often used method for creation or enhance catalytic systems [4]. However, introducing of Cu or Ag-contained compounds into the oxide synthesis process results in a greater variation of catalytic system properties because, in this case, the added ions influence not only the surface state but also the crystal lattice of the oxide [5].

However, the using of second route of synthesis for creation of composite structure based on tetragonal zirconia doped by d-elements of I group (especially, Cu and Ag) has determined features. The use of ammonium hydrate as agent-precipitator leads to form Cu (or Ag) ammonium hydroxocomplexes that occlude on surface of colloidal zirconia hydroxide nanoparticles (NPs) [6]. There are the ammonium complexes of copper - $[Cu(NH_3)_m(H_2O)_n]^{2+}$ or hydroxocomplexes - $[Cu(H_2O)_m(OH)_k]^{2-k}$, where coordination number of coper is 4 or 6 and k<3, or mixing ammonium hydroxocomplexes - $[Cu(NH_3)_m(OH)_k]^{2-k}$. For case of silver complexes in which coordination number of silver ions is 2 the structure of complexes may be described as $[Ag(NH_3)_2]X$, where X is chloride ion or nitrate ion. Ammonium molecule in first coordination sphere may be exchange on water molecule in water solution. The structures of copper or silver complexes depend on synthesis conditions, in particular, pH precipitation. For example, at high pH the formation of ammonium complexes of copper or silver are observed, such as the decreasing of pH value of solution leads to exchange of ammonium ligand on hydroxyl group. Since zirconia hydrogel is colloid systems the absorption of copper or silver complexes on zirconia NPs surface may influence on formation of modified NPs systems and their properties.

The nature of zirconium salts may change the optimal concentration and viscosity of solution. It also is very important moment in technology of obtaining of complex oxide systems because it may influence on distribution the dopants between phases and leads to form inhomogeneity product [7]. Other main moments of wet technology of complex oxide materials are influence of type of dopant, salt nature and salt concentration on emulsion stability, aggregation and electrophoretic movement of NPs, features of formation precipitates [8-10], phase stability of NPs, other. In this connection, in technologies of obtaining of complex oxide materials investigators do accent the influence of these factors on drying of zirconia hydrogel, dehydration and crystallization amorphous zirconia xerogel, growth of oxide NPs.

The aim of present work is investigation of formation of complex oxide systems based on tetragonal zirconia doped d-elements of I group.

2. Preconditions and means for resolving problems

2.1 Synthesis and characterization of zirconia metastable NPs

Fig. 1 shows the scheme of syntheses of tetragonal zirconia doped by copper or silver dopant. Synthesis contains some stages there are zirconia hydrogel precipitation; formation of amorphous zirconium hydroxide (xerogel) under MW drying; formation of composite structure based on tetragonal zirconia under heat treatment.

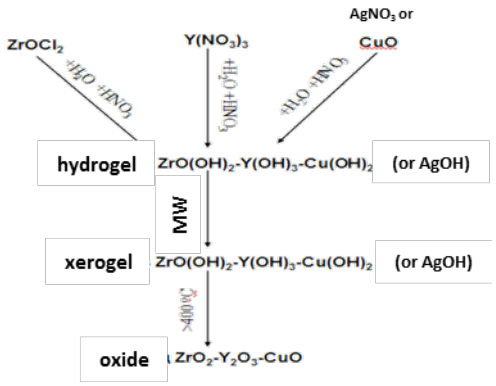


Fig. 1 *- Scheme of syntheses of tetragonal zirconia doped by copper or silver dopant.*

Dehydration kinetics of zirconia hydrogel and xerogel are described in Avrami-Erofeev approach:

$$d\alpha / dt = k \cdot f(\alpha) \quad (1)$$

where α is the share conversion of phase fraction, t – dehydration time (min), $f(\alpha)$ - function which depends on dehydration or crystallization mechanism and NPs geometry [11]. Equation (1) after integration is:

$$g(\alpha) = \int d\alpha / f(\alpha) = k \cdot dt = kt \quad (2)$$

where $g(\alpha)$ is function which depends on dehydration or crystallization mechanism such as f(α). The types of $g(\alpha)$ are shown in work [11].

Accordingly [11], type of function which describes dehydration kinetic depends on partial pressure of water under NPs surface. The constant removing of water vapor is characteristic for MWconditions of drying of zirconia hydrogel, because $g(\alpha)$ corresponds to Avrami-Erofeev equation $[-\ln(1-\alpha)]^{1/n}$, where n=0.5;1; 2; 2,5; 3;…, and equation (2) transform to (3):

$$[-\ln(1-\alpha)]^{1/n} = kt \quad (3)$$

Avrami constant *n* shows mechanism of process (dehydration and crystallization), and lnK corresponds to velocity of evaporation or crystallization.

Activation energies of dehydration and crystallization are estimated in Kissindger approach (4):

$$d\ln(\beta / T^2_{\max}) / d(1/T_{\max}) = -E_{act} / R \quad (4)$$

where T_{max} – temperature of maximum of endothermic or exothermic peaks, K, β is heat increasing rate.

3 Kinetic parameters of formation of xerogels and processes of their dehydration and crystallization

3.1 Kinetic parameters of drying of hydrogel under MW condition

Analysis TG data in logarithmic coordinates of equation (3) allows to estimate parameters of dehydration there are m which describes reaction mechanism (in particular, if m<1 the evaporation occurs according to homogenous mechanism, if m changes from 1 to 2 the evaporation occurs with line portion of surface, for example from pores) and lnK corresponds to rate of evaporation.

It is noted, that dehydration process is sum of water diffusion processes on surface and inside pores of hydrogel NPs, water phase transformation (liquid-vapor), water desorption from NPs surface and other. For example, dehydration process of Cu doped tetragonal zirconia hydrogel approximately may be determined as:

$$ZrO(OH)_2 \cdot Y(OH)_3[Cu(NH_3)_m(OH)_k]^{2-k} nH_2O \rightarrow ZrO(OH)_2 \cdot Y(OH)_3[Cu(NH_3)m(OH)_k]^{2-k} + nH_2O, \quad (5)$$

For Ag doped zirconia process of dehydration is analogical. The amount of residual ammonium, nitrate or chloride ions depends on precursor type and may be variated by washing number. Thus, the process which occurs at dehydration may be complex because the dehydration determines by water desorption from pores surface and water diffusion from pores to NPs surface.

Parameters of kinetic dehydration of unmodified and Cu (or Ag) modified zirconia hydrogel which syntheses from zirconium nitrate and chloride salts were shown in table 1.

Table 1 *– Kinetic parameters of unmodified (ZrO_2-3 mol. % Y_2O_3) and Cu (or Ag) modified amorphous xerogel formation (ZrO_2-3 mol. % Y_2O_3- 1 mol. % CuO(or Ag_2O))*

	ZrO(OH)2-3 mol.%Y(OH)3-x mol. % Me-complex		
		Me - CuO	Ag2O
	0	1	1
	Nitrate route		
lnk1	-4.62	-2.86	-2.33
n1	1.99	2.01	2.5
lnk2	-2.32		-
n2	0.81		-
	Chloride route		
lnk1	-4.8	-2.14	-2.49
n1	1.90	2.04	2.6
lnk2	-2.61		-
n2	0.82		-

It was shown that the dehydration of unmodified zirconia xerogel contains two stages, the kinetic parameters of that depend on precursor nature. The n_1 values for systems is near 2 for both routes of synthesis of zirconia hydrogel. It is evidence that the evaporation occurs with line portion of surface and the nature of used zirconia salt does not practically influence on intensity of water evaporation. The n_2 values m is less than 1 for both routes of synthesis of zirconia hydrogel. The change of n values at transfer from first to second stage may be connected with activation of diffusion processes on second stage. Kinetic of second stage may be described by homogenous mechanism of evaporation and intensity of this stage in two time bigger than evaporation water on first stage.

For cause of Cu (or Ag) modified zirconia hydrogel the dehydration occurs on the one stage. The n is approximately equal 2 and the mechanism of dehydration of zirconia hydrogel does not change at their modification by Cu ions. For Ag-modified systems n is above 2. The intensity of evaporation for both type of dopants is bigger to compare with intensity of unmodified systems and does not depend from type of dopants that use for creation of complex system.

Thus, mechanism evaporation for first stage is equal for unmodified and Cu (or Ag) modified tetragonal zirconia but the modification of tetragonal zirconia by d-elements of I group lead to disappearance the second stage of evaporation. The rate of dehydration process is more intensive for case modified systems at approximately equal time of drying. The estimated kinetic parameters show the independence of dehydration of modified zirconia hydrogel on nature of synthesis route and type of dopant.

3.2 ***Kinetic parameters of dehydration of xerogel***

Fig.2 shows the DSC curves for unmodified and Cu (or Ag) modified tetragonal zirconia.

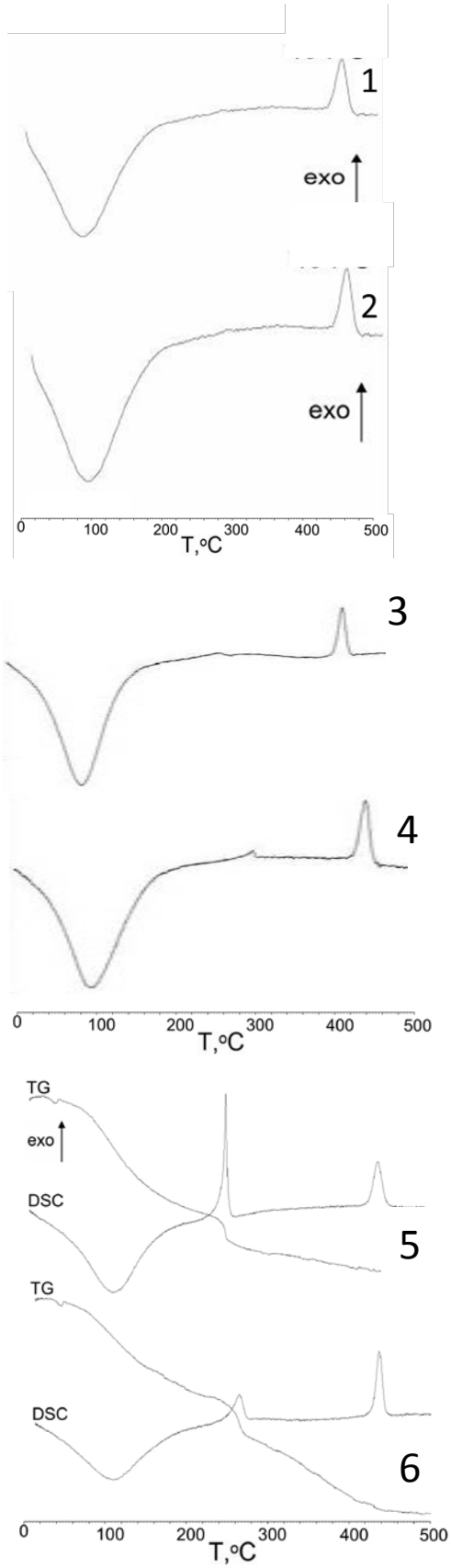


Fig.2 *DSC curves for nitrate route: 1) unmodified 3) Cu and 5) Ag modified tetragonal zirconia and for chloride route: 4) unmodified 3) Cu and 6) Ag modified tetragonal zirconia.*

Accordingly DSC data at calcination of unmodified system are observed the wide endothermic peak (temperature diapason is 20-250^{o}C) and the narrow exothermic peak at temperature above 400^{o}C. For case of Cu(Ag)-modified systems DSC specters shows the wide endothermic peak (temperature range is 20-250^{o}C) and two exothermic peaks. First exothermic peak is appearance at near 300^{o}C and their intensity depends on precursor nature. This peak corresponds to processes that occur at destroyed or structure reorganization of Cu (or Ag) complexes. Second exothermic peak correspond to crystallization of tetragonal zirconia. Kinetic parameters of dehydrationof xerogel are presented in table 2.

Table 2 *- Kinetic parameters of dehydration of xerogel*

Systems	Parameters	
	T, ^{o}C	ΔH, J/g
Chloride route		
ZrO_2-$3Y_2O_3$	383,2	-449,44
ZrO_2-$3Y_2O_3$-1CuO	378,8	-544,04
ZrO_2-$3Y_2O_3$-1Ag_2O	393,1	-454.51
Nitrate route		
ZrO_2-$3Y_2O_3$	379	-565.81
ZrO_2-$3Y_2O_3$-1CuO	382.9	-779.04
ZrO_2-$3Y_2O_3$-1Ag_2O	401.9	-519.7

It is noted, that for unmodified systems the temperatures of dehydration is decreasing for material, which was synthesized by nitrate route. However, the enthalpy of this process are increasing for this route. It connects with the adding of energy expensive at remove residual nitrate groups to dehydration of xerogel.

For Cu (or Ag) modified systems the shift of maximum of temperature of dehydration to higher temperature are observed and the increasing of enthalpy are occurred. It is noted, for Cu modified systems the route of synthesis influences on parameters of dehydration and as for unmodified systems.

The estimated of activation energies according to equation (4) for dehydration process are presented in table 3.

Table 3 *Activation energy of dehydration for unmodified and Cu(or Ag) modified system.*

Route of synthesis	ZrO(OH)2-3 mol.%Y(OH)3-x mol. % M-complex		
		CuO, %	Ag_2O, %
	0	1	1
	Activation energy, kJ/mol		
Nitrate	22.1	29.56	40.32
Chloride	37.2	25.06	19.71

Analysis of activation energy show that adding of d-elements of I group leads to decrease of activation energy values. It may be connected with change of structure of hydrate shell of modified NPs.

First exothermic peak is appearance at 257^{o}C (for Cu-modified systems, ΔH=103 J/g) and 253^{o}C (for Ag-modified systems, ΔH=105 J/g) for systems that are synthesized by

nitrate route and at 263°C (for Cu-modified systems, ΔH=76 J/g) and 263°C (for Ag-modified systems, ΔH=55 J/g) for systems that are synthesized by chloride route. The difference in enthalpy of this process for systems which are synthesized by different routes may be connected with features of Cu (or Ag) complex structures, in particular, with different ligands.

3.3 *Kinetic parameters of crystallization of xerogel*

Kinetic parameters of dehydration of xerogel are presented in table 4.

Table 4 *- Kinetic parameters of crystallization of xerogel*

Systems	Parameters	
	T, °C	ΔH, J/g
Chloride route		
ZrO_2-$3Y_2O3$	699,7	108,04
ZrO_2-$3Y_2O3$-1CuO	713,4	131,17
ZrO_2-$3Y_2O3$-1Ag_2O	715,2	107,0
Nitrate route		
ZrO_2-$3Y_2O_3$	710,9	122,81
ZrO_2-$3Y_2O3$-1CuO	728,1	165,05
ZrO_2-$3Y_2O_3$-1Ag_2O	720,4	109,4

As we can see from table 4, the crystallization temperatures are higher for systems that are synthesized by nitrate route independently from their chemical composition. It is also noted the enthalpies of systems that are synthesized by nitrate route are higher than for systems are synthesized by chloride route. Higher values of enthalpy evidence about most defectiveness of crystal lattice of tetragonal zirconia. For case of Cu-modified tetragonal zirconia the routes of preparation influence on parameters of crystallization and ordering of structures are strongly.

The estimated of activation energies according to equation (4) for crystallization process are presented in table 5.

Table 5 Activation energy of crystallization for unmodified and Cu(or Ag) modified system.

Route of synthesis	ZrO(OH)2-3 mol.%Y(OH)3-x mol. % M-complex		
		CuO, %	Ag_2O, %
	0	1	1
	Activation energy, kJ/mol		
Nitrate	348,70	243,08	233
Chloride	544,38	230,59	151

Analysis of estimated activation energies show the difference dependence of E_{akt} on route of synthesis for unmodified and modified systems. For unmodified system that is synthesized by chloride route the activation energy is approximately in two time higher than for one that are synthesized by nitrate route. In contrast, the modified systems shows dependence on as route of synthesis and type of dopant (Cu or Ag).

4 Conclusion

It was shown that surface Cu (or Ag) modification of tetragonal zirconia which are obtained by wet technology occurs due to adsorption of complex of these d-elements. It was shown the structure of complex depends on synthesis conditions (route) and nature of dopants. Based on DSC method the formation oxide NPs is investigated. It was found the appearance of addition exothermic peak in DSC spectra of modified systems. This peak connects with presence of ammonium or hydroxocomplexes on zirconia NPs surface. It was noted the type of dopants and synthesis route more influence on kinetic parameters of dehydration. It may be connection with different stability of complex with different structures at temperature less 300°C. Other side the dependence of activation energy of crystallization on route of synthesis and nature of dopants is very strongly.

Acknowledgment

The work was carried out in framework of projects NANOGUARD 2AR HORIZON 2020 and partially in framework projects N47/16-H of program NAS of Ukraine “Fundamental problem of creation of new materials and nanotechnologies”

Reference

1. Ju-Nam Yon Manufactured nanoparticles: An overview of their chemistry, interactions and potential environmental implications. Science of The Total Environment, 2008, 400, 396-414 (Yon Ju-Nam, Jamie R. Lead).

2. Díaz-Flores L.L. Formation of Ag-Cu Nanoparticles in SiO2 Films by Sol-Gel Process and their Effect on the Film Properties. Phys. Stat. Sol. C, 2007, 4 (N6), 2016–2020 (L.L. Díaz-Flores, M.G. Garníca-Romo, J. González-Hernández, J.M. Yáñez-Limón, P. Vorobiev, and Y. V. Vorobiev).

3. Mayo M. J. Surface chemistry effects on the processing and superplastic properties of nanocrystalline oxide ceramics. Nanostruct. Mater., 1999, 11(2), 271–282 (Mayo M. J., Seidensticker J. R., Hauge D. C., Carim A. H.)

4. Kundokovic Lj. Deep oxidation of methane over zirconia supported Ag catalysts. Applied Catalysis A: General, 1999, 183, 35-51 (Kundokovic Lj., Flytrani-Stephanopoulos M.).

5. Ramaswamy Veda. Structural and spectral features of nano-crystalline copper-stabilized zirconia. Catalysis Today, 2004, 97, 63–70 (Veda Ramaswamy, Mahesh Bhagwat, Darbha Srinivas, Arumugamangalam V. Ramaswamy).

6. Ануфриенко, В.Ф. Особенности ассоциирования ионов Cu(II) в концентрированных водно-аммиачных растворах азотнокислой меди по данным ЭПР. ДАН, 2011, 440 (№5), 651-654 (В.Ф Ануфриенко, Г.А.Зенковец, Р.А. Шутилов, В.Ю. Гаврилов, Н.Т. Васенин, А.А.Шубин, З.Р. Исмагилов, В.Н. Пармон).

7. Cousin P. Preparation of mixed oxides: A review. Mater. Sci. and Engineer., 1990, A130 (N 2), 119-125 (P. Cousin, R.A. Ross).

8. Carter Geoffrey A. Ammonia-induced precipitation of zirconyl chloride and zirconyl -yttrium chloride solutions under industrially relevant conditions. Powder Technology, 2009, 188, 222-228 (Geoffrey A. Carter, Mark I. Ogden, Craig E. Buckley, Clinton Maitland, Mark Paskevicius).

9. Chuah G.K. The influence of preparation conditions on the surface area of zirconia. Applied Catalysis A, 1996, 145 (1-2), 267-284 (G.K. Chuah, S. Jaenickea, S.A. Cheonga and K.S. Chana).

10. Konstantinova T. Mesoscopic phenomena in oxide nanoparticles systems: processes of growth J. Nanopart. Res. – 2011. - V.13. – P. 4015-4023 (Konstantinova, T., I. Danilenko, V. Glazunova, G. Volkova, O. Gorban)

11. *Masudo, Yoshio* The effect of the water vapor pressure on the kinetics of the thermal dehydratation of some hydrates. Examples of magnesium, manganese, cobalt, zinc, yttrium and erbium formate dihydretes. Netsu Sokutei, 1995, 22 (N4), 203-211 (Yoshio Masudo).

THERMAL EXPANSION OF CARBON MATERIAL FOR SUPERCAPACITOR ELECTRODS

Dr.Sc. T. Kompan, Dipl. Ing. N. Pukhov
Department of thermodynamics, D. I. Mendeleev Institute for Metrology, Saint-Petersburg, Russia

T.A.Kompan@vniim.ru

Abstract: *Measurements of linear thermal expansion coefficient (TEC) of a nanoporous metal carbide based carbon material were carried out. The values of linear thermal expansion coefficient in the range from 20°C to 300°C were obtained. The measured value of TEC are presented for this material for the first time.*

KEYWORDS*: TEMPERATURE, THERMAL EXPANSION COEFFICIENT, NANOPOROUS CARBON, DILATOMETER*

1. Introduction

Nanotechnological initiatives of the last two decades have emphasized global trends in science and technology that had been formulated long before their recognition as a single field. Nanotechnology is by definition a deliberate employment of devices and materials with dimensions of less than 0.1 μm (100 nm). Examples of these materials are nanostructured carbon materials with considerable surface unit area. Some of them such as activated coal have been known for hundreds of years, and others have only emerged recently.

In the present paper properties of metal carbide based nanoporous carbon (CDC – carbide derived carbon) were studied. Nanoporous carbon belongs to a group of carbon materials with complex structure, which depends on parameters of the fabrication process as well as the type of original carbide. Apart from "CDC" term "skeleton carbon" is often referred to regarding the material above in the English-language literature [1]. This type of nanoporous carbon is usually obtained in process, when original carbide powder is exposed to gaseous chlorine at high temperatures. For instance, the following reaction can be used

$$SiC + 2Cl_2 = SiCl_4 \uparrow + C \qquad (1)$$

As a result of the reaction a volatile metal chloride is formed (Si in particular case). A metal atom in the chloride composition leaves the carbide crystal lattice, while carbon stays in the solid state. Since balance of forces inside the lattice is disturbed due to metal removal, carbon forms a new type of material.

The process kinetics is limited by diffusion of chlorine gas from the surface into the inside of carbide crystal grains, hence the carbon material is formed at the surface of the grains, i.e., predominantly in the form of quasi-two-dimensional crystallites (flakes). A question regarding the number of graphite layers in such flake is not addressed in the literature. Irregularity of the original carbide grain shape as well as stochastic nature of flake formation lead to a situation that exfoliated carbon flakes form an irregular conglomerate. This conglomerate structure is often described using the term "turbostratic" [2]. Cavities between flakes act as pores that determine the further functional use of the material. It is notable that shapes of macroscopic grains (granules) of nanoporous carbon remain almost the same as for the original carbide.

However, the process of graphitization of the obtained mass takes place simultaneously with formation of nanoporous carbon. If the temperature is excessively high and process time is too long, the material undergoes an internal rearrangement. Carbon layers mostly take parallel orientation, similar to that of carbon layers in graphite. Upon that the density of the material is increased and so does its some other properties as stability. However specific surface area decreases. Therefore, a tradeoff between different processes has to be taken into account when fabricating nanoporous carbon.

The technology described above allows for fabrication of different types of nanoporous carbon with parameters presented in the Table 1 [1].

Table 1. *Pore system properties for different types of nanoporous carbon*

Original carbide	Averade density, g/cm^3	Specific pore volume, cm^3/ cm^3	Specific surface, m^2/g	Pore diameter at the maximum of the distribution curve, nm
Sic	0,91	0,67	879	0,6
Tic	0,99	0,72	663	0,6
B_4C	0,55	1,08	2200	2,0
Mo_2C	0,52	1,31	2110	2,0

It has to be noted that unit surface values in the two bottom rows of the Table 1 are approaching the theoretical limit for a unit surface value in a single-layer graphite sheet (graphen), i.e., 2600 m^2 /g. This explains high efficiency of using these materials as absorbents, porous electrodes, or catalyst carriers, alongside favoring the above noted material formation and structure model.

It has to be kept in mind that the properties of the pore system, given in the Table 1, were obtained using the BET method [1] of nitrogen absorption, where a regular spherical pore shape is assumed. It bears mentioning that a significant degree of material structure disordering makes it impossible to study the structure in details by X-ray structural methods. The use of other methods for studying the material are considerably limited for different reasons. As a result, a little study has been carried out on the properties of materials falling into that group, and developers who used the material had to rely largely on empirical approach.

In the present paper thermal expansion was studied in-compact samples of pressed nanoporous carbon. Besides new information on the material, features of the material structures were deduced from the measurements.

2. Experiment

The choice of method and sample operating conditions were important aspects of the study. There are high precision dilatometry methods that provide the accuracy within $(0.5–1)\cdot10^{-9}$ K^{-1} [3], however the required equipment set is quite complex, and thus implementation of such method for in production material control is encumbered. For that reason, a fairly simple mechanical dilatometer was employed in the present paper. [4]. Measuring unit of the dilatometer is shown in the Fig. 1. TEC measurement technique is shown in the diagram in the Fig. 2. The dilatometer exerts reasonably small pressure on the sample during measurements. Accuracy of the dilatometer will be shown to be adequate for the materials of choice.

Determination of the temperature range for the measure-

ments was one part of the study. In the first series of measurement the TEC was measured up to 500°C. It was found however, that heating above 300°C leads to irreversible changes and destruction of the material. This became evident as the material experienced significant shrinkage when heated above 300°C, as well as in the fact of the material changing its dimensions during thermal cycling.

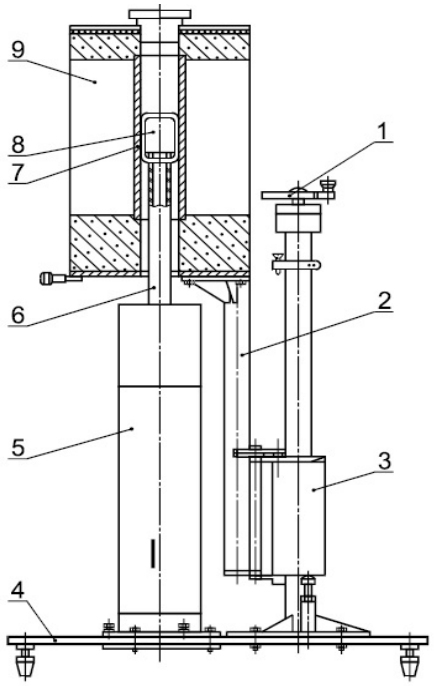


Fig. 1 *Measurement unit: 1) carriage; 2) lead screw; 3) lifting mechanism; 4) base; 5) body; 6) tube; 7) pusher; 8) specimen; 9) furnace.*

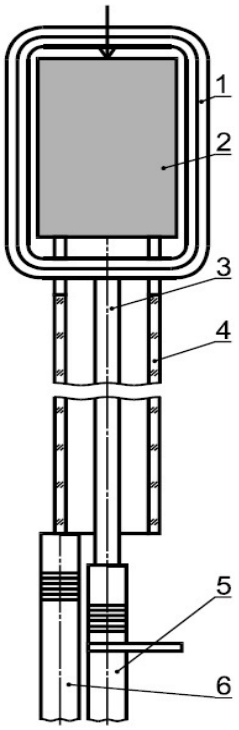


Fig 2. *TEC measurement scheme: 1) frame; 2) specimen; 3) pusher; 4) tube; 5, 6 "Micron 02" instrument displacement inductive transducers.*

Examples of such dependences are demonstrated in the Fig. 3.

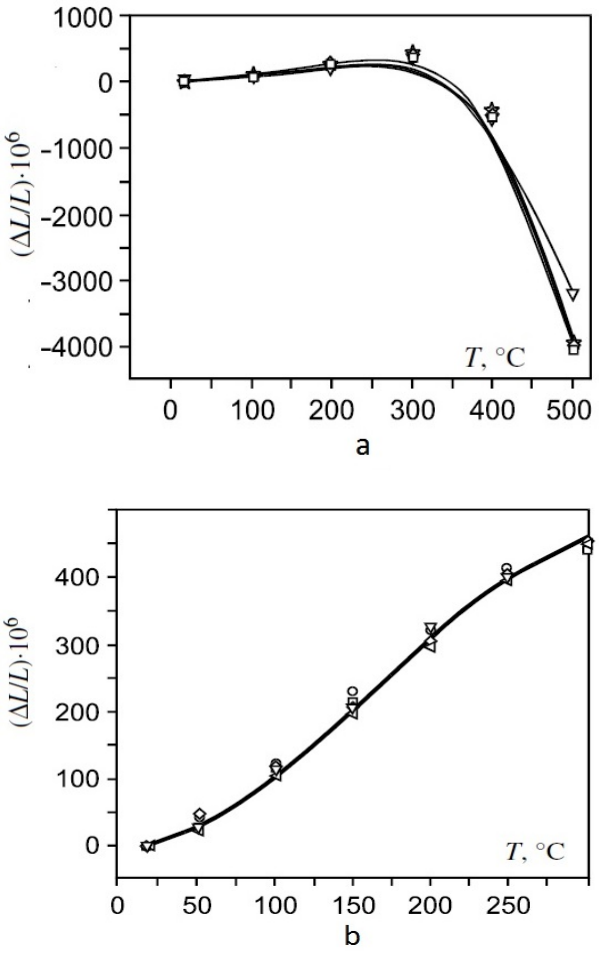


Fig. 3 *Dependence of relative nanoporous carbon elongation on temperature of 20-500 °C (a) and 20-300 °C (b)*

The dimensions were carefully checked to be stable for temperatures up to 300°C, and the results of the TEC measurements were found to be reproducible. It can be seen from the dependences given in the Fig. 4.

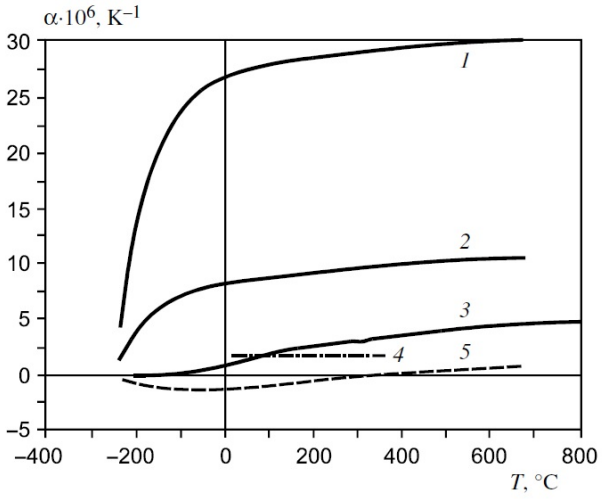


Fig. 4. *Shows the differential TEC values as a function of temperature. Also for comparing there are shown the data for expansion of carbon material with sp3-bonds (diamond) between atoms of carbon and sp2-bonds (graphite) in directions along and perpendicular to the preferred direction [5].*

Accuracy of TEC determination was evaluated based on

the curves such as one shown above or similar. The mean square deviation (MSD) for the measurements was found to be $8.6 \cdot 10^{-6}$.

3. TEC determination results and discussion

Resulting thermal expansion (elongation) values are presented in the table 2.

Table 2. *Relative elongation as a function of temperature*

Measur. number	Relative elongation $(\Delta L/L)10^6$ at temperature °C				
	100	150	200	250	300
1	144,6	228,9	330,4	-	-
2	124,6	229,6	325,4	415,4	501,0
3	121,0	207,5	326,8	-	-
4	-	205,3	306,1	405,3	458,1
5	106,0	198,2	297,6	398,2	460,2
6	112,5	200,3	-	400,4	444,5
7	115,3	215,3	-	404,7	445,9

Figure 4 shows the differential TCLE values as a function of temperature. Also for comparing there are shown the data for expansion of carbon material with sp3-bonds (diamond) between atoms of carbon and sp2-bonds (graphite) in directions along and perpendicular to the preferred direction [5].

A conglomerate of graphite-like flakes appears to be the most probable structure of nanocarbon material, hence coefficient of thermal expansion of such material can be imagined. Material with a layerwise arrangement of sp2 bonded carbon atoms has drastically anisotropic coefficient of thermal expansion. The TEC in the layer plane can be small or even negative at temperatures from –200°C to+300°C. By contrast, the TEC across layers can have large positive value. Sincein-plane bonds are much stronger compared to those between layers, thermal expansion of an individual layer (graphene) might be expected to be close to the graphite expansion along its layers.

Thermal expansion, perpendicular to an individual layer of carbon atoms (graphene) is devoid of meaning. Therefore there is neither theoretical evaluations nor experimental data for flakes comprising a small number of layers. General considerations suggest that outer layers of the flake do not have “neighbours” (and bonds)on the outside, and consequently they do not affect expansion. At the qualitative level, it may be suggested that the TCLE of a flake perpendicular to the plane of that object α would be related to the number of carbon layers N is a flake and the TCLE of the layer $\alpha\perp$ by the relationship

$$\alpha_* = \alpha_\perp (N - 1)/N.$$

Macroscopic material samples are composed of an non-oriented conglomerate of flakes. The thermal expansion coefficient of such samples should be determined in the same way as it is done for polycrystalline samples, which is in terms of $\alpha\perp$ and $\alpha\|$ expansion coefficients (expansion coefficients perpendicular to and parallel to the plane of graphite flakes respectively) using the following equation

$$\alpha = \alpha_*/3 + 2\alpha_\|/3 = \alpha_\perp (N - 1)/(3N) + 2\alpha_\|/3.$$

Calculation of the number of the graphene layers N in a carbon flake yields a value of N = 1.75 at a temperature of 300 K. That value confirmsthe current concept of the nanocarbon material structure. It can be inferred from the Fig. 4 that the resulting TEC values obtained in the paper are slightly larger than TEC of graphite along its carbon layers. This validates the nanocarbon material model as described above.

4. Conclusions

The measurements of TEC of nanoporous carbon, conducted for the first time, are described in the present paper. Temperature stability range was determined for the material. Obtained TCLE values are situated between the TCLE values of anisotropic graphite and those of graphite in the carbon atom plane.

4. *References*

1. Gogotsi Y. et al. Nanoporous carbide-derived carbon with tunable pore size // Nature Materials. 2003. N 2. P. 591.
2. A. E. Kravchik, A. S. Osmakov, and R. G. Avarbe, “Analysis of the structure of carbon nanocrystalline and turbostratic materials,” Zh. Prikl. Khim ., No. 11, 2430 (1989).
3. A. I. Pokhodun et al., “Modernization of state primary standards for units of thermophysical quantities,” Izmer. Tekhn., o. 8, 55 (2009).
4. T. A. Kompan, “Metrological provisions for measuring the thermal expansion of materials. Critical analysis, development of the last decade and future development of themes in FGUP VNIIM im D. I. Mendeleeva” // Glavnyi Metro log, No. 4, 36, (2007)
5. S. I. Novikova, Thermal Expansion of Solids [in Russian], Nauka, Moscow (1974).

FORMATION OF STRUCTURE IN THE TINIHF SURFACE LAYERS WITH THE ASSESSMENT OF THEIR DURABILITY

ОСОБЕННОСТИ ФОРМИРОВАНИЯ СТРУКТУРЫ В ПОВЕРХНОСТНЫХ СЛОЯХ TiNiHf С ОЦЕНКОЙ ИХ ДОЛГОВЕЧНОСТИ

Conf. dr. Rusinov P.O.[1], Prof. dr. Blednova Zh.M.[2]
Faculty of Mechanical [1,2]– Kuban State Technological University, Russia

Abstract: *On the basis of complex metallophysical studies, surface-modified layers (electron microscopy, spectroscopy, X-ray diffraction, calorimetry, durometer analysis), we obtained new data on nanoscale composition within the surface-modified layer, on its mechanical properties, phase composition, which determines functional properties. This allows us to find ways of their purposeful formation for different operating conditions. On the basis of experimental data of X-ray analysis of the TiNiHf alloy, we calculated energy consumption, the theoretical strength. As a result of the simulation, we constructed generalized diagrams of energy intensity and theoretical strength of the ternary alloy Ti-Ni-Hf and compiled their relationship equation.*
***KEYWORDS**: SHAPE MEMORY EFFECT, HIGH SPEED FLAME SPRAYING, DURABILITY, STRENGTH, WEAR RESISTANCE*

1. Introduction

Modern trends in science and technology development make it necessary to improve the quality and advance the functional characteristics of the existing materials in order to expand the area of their practical use [1-10]. The priority development directions of materials and technologies include the development of intelligent, adaptive materials and coatings, including materials with shape memory effect (SME), as well as development of resourceful technology for their production [11-16]. Among the alloys with SME, TiNiHf is positioned as a high-temperature shape memory alloy, it is one of the most promising alloys because of its higher martensitic transformations temperatures and low cost [17,18]. Temperature of martensitic transformation has a significant impact on the physical and mechanical properties of shape memory alloys. While the temperature changes the work against the applied stress can be done; ie, heat is converted into mechanical action, which allows us to consider the shape memory materials to be functional ones. Between voltage, temperature and deformation in shape memory alloys, there is no uniquely ultimate dependence, which requires the development of methods for calculating the mechanical behavior of alloys with shape memory effect [19].

The aim of this study is to investigate the structure of the shape memory surface layers, obtained by high-velocity oxygen-fuel spraying of mechanically activated TiNiHf powder in a protective atmosphere with the assessment of their durability.

2. The experimental procedure

To form TiNiHf surface layers on steel we used the technology of high-velocity oxygen-fuel spraying of mechanically activated powders PN37T18GF45 and PNK1-VL7. Spraying of PN37T18GF45 was carried out via an intermediate layer of pure nickel Ni (δ = 100 microns), which provides a strong bond at the interface steel - TiNiHf, upon cylindrical (diameter 10 mm, steel 1045) samples. The total thickness of the layer was varied within 0.9 ÷ 1.1 mm.

Powders Ni, TiNiHf of PNK1-VL7, PN37T18GF45 brands for high-velocity oxy-fuel spraying were subjected to mechanical activation in a high-velocity planetary ball mill AGO-2U, drum rotation speed is 1200 min^{-1}, carrier rotation speed is 900 min^{-1}, the diameter of the steel balls is 6 mm, operation time the 10-30 min.

In the process of mechanical activation of PN37T18GF45 powder we observe its fragmentation and plastic deformation. PN37T18GF45 powder particles before mechanical activation are 40-60 microns, after mechanical activation they are 0.1 - 3 microns, with nanoparticles.

High-velocity oxygen-fuel spraying was carried out on a modernized universal plasma unit GLC-720, in a protective atmosphere (argon). As a result of mechanical process and statistical processing of technological parameters, we determined optimal modes of high-velocity oxy-fuel spraying of TiNiHf shape memory materials: propane flow rate of 60-85 l / min, oxygen - 120-160 l / min, powder consumption 190-210 g / min, the carrier gas (argon) flow - 40-50 l / min, spraying angle - 70 °, the burner moving speed - 0.2-0.3 m / min, the speed of the coated workpieces 500 rev / min, spraying distance of 300 mm.

TiNiHf surface layer was under thermomechanical processing cycle including mechanical, thermal and combined thermomechanical treatment.

X-ray analysis was performed on diffractometer Shimadzu XRD - 7000 in Cu-Ka radiation (λ = 1,54051). The microstructure and chemical analysis of the material steel-alloy TiNiHf was analyzed on an electron microscope of ultrahigh resolution JSM-7500F. Evaporation and heating of the sample was analyzed using arc and spark discharges, and then we carried out decrypts of the spectra and evaluation of the intensity of the spectral lines of the respective elements. Multi-cycle fatigue tests of steel 1045 cylindrical samples were carried out at the equipment MIE-6000. Quantitative assessment of durability was carried out by gravimetric method using an analytical balance WA-33. After deposition and machining to size, we held vacuum annealing of the samples: steel + TiNiHf at T = 1073K for 1 hour in order to impart the necessary functional mechanical properties to surface layer, it was subjected to thermomechanical processing by means of surface plastic deformation. Running by rollers of the cylindrical samples made of steel 1045 with TiNiHf coating was carried out under the following conditions: contact pressure (per roller) F = 3 ÷ 4 kN, roller diameter d1 = 50 mm, roller width b1 = 8 mm, the running speed v = 94 • 10-3 m / s, longitudinal feed - s = 0,08 mm / rev. Control over thermomechanical return of the samples, that were subjected to a combined treatment in a thermomechanical cycle, was carried out after heating to a reverse martensitic transformation temperature.

Structural and mechanical features of the surface layers formation using shape memory alloy. As a result of high-velocity oxygen-fuel spraying of mechanically activated powders, a layer with thickness of 1 mm (Fig. 2) is formed, it has a minimum amount of pores (less than 1%). The adhesion strength to the substrate layer increases (110-120 MPa).

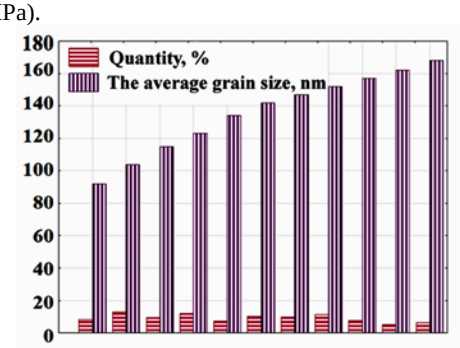
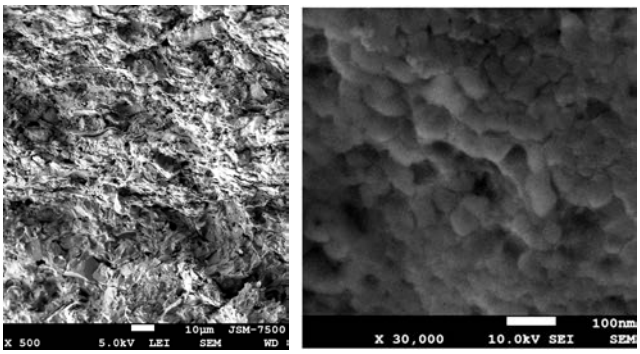


***Fig. 2.** The quantitative distribution of the grain size and their percentage in the TiNiHf layer*

Structure of a sprayed TiNiHf layer has extremely low etchability with conventional reagents, largely due to the strong grain refinement as a result of high-velocity heating, rapid cooling, and significant strain (Fig. 3); that provides specific structural effects. Due to characteristics of high-velocity oxy-fuel spraying of mechanically activated powder (high cooling rate and rapid hardening of the layer), during spraying in the cross-section of the TiNiHf layer there are no distinct columnar dendrites, the structure can be described as a nanocrystalline with grain size of 50-90 nm. Microhardness of TiNiHf layer varies H_μ = 9,7 ÷ 12,6 GPa.



a) b)

Fig. 3. *Nanostructured TiNiHf layer formed by high-velocity oxy-fuel spraying of mechanically activated powder in a protective atmosphere: thickness - 1 mm, × 500 - a), × 30000 - b)*

3. *A theoretical estimation of durability*

To evaluate the durability we used an option of energy model of damage accumulation in the surface-doped material for the two-component alloys, proposed by the following authors [20,21]. Models of [20,21] are reduced to the fact that for the destruction of the material, it is necessary to spend a part of the value of the irreversible deformation work. Only a certain amount of irreversible deformation work is spent for the accumulation of damage. To establish this amount, which depends on the heat transfer conditions, the degree of deformation, etc. we must refer to physical or mechanical experiments.

The energy spent in the crystal lattice distortion is determined from the expression [21]:

$$H = \int c_p \cdot dT \qquad (1)$$

where c_p – specific heat capacity, J / kg·K;
T – temperature, K;
T_{tm} – temperature of melting onset, K.
The limit energy (energy intensity), absorbed by the body, located at T, when melting, is determined from the expression:

$$Q = \int_{T}^{T_{tm}} c_p \cdot dT + L_{tm}\ , \qquad (2)$$

where L_{tm} – latent heat of fusion.
The theoretical strength is determined by the formula [21]:

$$\sigma_{teor} = \sqrt{E \cdot Q}\ , \qquad (3)$$

where E – Young's modulus, MPa.
Latent fusion heat is determined from the equation [21]:

$$L_{tm} = \Delta S_{tm} \cdot T_{tm}\ , \qquad (4)$$

where ΔS_{tm} – change in entropy of the body when it is melting.
Entropy of the melting is determined by the expression [21]:

$$\Delta S_{tm} = A_1 \cdot \Delta S_1 + A_2 \cdot \Delta S_2\ , \qquad (5)$$

According to the formula of the Neumann-Conn, heat capacity of alloys with shape memory effect is calculated using the formula [10]:

$$c_p = A_1 \cdot c_{p1} + A_2 \cdot c_{p2}\ , \qquad (6)$$

where c_p^1 и c_p^2 – the specific heat of the component alloy.
We carried out the calculation of energy consumption and the theoretical strength of the multi-component SME material TiNiHf, obtained by high-velocity oxygen-fuel spraying in a protective atmosphere (argon). Calculation of entropy and heat capacity was performed for each of the phases (Figure 4), included in the composite SME layer TiNiHf, according to formulas (5) and (6). Further calculation was made according to the formulas (1), (2), (3) and (4).
The results of X-ray analysis showed that at room temperature, the initial phase state of TiNiHf layer after a high-velocity oxygen-fuel spraying of mechanically activated powder is an austenitic TiNi B2 phases with a cubic lattice, martensite TiNi phases B19' with monoclinic lattice, intermetallic phases Ti_2Ni with a cubic lattice, HfNi phase with orthorhombic lattice, $HfNi_3$ phase with rhombohedral lattice, Hf0.24NiTi0.76 phase with a cubic lattice, we also observed a small amount of titanium oxide TiO, less than 3% (Fig. 4).

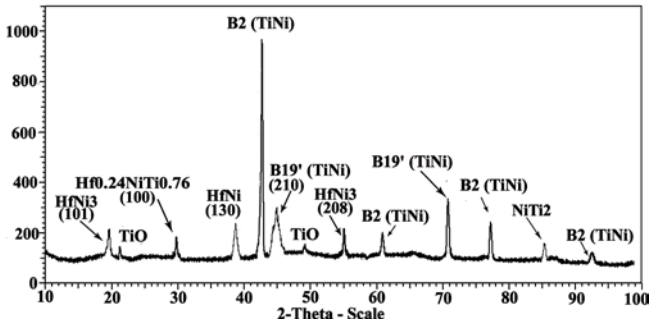


Fig. 4. *X-ray analysis of the TiNiHf alloy, after a high-velocity oxygen-fuel spraying with a local protection in argon atmosphere*

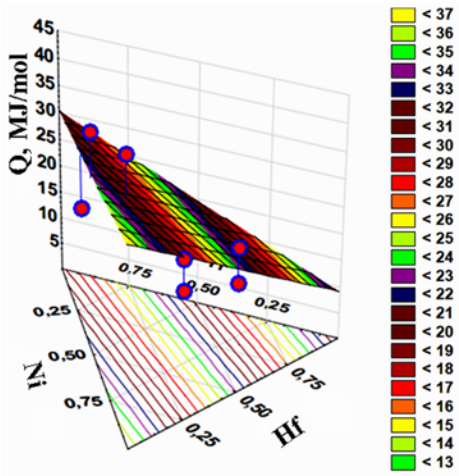
For phases TiNi, HfNi, Ti_2Ni, $HfNi_3$, Hf0.24NiTi0.76, TiO we counted (the energy of H, spent on the distortion of the crystal lattice; the ultimate energy Q, the energy absorbed by the body located at T, when it melts; σ_{teor} theoretical strength). Thus, the energy of H, spent on distortion of the phase crystal lattice Ni3Hf is equal to 23.9 MJ / kg; ultimate energy Q, the energy absorbed by the body is equal to 29.7 MJ / mol; σ_{teor} theoretical strength is 16,08GPa. We determined target values H, Q, σ_{teor} for all phases components and on the basis of statistical processing, we compiled the following equation:
- maximum Q, the energy absorbed by the body at the temperature T at its melting

$$Q = 37{,}0238 \cdot Ni + 9{,}1063 \cdot Hf + 30{,}3113 \cdot Ti \ \text{(MJ / mol)}, \qquad (7)$$

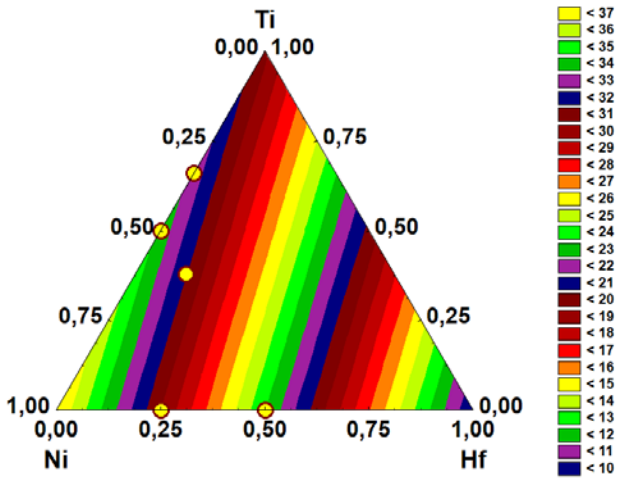
- theoretical strength σ_{teor} is described by the equation

$$\sigma_{teor} = -23{,}9847 + 5{,}3837 \cdot Q - 3{,}3905 \cdot H - 0{,}1314 \cdot Q^2 + 0{,}0833 \cdot Q \cdot H + 0{,}0314 \cdot H^2, \qquad (8)$$

where Ni, Hf, Ti – the percentage of SME in TiNiHf (at.%).
Fig. 5 shows the power consumption of system Ti-Ni-Hf alloys (a, b). Fig. 5 shows that power consumption value for the alloy system Ti-Ni-Hf, Ti-Ni-Zr with SME slightly differs from other connections of the system.



a)



b)

Fig. 5. *Power consumption of system Ti-Ni-Hf: three-dimensional (a) and two-dimensional model (b)*

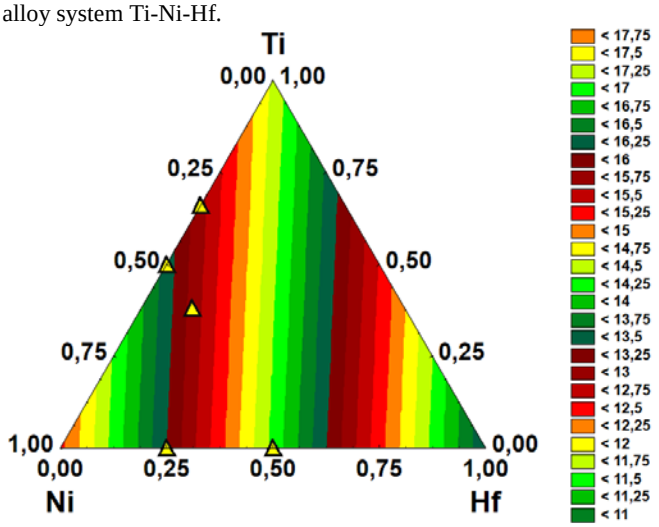
As a result of statistical processing of the calculated data, the limit energy Q, absorbed by the body located at temperature T when it melts is described by the equation

- for the layer Ti-Ni-Hf

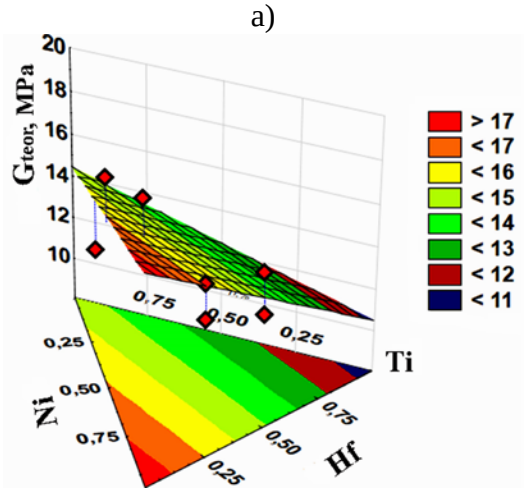
$$Q = 37{,}0238 \cdot Ni + 9{,}1063 \cdot Hf + 30{,}3113 \cdot Ti \quad \text{(MJ/mol)}, \qquad (9)$$

where Ni, Hf, Ti – the percentage of cells with SME, (at.%).

Fig. 6 shows a model for calculating the theoretical strength of the alloy system Ti-Ni-Hf.



a)

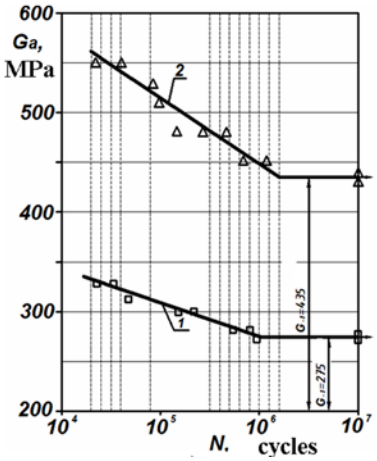


b)

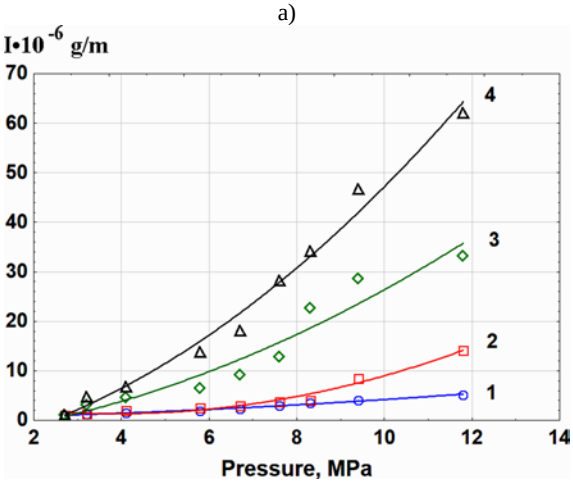
Fig. 6. *The theoretical strength of the systems Ti-Ni-Hf: a two-dimensional (a) and the three-dimensional model (b)*

4. The performance properties of the layers with shape memory alloy TiNiHf

In this paper, as showed the steel samples tests (steel 1045 + layer TiNiHf), on high cycle fatigue in bending with rotation, we can see increase in durability (Fig. 7) endurance limit (σ_{-1}) of steel 1045 without coating was 275 MPa, and after the surface modification with shape memory alloy TiNiHf - 435 MPa (increased by 36.8%). During the wear test of the samples with a surface layer TiNiHf, we observed increase in the surface temperature in the friction zone, causing austenite-martensite transformation. Large pressures, occuring at friction, cause the effect of transformation plasticity, due to the formation of martensite stress. The combination of these processes determines the durability of the sample. Improved wear resistance after full processing cycle is due to the considerable reversible plastic deformations (2.2%). Experience shows that the higher the reversible deformations, the higher the wear resistance. Increased wear resistance of steel 1045 with a surface SME layer TiNiHf is 2.6 times than that compared to steel 1045 (Fig. 7 b).



a)



b)

Fig. 7. *Cycle fatigue curves of steel 1045: no cover (1), after surface modification with shape memory alloy TiNiHf (2) - a); dependance of wear intensity I of TiNiHf layer from P drive pressure at the disk sliding speed of 0.5 m / s-1; 1 m / s -2; 1.5 m / -3; 2 m / s -4 - b)*

Increase of samples durability with nanostructured surface layer TiNiHf is explained both by features of nanostructured materials destruction, which is the slowdown in destruction at the grain boundaries, and movement obstruction cracks branching due to borders hardening, and by the pseudoelasticity of TiNiHf surface layer, inherent to materials with shape memory effect. Accumulated deformation by the surface layer is capable of recovering during cyclic loading and, thus, does not accumulate in the material, which increases its durability.

5. Summary

Complex formation method of a surface-modified layers using shape memory materials, which includes a high-velocity oxygen-fual spraying of mechanically activated powders based on TiNiHf, subsequent thermal and thermomechanical treatment allowed to form the nanoscale state in the surface layers, which have elevated level of functional, mechanical and performance properties. It is shown that preliminary mechanical activation of TiNiHf powder has reduced coatings porosity (less then 1%) and provided a bonding strength of the coating with the base (110-120 MPa). After the high-velocity oxygen-fual spraying in protective atmosphere of mechanically activated powder with shape memory efect based on TiNiHf, the cyclic durability under multi-cycle fatigue has increased by ~ 37% and the wear resistance - by 2.6 times, compared with steel 1045.

On the basis of complex metallophysical studies, surface-modified layers (electron microscopy, spectroscopy, X-ray diffraction, calorimetry, durometer analysis), we obtained new data on nanoscale composition within the surface-modified layer, on its mechanical properties, phase composition, which determines functional properties. This allows us to find ways of their purposeful formation for different operating conditions. On the basis of experimental data of X-ray analysis of the TiNiHf alloy, we calculated energy consumption, the theoretical strength. As a result of the simulation, we constructed generalized diagrams of energy intensity and theoretical strength of the ternary alloy Ti-Ni-Hf and compiled their relationship equation.

Acknowledgements

The work was performed as part of the state task № 9.555.2014 / K with the financial support of the Ministry of Education and Science of the Russian Federation and the President grant No MK-5445.2016.8.

References

1.Stavrev D., Dikova T., Modern Trends in Development and Strengthening of Tools Steels for Hot Strain, Proceedings of Scientific "Conference dedicated to 20th Anniversary of material Science and Technology Department", T U-Gabrovo, Bulgaria, March 2001, pp. 184-189.

2.Stavrev D., Russev D., Chakyrova D., Dikova T., Temperature Field in Prismatic Pattern during Thermal Cycling, Manufactiring Engineering and Technology, 2004, 1, pp. 35-40.

3. Glezer A., Plotnikova M., Dobatkin S., Perov N., Shalimova A. Effect of the High Pressure Torsion on Magnetic Properties of Amorphous Alloys. Materials Science Forum, 2011 volume 667, pp. 1077-1082.

4.Terent'ev V.F., Dobatkin S.V., Nikulin S.A., Kopylov V.I., Prosvi rnin D.V.,Rogachev S.O., Bannykh I. Fatigue strength of submicroc rystalline Tiand Zr2.5%Nb alloy after equal channel angular pressin g // Kovove Mater. - 2011. - V. 49.–N 1.–P. 65-73.

5. Rogachev S., Nikulin S., Dobatkin S., Terent'ev V., Kopylov V. The structure and properties of ultrafine-grained zirconium alloys // International virtual journal "Machines, technologies, materials".– 2011.–N 12.–P. 3-6.

6. Dobatkin S.V., Gubicza J., Shangina D.V., Bochvar N.R., Tabachkova N.Y. High strength and good electrical conductivity in Cu–Cr alloys processed by severe plastic deformation. Materials Letters. 2015. V.153. P. 5–9.

7. Vanadic alloys in atomic energy : thesis / S.A. Nikulin, S.N. Votinov, A.B. Rozhnov–Moscow: Publishing house MISiS, 2014.– 206 p.

8. A.G. Svyazhin, L.M. Kaputkina Dissolution and precipitation of excess phases in high-nitrogen steels. /Materials Science Forum Vols. 638-642 (2010) pp. 3026-3031.

9. L.M. Kaputkina, A.V. Skugorev. Strength aftermath, stress relaxation and phase transformations under pressure in deformed sheet steels // Structure-phase conditions of perspective metals / Edited by V.E. Gromov - Novokuznetsk: Publishing house, 2009. P. 230-258.

10. V. Anchev. Handbook of aluminum bonding technology and data: by J. Dean Minford; published by Marcel Dekker, Inc., New York, 1993.

11. V.Brailovski, S.Prokoshkin, P.Terriault, F.Trochu, Eds. Shape memory alloys: fundamentals, modeling and applications. Montreal, ETS Publ., 2003, 851 p.

12. V.G.Pushin, S.D. Prokoshin, R.Z. Valiev et.al. TiNi alloys with SME. Part I. Structure, phase transformations and properties. Ekaterinbourg: Russian Academy of Science. 2006, 439 p.

13. Blednova, Zh. M. Formation of Nanostructured Blankets from Materials with Shape Memory Effect (SME) in the Conditions of Plasma Dusting and their Optimisation for Maintenance of Functional-mechanical Properties [Text] / Zh. M. Blednova, P. O. Rusinov//Advances in nanotechnology.- Volume 10.- Editors: Z Bartul and J. Trenor.- Nova Science Publishers, New York.- 2012. – p. 61-109.

14. P.O. Rusinov, Ch.3 Surface engineering using multi-component SME materials Group thesis [Text] / P.O. Rusinov, Zh.M. Blednova // Scientific conclusions. - Moscow: Russian Academy of Science.- 2015. -231 p.

15. Zh.M. Blednova, N.A. Mahutov, P.O. Rusinov. Perspectives of SME materials to from multi-functional layers on the details of engineering sphere // Factory laboratory. Materials diagnostics.- 2013.- V. 79. - № 11.-P. 49-56.

16. Rusinov P.O., Blednova Zh.M., Balaev E.U., Dmitrenko D.V. Formation of composite layers TiNiZr-cBN-Co, working in conditions of cyclic loading and reverse friction. Procedia Structural Integrity 2 (2016), 1506–1513.

17. Xianglong Meng, Wei Cai, K.T.Lau, L.M.Zhou and Liancheng Zhao. Phase Transformation and Thermal Stability of Aged Ti-Ni-Hf High Temperature Shape Memory Alloys. J. Mater. Sci. Technol., Vol.22, No.5, 2006. 691-695.

18. Meng X.L, Cai W, Zheng Y.F, Zhao L.C. Phase transformation and precipitation in aged Ti–Ni–Hf high-temperature shape memory alloys. Materials Science and Engineering A. 438–440 (2006). pp. 666–670.

19. Perspective materials. Structure and methods of study / Edited by D.L. Merson - Tomsk State University, MISiS, 2006 – 536p.

20. Blednova Zh.M. Prognosis of cyclic durability of binary alloys and materials with coatings // Factory laboratory. – 1988. – № 7. – P. 76-81.

21.Blednova Zh.M. Increase in durability and cyclic strength for details by combined processing methods*:* Author's thesis for Doctor of Science. – Kiev, 1989. – 35 p.

STRUCTURE AND PROPERTIES HARD ALLOYS T5K10 WITH BORIDE COATINGS FORMED IN A MAGNETIC FIELD

СТРУКТУРА И СВОЙСТВА ТВЕРДЫХ СПЛАВОВ Т5К10 С БОРИДНЫМИ ПОКРЫТИЯМИ СФОРМИРОВАННЫМИ В МАГНИТНОМ ПОЛЕ

Prof. Dr. Chernega S.[(1)], Poliakov I.[(1)], Grinenko E.[(1)], Krasovskiy M.[(2)]
[1]National Technical University of Ukraine "Kiev Polytechnic Institute", 03056, Ukraine, Kiev, Polytechnique st., Bldg. 9, e-mail: smchernega@mail.ru; polykov_igor@mail.ru
[2]The Frantsevich Institute for Problems of Materials Science of NAS of Ukraine, 03680, Ukraine, Kiev, Krzhizhanovskogo st., 3

Abstract: *It was investigated the structure, phase and chemical composition, thickness diffusion boride layers obtained after boriding and complex saturation boron and copper with simultaneous action an external magnetic field (EMF) on solid alloy T5K10. It was established that the application of an external magnetic field allows to intensify the process of diffusion saturation hard alloys boron and by 2 hours chemical – thermal treatment with simultaneous action EMF get such thickness diffusion boride layer which is formed by 4 hours chemical – thermal treatment without EMF. It was found increase microhardness diffusion layers formed on the hard alloys on 2 – 2.5 GPa (30 - 30.5 GPa) that is associated with a decrease areas of coherent scattering and as a result increase operating parts that work in conditions of intensive wear.*

Keywords: *boron, boriding, boron layer, copper, structure, diffusion, microstructure, microhardness, external magnetic field.*

1. Introduction

Hard alloys provide high capacity under different operating conditions. Hard alloys WC-TiC-Co – titanium tungsten is used for the treatment of viscous materials: steel, brass [1 – 2], but their application field is narrowed due to low strength. One of the ways to improve the operational characteristics alloys are applying coatings, such as the use of chemical – heat treatment (CHT) [3 – 5]. However, doesn't definitive data on the positive effects of this method CHT to improve wear resistance hard alloys products [6 – 8]. To create technology of boriding hard alloys that gives stable results, it is necessary to investigate the mechanism of boride layer, processes of diffusion and redistribution of elements in boride layer and the transition zone hard alloy.

The aim of this work was to investigate the structure and characteristics of complex diffuse boride coatings on hard alloys obtained in boriding powder mixtures with the addition copper containing elements: Cu_2O with simultaneous action an external magnetic field.

2. Materials and Experiment

Processes borating and complex saturation with boron and copper performed powder method in a special at a temperature of 975 °C during 2, 4 and 6 hours using fusible valves. Saturation steels boron or boron and copper performed in powder mixtures on the basis of technical boron carbide B_4C with the addition of powders Cu_2O, as a source of copper and fluoroplast as activating additions.

To create a magnetic field coil (solenoid) used, which consisted of 635 windings tires aluminum alloy, the size of 10x20 mm; the current strength – 60 A; the magnetic induction – 35 mT. For magnetic thermo chemical treatment in coil placed high temperature furnace with crucible and packed in them saturated mixture for boriding with samples of hard alloys.

Investigation of the structure of boride coatings on hard alloys performed on microsections subjected a high temperature etching at 400°C at excerpt 30 minutes in the furnace with followed by cooling to room temperature in air.

Microstructural studies coatings and measuring the thickness of diffusion layers was carried out on metallographic microscope Axio Observer A1m, Zeiss, in the range the increase 100...1000.

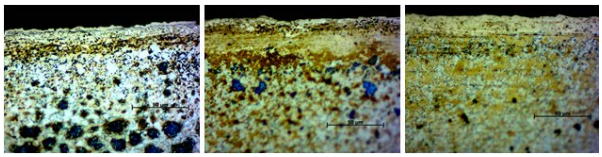
Microhardness measurements were carried out on the equipment PMT – 3 no less than 15 – 20 fields of view at a load of 0.49 – 0.98 N. Measuring accuracy microhardness was – ±300 MPa.

Research of the chemical composition of coatings performed micro X-ray spectral analysis on electronic scanning microscope – SEM 106 with increasing in 2000 time, accuracy – 0.01% by weight.

Phase composition, quantitative analysis phase, the periods of the crystal lattice, volume of elementary lattice phase, regions of coherent scattering in boride coatings were analyzed for X-ray diffractometer Ultima-IV of Rigaku (Japan), in the copper Kα monochromatic radiation.

3. Results and discussion

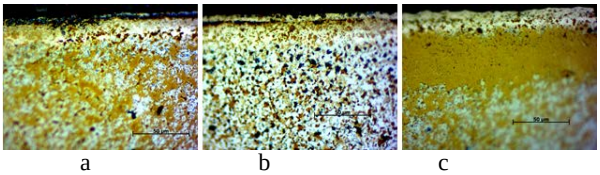
Investigation of the structure of hard alloy T5K10 with diffusion boride coatings obtained after boriding and complex saturation boron and copper in different physical – chemical conditions showed that after diffusion boriding during 4 hours on the surface hard alloy T5K10 formed diffusion layer thickness up to 25 μm (Fig. 1, a), and during 6 hours – up to 40 μm (Fig. 1, b). At applying the EMF on the surface of hard alloy T5K10 formed diffusion layer thickness up to 20 microns by 2 hours diffusion saturation (Fig. 1, c).



a b c

Fig.1: *Microstructures boride coatings on solid alloy T5K10 obtained after boriding without action EMP (a, b) by the duration of saturation 4 (a) and 6 (b) hours and in conditions action EMP (c) by the duration of saturation 2 hours, x500 (thermal etching)*

At the the complex saturation with boron and copper by 4 hours diffusion saturation on the surface of hard alloy T5K10 observed formation boride layer thickness up to 25 μm (Fig. 2, a), and by 6 hours - up to 35 μm (Fig. 2, b) whereas at complex saturation boron and copper with simultaneous action EMP by 2 hours forming diffusion layer thickness up to 23 μm (Fig. 2, c).



a b c

Fig.2: *Microstructures boride coatings on solid alloy T5K10 obtained after: a – complex saturation boron and copper without action EMP, duration saturation 4 hours; b – complex saturation boron and copper without action EMP, duration saturation 6 hours; c – complex saturation boron and copper in conditions action EMP, duration saturation 2 hours, x500 (thermal etching)*

Established that boriding with using EMF allows to increase microhardness of surface layers hard alloy T15K6 up to 30 – 30.5 GPa and complex saturation boron and copper – up to 28 GPa, in comparison with the diffusion boration without application EMF for which the microhardness amounts to 27,5 GPa, complex saturation boron and copper without action EMP – 25 GPa (Fig. 3).

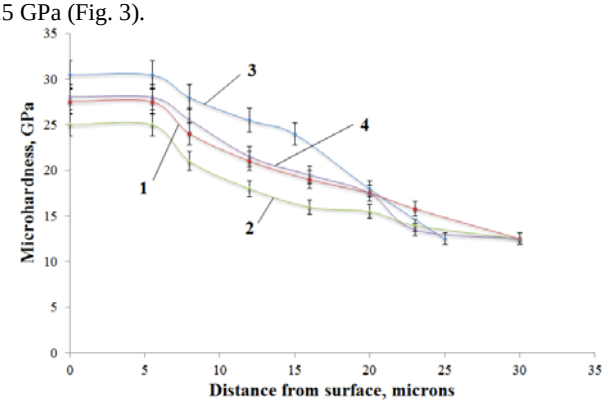
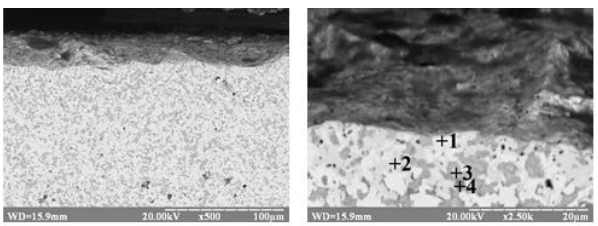


Fig.3: *Change microhardness by thickness diffusion boride coatings on hard alloy obtained in different physical – chemical conditions: 1 – boriding without EMF; 2 – complex saturation with boron and copper without EMF; 3 – boriding at the simultaneous action EMF; 4 – complex saturation with boron and copper with simultaneous action EMF*

To determine the chemical composition of the coating was applied microanalysis by using scanning electron microscope – SEM-106I with increasing in 2000 time, accuracy 0.01 wt. %.

Microrengenospectral analysis has established presence copper on the surface of boride coating (Fig. 4 – 5, Table 1 – 2). Formation separate inclusions copper leads to increased wear resistance, such as copper in the coating under dry frictional wear acts as solid lubricant.

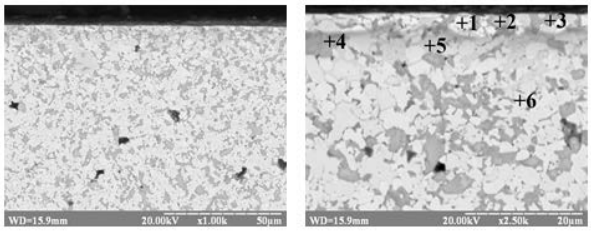


a b

Fig.4: *The structure of cross sections grindin with boride coatings on hard alloy T5K10 obtained after complex saturation boron and copper without action EMP by saturation duration 6 hours (a – x500; b – x2500) (chemical analysis determined the points +1, +2, +3, +4)*

Table 1. *The chemical composition of the diffusion boride layer on hard alloy T5K10, obtained after complex saturation boron and copper without action EMP*

Elem.	Position				
	General	+ 1	+ 2	+ 3	+ 4
	wt. %				
Ti (K)	7,17 ± 0,32	0,22 ± 0,18	0,19 ± 0,10	42,02 ± 0,70	11,31±0,49
Co (K)	12,90 ± 0,61	0,34 ± 0,26	35,88 ± 0,65	2,89 ± 0,38	44,37 ± 1,12
W (M)	79,06 ± 0,67	99,13 ± 1,73	63,93 ± 1,16	55,09 ± 1,05	40,68 ± 1,17
Cu (K)	0,87 ± 0,46	0,31 ± 0,19	0,00	0,00	3,64 ± 0,63



a b

Fig.5: *The structure of cross sections grindin with boride coatings on hard alloy T5K10, obtained after complex saturation boron and copper in conditions action EMP by saturation duration 2 hours (a – x1000; b – x2500) (chemical analysis determined the points +1, +2, +3, +4, +5, +6)*

Table 2. *The chemical composition of the diffusion boride layer on hard alloy T5K10, obtained after complex saturation boron and copper in conditions action EMP*

Elem.	Position						
	General	+ 1	+ 2	+ 3	+ 4	+ 5	+ 6
	wt. %						
Ti (K)	45,75±0,74	0,42±0,18	31,81±0,64	0,00	19,16±0,51	0,49±0,21	44,68±0,73
Co (K)	8,30±0,59	0,75±0,28	1,32±0,33	2,27±0,33	14,92±0,65	32,35±0,84	1,74±0,36
W (M)	45,12±0,77	98,83±1,52	66,87±1,24	97,20±1,85	65,92±1,21	67,16±1,18	53,58±1,17
Cu (K)	0,83±0,45	0,00	0,00	0,53 ± 0,41	0,00	0,00	0,00

To establish the phase composition boride coatings formed after boriding and complex saturation boron and copper in different physical – chemical conditions performed X-ray analysis.

At the study surfaces hard alloy T5K10 with diffusion boride coatings formed at boriding without action EMP X-ray analysis was established that in the surface layer up to 10 – 15 microns formed phases: B_2CoW_2, CoB, TiB, WB, TiC and WC (Fig. 6, Table 3).

At applying the EMP observed change the phase composition and on diffractograms taken from the surface of hard alloy T5K10 with diffusion boride coating obtained after boriding in conditions action EMP fixed presence phases CoB, Co_2B, TiB, WB, W2B, TiC та WC (Fig. 7, Table. 3).

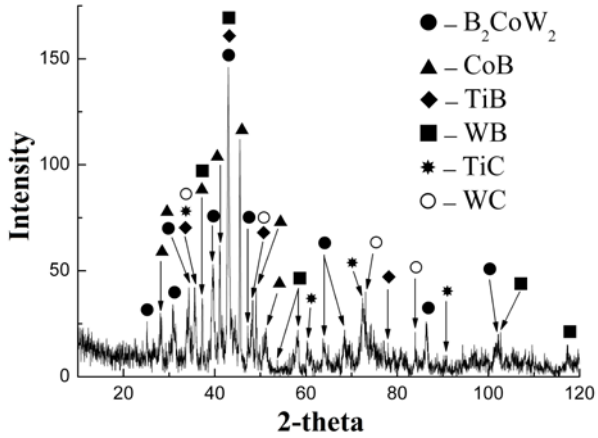


Fig.6: *Diffractograms taken from the surface of hard alloys T5K10 with boride coatings obtained after boriding without action EMP in Cu Kα monochromatic radiation*

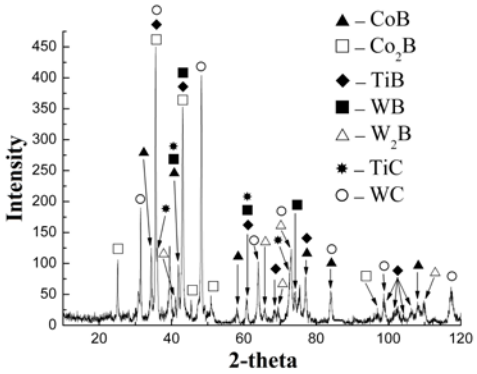


Fig.7: *Diffractograms taken from the surface of hard alloys T5K10 with boride coatings obtained after boriding in conditions action EMP in Cu Kα monochromatic radiation*

At the study diffusion boride coatings obtained after complex saturation boron and copper without action EMP was established following phase composition: B_2CoW_2, CoB, WB, TiC, WC and Cu (Fig. 8, Table 3).

After complex saturation boron and copper in conditions action EMP formed diffusion boride coatings next phase composition: B_2CoW_2, TiB, WB, WC and Cu (Fig. 9, Table. 3).

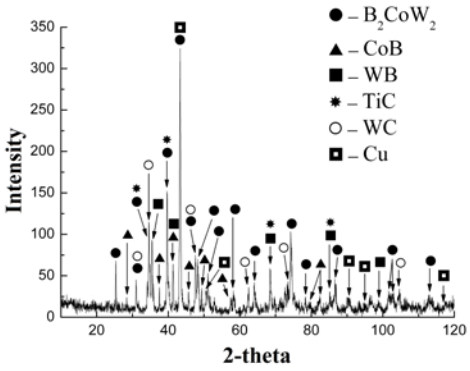


Fig.8: *Diffractograms taken from the surface of hard alloys T5K10 with boride coatings obtained after complex saturation boron and copper without action EMP in Cu Kα monochromatic radiation. Diffraction peaks Cu responsible crystallographic planes: (111) (200) (311) (222) (400)*

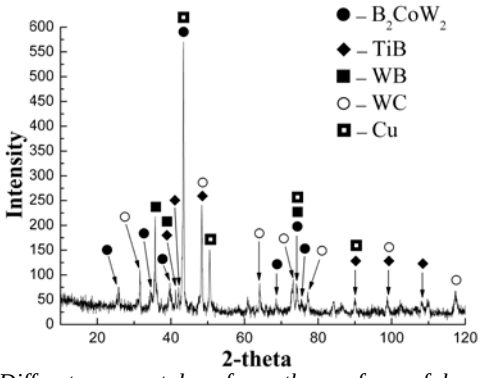


Fig.9: *Diffractograms taken from the surface of hard alloys T5K10 with boride coatings obtained after complex saturation boron and copper in conditions action EMP in Cu Kα monochromatic radiation. Diffraction peaks Cu responsible crystallographic planes: (111) (200) (311) (222) (400)*

Table 3. *The parameters crystal lattice phase and quantitative phase analysis of surface hard alloy T5K10 after boriding and complex saturation boron and copper in different physical – chemical conditions*

Process saturation	Phase	Parameters crystal lattice, Å			Volume of elementary crystal lattice (Å^3)	Areas coherent scattering (Å)
		a	b	c		
Boriding without action EMF	B_2CoW_2	7,095	4,560	3,186	103,082	151 ± 12
	CoB	3,963	5,253	3,052	63,539	131 ± 9
	TiB	6,232	2,999	4,466	83,490	176 ± 21
	WB	3,158	8,167	3,013	77,716	204 ± 10
	TiC	4,336	4,336	4,336	81,5	252 ± 49
	WC	2,908	2,908	2,844	20,832	247 ± 22
Boriding in conditions action EMF	CoB	3,861	5,221	2,993	60,319	85 ± 7
	Co_2B	5,019	5,019	4,191	105,591	-
	TiB	6,118	3,046	4,461	83,146	86 ± 7
	WB	3,267	8,403	3,033	83,257	97 ± 4
	W_2B	5,497	5,497	4,869	147,117	64 ± 3
	TiC	4,312	4,312	4,312	80,155	58 ± 3
	WC	2,910	2,910	2,837	20,809	98 ± 5
Complex saturation boron and copper without action EMP	B_2CoW_2	7,038	4,548	3,168	101,385	134 ± 8
	CoB	3,942	5,257	3,022	62,609	141 ± 7
	WB	3,252	8,504	3,143	86,916	249 ± 9
	TiC	4,537	4,537	4,537	93,421	65 ± 4
	WC	2,973	2,973	2,872	21,978	108 ± 5
	Cu	3,612	3.612	3.612	47,106	315 ± 28
Complex saturation boron and copper in conditions action EMP	B_2CoW_2	6,971	4,549	3,172	100,591	115 ± 10
	TiB	6,183	3.074	4,575	86,948	103 ± 4
	WB	3,260	8,379	3,146	85,953	105 ± 4
	WC	2,903	2,903	2,833	20,669	94 ± 15
	Cu	3,611	3,611	3,611	47,076	264 ± 18

Testing wear resistance were carried out on rollers produced of hard alloys, which are used to rolling aluminum profiles. Investigations have shown that the boride coating allow in 2 times increase the term of operation rollers. When the rollers working without coating can be made of 10 tons aluminum profiles, whereas at the application of the boride coatings is reached value of 21 tone.

4. Conclusions

At the application EMP allows in 2 times to reduce the duration of saturation products from hard alloys. Boride phases that are formed in the magnetic field have less periods, and accordingly the volume of elementary crystal lattices and less value areas of coherent scattering.

Established that the application of an external magnetic field allows to intensify the process of diffusion saturation hard and increase microhardness diffusion boride layers formed on the hard alloys on 2 – 2.5 GPa (30 - 30.5 GPa) and as a result increase operating parts that work in conditions of intensive wear.

5. *References*

[1] Bogoduhov S.I. Improving the performance of hard alloys by heat treatment / S.I. Bogoduhov, A.S. Kills, E.A. Shein, A.S. Yasakov, R.R. Khaibullin // Bulletin of the Orenburg State University. – №5 (124). – 2011. – P. 164 – 170.

[2] The use of plasma ceramic coatings in friction pairs of end seals / O.A. Zelenkevich, N.G. Taran, G.E. Lazarev, B.M. Kudryavtseva // Chemical and petroleum engineering. – 1990. – № 4. – P. 28 – 30.

[3] Klinskaya-Rudenskaya N.A. Comparative analysis of the composite coatings based alloys Ni-Cr-B-Si with refractory borides, obtained by different methods / N.A. Klin-Rudenskaya, V.A.Kopysov // Physics and Chemistry of Materials Processing. – 1995. – № 3. – P. 63 – 68.

[4] Moiseenko O.I. Tool materials / O.I. Moiseenko, H.O. Chkalov.–K.: Higher school, 1982. – 196 p.

[5] Berzina I.G. Distribution of boron, tungsten, titanium and cobalt alloys in solid borated / I.G. Berzina, E.B. Gusev, B.V. Zakharov, G.N. Fedin, V.M. Fedin // Physics of Metals and Metallography.–1984 – T.57, # 4. – P. 713 – 718.

[6] *Zakhariev Z.* Preparation and some properties of boride diffusion layers hard WC – TiC – Co alloys / Z. *Zakhariev, K. Petrov, M. Christov* // J. Less-Common Metals. – 1981. – 82. – P. 57 – 62.

[7] Berzina I.G. On the distribution of boron diffusion zone borated hard alloys used for the manufacture and machining of rolling stock / I.G. Berzina, E.B. Gusev, B.V. Zakharov and others // Proceedings of the Institute of Railway Engineers, Engineering. – 1982. – Vol. 701 – P. 24 – 27.

[8] Chernega S. Increace wear resistance hard alloys T15K6 boride coatings / Chernega S. Poliakov.I., Grinenko K., Krasovsky M.// Scientific technical journal "Material science. Non-equilibrium phase transformation" ISSUE 2/2015. – P.46 – 48 Publisher: scientific technical union of mechanical engineering/ ISSN 2367-749X. Sofia, Bulgaria.

SPARK PLASMA SINTERING THE COMPOSITES OF BIMODAL COPPER POWDERS

Prof. Grigoryev E. PhD., P.G. Nefedova E.
National Research Nuclear University MEPhI, Russia
eugengrig@mail.ru, nev_92@bk.ru

Abstract: *The present work is devoted to analysis of relations between the physical, mechanical properties and microstructure of the material produced by spark-plasma sintering (SPS) of bimodal copper powders. The used starting powders were bimodal mixtures of nano- and micro-sized copper powders, including the pre heat treatment of these powders in a hydrogen atmosphere. As a result, it was studied the influence of sintering parameters on the final density, microstructure and mechanical properties of bimodal copper sintered compacts. It was also produced a comparison of physical and mechanical properties of sintered samples obtained by SPS and by hot pressing (HP) from these bimodal copper powders.*

Keywords: COPPER POWDERS, SPARK PLASMA SINTERING, MECHANICAL PROPERTIES, MICROSTRUCTURE

1. Introduction

Optimization properties of nano- and ultrafine materials are important task of Material Science. It is known that nanocrystalline metals are characterized by high strength and hardness, but low ductility [1]. One way to increase the ductility is based on the creation materials with bimodal grain structure [2]. General principle of method is the nano- or ultrafine matrix provides a high strength, and evenly dispersed therein coarse grain contributes acceptable ductility. An important condition for preparing the bimodal material is to control and retention of the bimodal structure during processing. A great advantage over traditional methods, such as methods of severe plastic deformation of producing bimodal materials, exhibit electromagnetic methods of consolidation metal powders. SPS method [3] is promising for the development of materials, where need the collaborative and rapid consolidation of micro and nanosized powders. SPS technology can be used to produce materials with improvements in mechanical properties, microstructure, and other properties [4, 5].

2. Experimental

In this paper as the initial materials used copper powder of different fractional composition - a particle size of 40-90 μm and 50-70 nm. The morphology of copper powder is shown in Fig.1 [6]. As can be seen, nanopowder consists of microagglomerates which divided during the preparation of the powder mixture. The copper powder with a particle size of 50-70 nm was produced by "Advanced Powder Technologies", Russia.

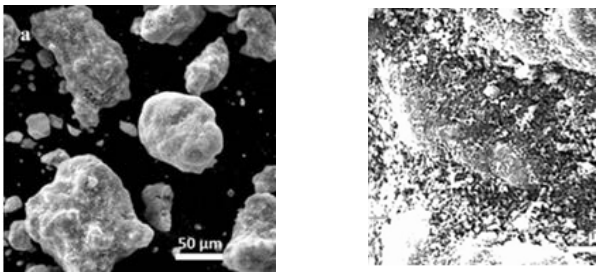


Fig. 1a *The SEM images of raw copper powders 50-70 nm.*

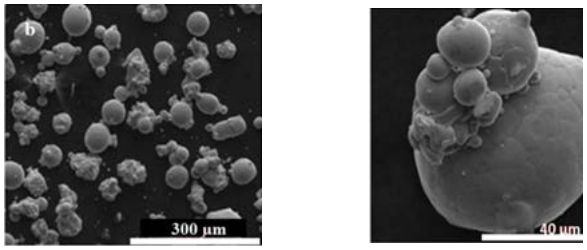


Fig. 1b *The SEM images of raw copper powders 40-90μm.*

The copper powder with a particle size of 40-90 μm was produced by Alfa Aesar company, USA. For the SPS-experiments it was used a copper micropowder of a coarse fraction 20-50 microns. Separation of the coarse fraction of copper powder was carried out in laboratory vibration equipment Fritsch Spartan. The particle sizes distribution of the composite of bimodal cupper powders is presented in Figures 2. The graph was obtained by using data from a laser analyzer of a particle size Fritsch Analysette 22.

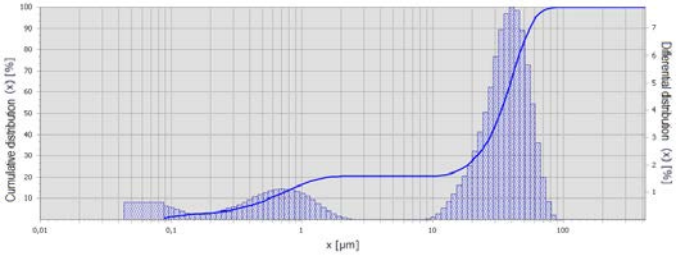


Fig. 2a *The particle size distribution of bimodal Cu powders.*

Nanodispersed copper powder contains metallic copper about 98%. In contact with air, metal content decreases to 85-90%. The average particle size of copper nanopowder has from 50 to 70 nm. Nanopowder agglomerates are easily formed, as can be seen in the Figure 1a by a scanning electron microscope JEOL 6610LV.

Initial nanopowders and micropowders were mixed in the mechanical mixer. The bimodal mixture (mass fraction of a micron-sized powder of 30%) was obtained by mixing nano and micro copper powders in a vertical automatic mixer MSK-SFM-2 for 6 hours. The density of the bimodal mixture of copper powder was 7.72 g/cm3. It was measured by an automatic helium pycnometer AccuPyc 1340. The powder sample has a mass of 2 grams. The initial relative density of powder compacts is 38%.

Experiments were conducted a spark-plasma sintering system model Labox-625 with pulse duration of 40 ms. A cylindrical graphite die with inner and outer diameters of 10 and 30 mm was used in the SPS process. The pressure in the vacuum chamber was 6 Pa. The temperature was measured using K-type thermocouple mounted in a hole on a lateral surface of the matrix.

In order to obtain relations of the relative density and microstructure of copper bimodal compacts on the SPS parameters were selected ranges of sintering parameters:

- Sintering temperature was varied from 200 to 600 °C, a pitch of 200°C;
- Pressure – from 20 to 50 MPa, 15MPa;
- Hearting rate was fixed parameter - 100°C/min.
- Holding time – from 3 to 6 min, 9 min;

Graphs of temperature modes spark plasma sintering are shown in Figures 3a, 3b, 3c.

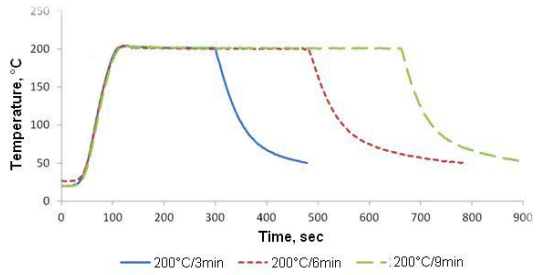


Fig. 3a *Temperature evolution during spark plasma sintering.*

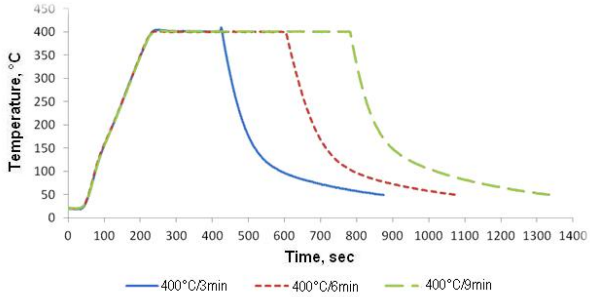


Fig. 3b *Temperature evolution during spark plasma sintering.*

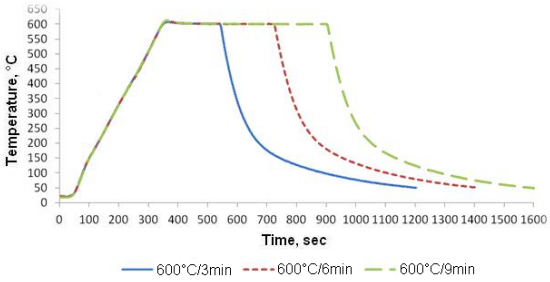


Fig. 3c *Temperature evolution during spark plasma sintering.*

The relations between different sintering parameters were obtained by the SPS output system. The density of the sample was measured by the Archimedes method. The microstructure of the bulk compact was observed by JEOL 6610LV scanning electron microscopy. The mechanical properties were tested using the hardness testing instrument (FM-800).

3. Results and discussion

Fig.4 shows the relation between the relative density of the bimodal copper compact and the sintering parameters. As seen from the graph, at a fixed value of sintering temperature was observed unessential change final density depending on the pressure and holding time. Thus at 200 °C and a selected range of changes pressure and holding time the relative density varies from 64.96 to 69.05% at 400 °C - 75,58-86,59% at 600 °C - 97.90 -99.45%.

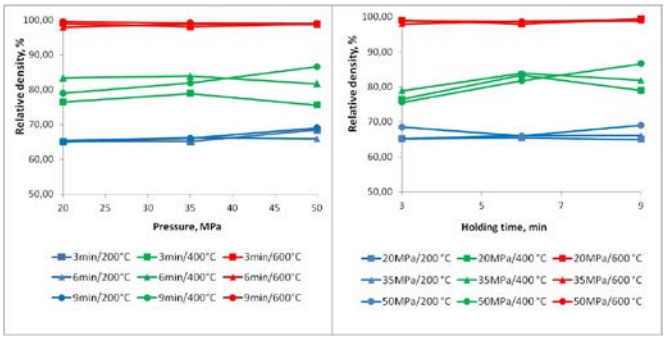


Fig. 4 *Effect of sintering temperature, pressure and holding time on relative density.* [6]

The kinetics of a powder densification during spark plasma sintering for 600°C/6min and different pressures: 20 MPa and 50 MPa are shown in Figures 5a, 5b.

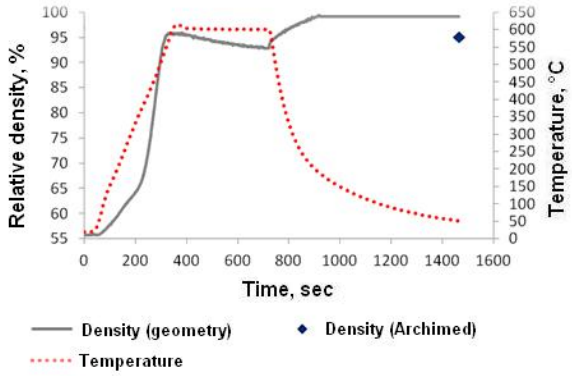


Fig. 5a *The evolution of a powder relative density during SPS for 600°C / 6 min, 20 MPa.*

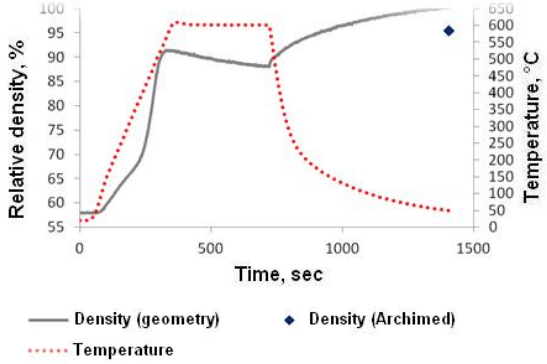


Fig. 5b *The evolution of a powder relative density during SPS for 600°C / 6 min, 50 MPa.*

Graphs 5a and 5b for the relative density of the compacts were built without correction for thermal expansion of the graphite punches.

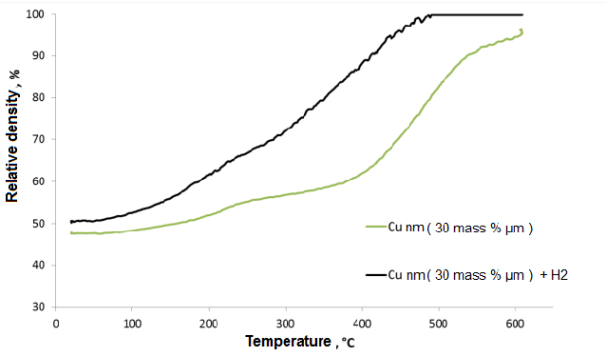


Fig. 6 *Densification kinetics of bimodal copper powders during SPS for 600°C / 6 min, 35 MPa.*

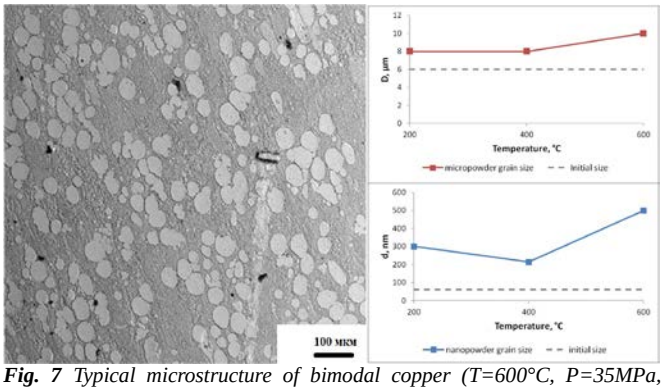


Fig. 7 *Typical microstructure of bimodal copper (T=600°C, P=35MPa, t=6min, v=100°C/min) and the relation between grain sizes and sintering temperature.*

The densification kinetics bimodal mixtures of initial copper powders and annealed in hydrogen copper powders (Figure 6) shows that the initial copper powders are unstable and the shrinkage rate has a distinct discontinuity in the temperature range from 400 to 500 ° C.

Typical microstructure of bimodal copper samples is shown in Fig.7. As can be seen, coarse powder particles are uniformly distributed in the volume of densely sintered nanopowder.

Since the temperature is a key factor affecting the final density of the samples, the dependence of the grain size was considered on the temperature at fixed values of pressure and holding time. Thus the average grain size on the range of temperatures was 8-10μm. The final grain size of the nanopowder varies depending on the sintering temperature ranging from 200 to 500 nm.

In order to compare the mechanical properties of mono- and bimodal copper prepared by SPS, a sample with a diameter of 10 mm was prepared. The following parameters were selected: T=600°C, P=35MPa, t=6min, v=100°C/min. As a result, the microhardness of bimodal sample (180 HV) is higher than that of the micro- (63 HV) and nanosamples (159 HV) obtained by SPS.

4. Conclusions

In this research, a bimodal Cu was synthesized by SPS successfully. The effects of sintering temperature, holding time, pressure and heating rate on the relative density, microstructure and mechanical properties of the samples were investigated. The results are shown:

- The sintering temperature increased density significantly. Extending the pressure and holding time can also cause density to increase, but not as much as the temperature.
- The sintering temperature has a significant effect on grain size of initial nanopowder, while the coarse grains don't grow.
- The SPS fabricated bimodal Cu has a high microhardness, compared with micro- and nanocrystalline samples.

5. Acknowledgements

The support of the Department of Science and Education of Russian Federation (Grant Contract 11.G34.31.0051) is gratefully appreciated.

6. References

[1] M.A. Meyers et al. / Progress in Materials Science 51 (2006) 427–556

[2] Wang Y. et al. / Nature. 419 (2002) 912-915

[3] Masao Tokita / Handbook of Advanced Ceramics (2013) 1149-1177

[4] Z.-H. Zhang et al. / Materials Science and Engineering A 476 (2008) 201–205

[5] C. Yang et al. / Materials Science & Engineering A 625 (2015) 264–270

[6] E. Nefedova, E. Aleksandrova, E. Grigoryev, E. Olevsky / Physics Procedia, Volume 72, p. 390-393.

REGULARITIES OF INFLUENCE OF NICKEL AND CHROMIUM ON STRUCTURE FORMATION OF ELECTRODEPOSITED IRON

Ph. D. Kolesnyk Ie.V.[1], Dr.Sc. (Eng.) Bagliuk G.A.[2]
Ukrainian State University of Chemical Technology, Dnipro, Ukraine [1],
Frantsevych Institute for Problems of Materials Science, National Academy of Science of Ukraine, Kyiv, Ukraine [2]
E-mail: ievgen.kolesnyk@ukr.net, gbag@rambler.ru

Abstract: *Structural investigations performed by the methods of X-ray diffractometry and scanning electron microscopy of electrodeposited iron-based coatings revealed common and specific features and regularities of influence of nickel and chromium on their structure formation. Significant changes in surface morphology, crystallographic texture and microhardness of the electrodeposited coatings caused by the insertion of nickel and chromium in the sulfate iron-plating electrolyte were found and compared.*
KEYWORDS*: ELECTRODEPSOITED IRON, NICKEL, CHROMIUM, ALLOY, COATING, CRYSTALLOGRAPHIC TEXTURE, SURFACE MORPHOLOGY*

1. Introduction

Electrodeposited iron is used in industry particularly as coatings to restore worn steel machine parts of various type [1-2]. In comparison with materials obtained by metallurgical methods electrodeposited coatings usually possess increased hardness. Therefore, the use of electrodeposited iron coatings also provides surface hardening of steel items, which should be mentioned as their additional advantage.

To improve the performance of electrodeposited iron its alloying by various metal elements with the formation of electrodeposited alloys is utilized [2-3].

2. Preconditions and means for resolving the problem

Analysis of the literature showed that the majority of publications on electrodeposited iron-based alloys focus on electrochemical aspects of their production, while their structure formation is discussed insufficiently and the available data on the influence of alloying elements on the processes of structure formation is not systematized. Therefore, to find new possible ways of improvement of the complex of properties of iron coatings the investigations of influence of alloying elements on structure formation of electrodeposited iron is sufficiently urgent.

In previous research it was shown that the presence of nickel [3-5], chromium [6-7] or both alloying elements [8-11] in iron-plating electrolytes causes significant changes in structure formation of electrodeposited iron-based coatings. Thus, our recent investigations in this field [5, 7, 11-12] revealed drastic changes in surface morphology and crystallographic texture of such nickel- and chromium-alloyed iron coatings obtained from sulfate electrolyte. But it should be noted that the structure formation of electrodeposited metal coatings usually occurs in non-equilibrium conditions and depends on the process parameters and electrolyte composition significantly, which may lead to the formation of quiet unusual phase composition [13-14] and surface morphology [14] of coatings. Therefore, the prediction of structure of electrodeposited coatings is hindered and experimental investigations are still necessary in every case of usage of such coatings.

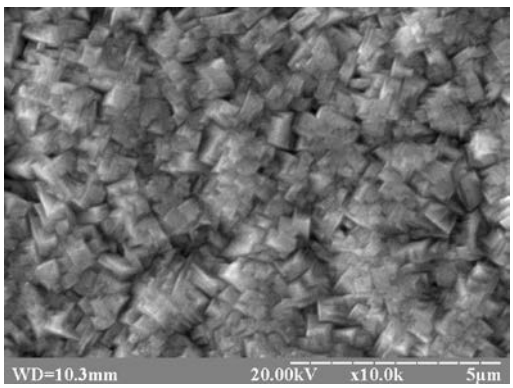
Thus, the aim of this work was further investigation, establishment and explanation of features and regularities of influence of nickel and chromium on structure formation of electrodeposited iron coatings obtained from sulfate electrolyte.

Iron-based coatings (1-150 μm thick) were electrodeposited at the temperature of 55-57°C and the current density of 10 A/dm^2 from sulfate electrolytes containing: Fe – 80 g/l, Ni – 0-40 g/l, Cr – 0-40 g/l (pH 2-3). The sources of Fe, Ni and Cr ions in the electrolyte were the sulfates $FeSO_4 \cdot 7H_2O$, $NiSO_4 \cdot 7H_2O$ and $Cr_2(SO_4)_3 \cdot 6H_2O$ respectively. Also $Al_2(SO_4)_3 \cdot 18H_2O$ (100 g/l) was used as a buffering substance. Iron anodes were utilized during deposition process. Industrial steel sheet 08kp without mechanical pretreatment was used as a substrate.

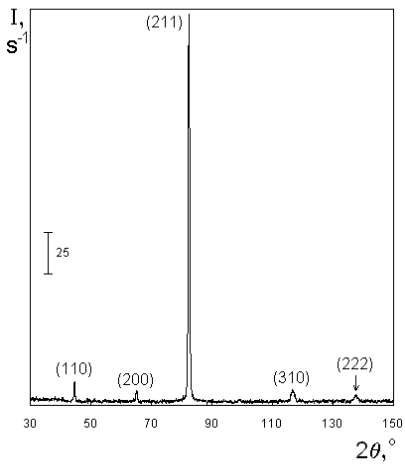
Surface morphology and element composition of the obtained coatings were investigated by scanning electron microscopy at the REM-106I microscope. Phase composition and crystallographic texture were determined by X-ray diffractometry at the DRON diffractometer in Cu-K_α radiation.

3. Results and discussions

The surface structure of electrodeposited iron without alloying at the thickness of 15 μm is represented mainly by fine non-equiaxial crystals. With the increase of thickness to 50 μm and above tightly arranged equiaxial crystals with clear cut begin to dominate in the coatings (Fig. 1, a) and the surface relief becomes noticeably smoother.



a



b

Fig. 1. *Surface morphology (a) and X-ray diffractogram (b) of electrodeposited iron without alloying, coating thickness 50 μm*

Crystallographic texture of electrodeposited iron (15-150 μm thick) is characterized by a strong axial <211> component (Fig. 1, b). Moreover, with the increase of thickness of the coatings in the investigated range the degree of perfection of texture increases.

Root-mean-square static displacements of atoms relative to their equilibrium positions in the crystal lattice equal 0.122 and 0,076 Å for the 15 and 50 μm thick iron coatings respectively, indicating more non-equilibrium conditions at the initial stage of electrodeposition process, which leads to the formation of a more defective structure in thin coatings.

It is established that phase composition of all investigated coatings alloyed with nickel and chromium contains solid solutions based on the crystal lattice of α-Fe. Intermetallic compounds were not found in the coatings.

The content of chromium and nickel in the alloys increases with the increase of their concentration in the sulfate electrolyte throughout the whole investigated range (Fig. 2). However, for the Fe-Ni coatings such dependence is of an exponential type, while for the Fe-Cr alloys it is close to a logarithmic type, which is caused by a significant difference in the deposition rates of nickel and chromium at their different concentrations in the electrolyte.

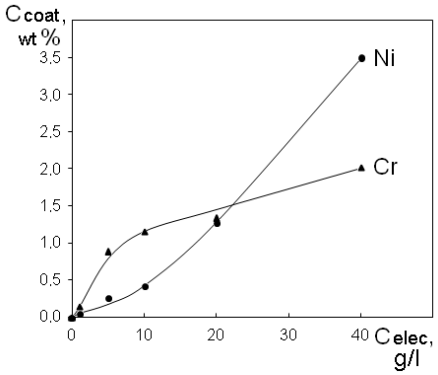


Fig. 2 *Dependence of alloying element content in the coating on its concentration in the electrolyte*

Analysis of cross-sections of the electrodeposited alloys Fe-Ni and Fe-Cr showed that the distribution of elements in both types of coatings is sufficiently uniform in thickness. Thus, after deposition of the initial layers the content of elements quickly stabilizes, which is observed at the thickness of about 8-10 and 10-12 μm for the Fe-Ni (Fig. 3, a) and Fe-Cr (Fig. 3, b) alloys respectively.

The surface structure of the Fe-Cr alloys electrodeposited from the sulfate electrolyte with 1 g/l Cr concentration is highly dispersed and consists mainly of small crystals (less than 1 μm) without clear cut forming a much smoother surface relief than the surface of electrodeposited iron without alloying. The increase of chromium concentration to 5 g/l is accompanied by a slight increase in the average crystal size and by the formation of relatively large crystal conglomerates. However, this structure, which looks coarser in comparison with the non-alloyed iron structure, actually consists of finer crystals forming such conglomerates. Further increase of the chromium concentration to 20 g/l leads to a gradual increase of the crystal size and at the concentration of 40 g/l some large crystals (more than 1 μm) appear in the surface structure of the alloy.

The insertion of nickel in the sulfate electrolyte and the increase of its concentration lead to significant changes in the type of crystal structure of the deposits. Thus, at the 5 g/l nickel concentration mainly fine needle-like crystals are present in the structure of the coatings, while the increase of its concentration to 10g /l leads to a significant increase of the share of spherulites, and further increase to 20 g/l is accompanied by the formation of a fully spherulite structure without any other forms of crystal growth.

Despite the relatively small amount of alloying elements in the obtained coatings (Fig. 2) the results of measurements indicate a significant influence of alloying on microhardness of the electrodeposited iron-based alloys (Table 1). And the character of change of microhardness of the investigated coatings depending on the concentration of alloying elements is nonlinear and very similar for nickel and chromium (Table 1).

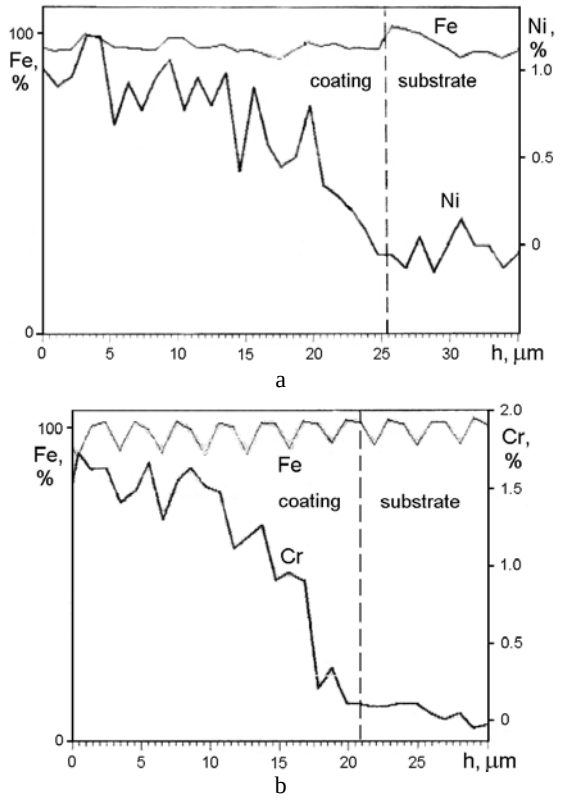


Fig. 3 *Elements distribution in cross-section of iron-based coatings alloyed with nickel (a) and chromium (b)*

Table 1. Microhardness of electrodeposited Fe-Cr and Fe-Ni alloys (50 μm)

Alloying element concentration in the electrolyte, g/l	Microhardness HV 0,05, GPa	
	Fe-Ni	Fe-Cr
0	4.57	4.57
1	4.49	4.18
5	4.29	3.48
10	4.60	4.60
20	5.58	5.72
40	5.21	4.55

The cause of such nonlinear change of microhardness of the investigated electrodeposited coatings is the features of their structure formation. Thus, at the 5 g/l chromium or nickel concentration in the electrolyte mostly fine needle-like crystals dominate in the structure of the coatings in contrast to iron coatings without alloying. In the Fe-Ni alloys such crystals have a preferential <111> orientation and form a relatively smooth surface relief of the coatings. In the Fe-Cr alloys fine crystals form conglomerates of different sizes. In this case the preferential <211> crystal orientation typical for electrodeposited iron is preserved but the fraction of disordered crystals significantly increases. These structural changes lead to a reduction of microhardness of the coatings.

Further increase of the concentration of the alloying elements in the electrolyte to 20 g/l results in gradual growth of microhardness, which may be associated with the formation of specific structural components in the coatings. Thus, in the Fe-Ni alloys fine crystals form spherulites – the crystal units of radial-beam structure (Fig. 4, a). In the Fe-Cr alloys the formation of spherulites is not observed, however the formation of crystal

conglomerates occur (Fig. 5, a). Crystallographic texture of the coatings obtained at such concentration of the electrolytes is also represented by the axial <111> and <211> orientations for the Fe-Ni and Fe-Cr alloys respectively (Fig. 4, b and Fig. 5, b).

Further increase of the concentration of the alloying elements in the electrolyte to 40 g/l leads to structural heterogeneity of the electrodeposited coatings. Thus, in the surface structure of the Fe-Cr alloys some large crystals can be observed. And in the Fe-Ni alloys some areas of disordered needle-like crystals occur between spherulites with distinct radial-beam symmetry. At this concentration of nickel the fraction of crystals with axial <111> orientation typical for spherulite structure decreases. As it turns out in this case the structural heterogeneity is associated with a certain reduction of microhardness of the coatings.

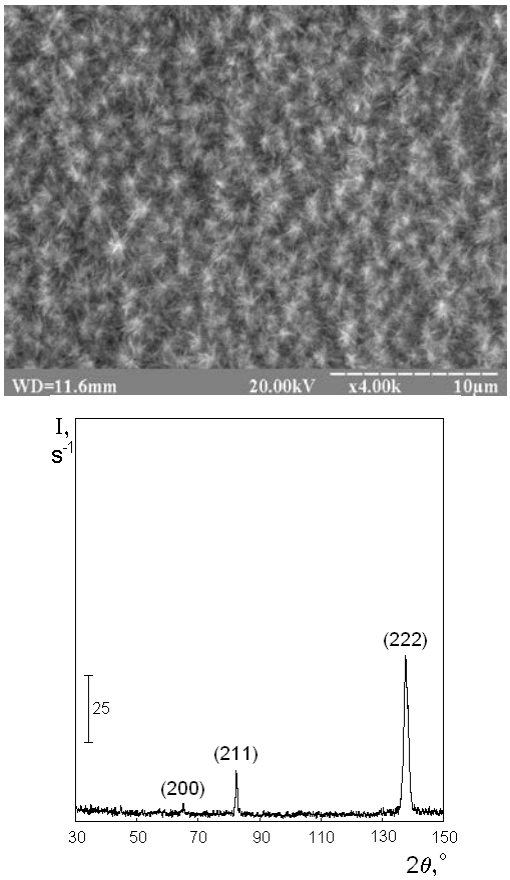


Fig. 4. *Surface morphology (a) and X-ray diffractogram (b) of electrodeposited Fe-Ni alloy (50 µm) electrodeposited from the electrolyte with 20 g/l of Ni*

4. Conclusions

The main common regularities of influence of nickel and chromium on structure formation of electrodeposited iron are the formation of solid solutions and fine structures as well as the identical character of change of microhardness of the alloyed iron coatings. The main specific regularities of influence of nickel are the formation of strong <111> axial texture and a fundamental change in surface morphology of the coatings from fine crystal structure with clear cut to the formation of spherulites, while the insertion of chromium in the electrolyte nearly does not change the <211> axial texture of electrodeposited iron.

The essential difference between the characters of the dependences of the average content of an alloying element in the coating on its concentration in the electrolyte is established for nickel and chromium. This dependence for nickel-alloyed coatings is of an exponential type, while for the chromium-alloyed coatings it is close to a logarithmic type, which is caused by a significant difference in the deposition rates of nickel and chromium at their different concentrations in the electrolyte.

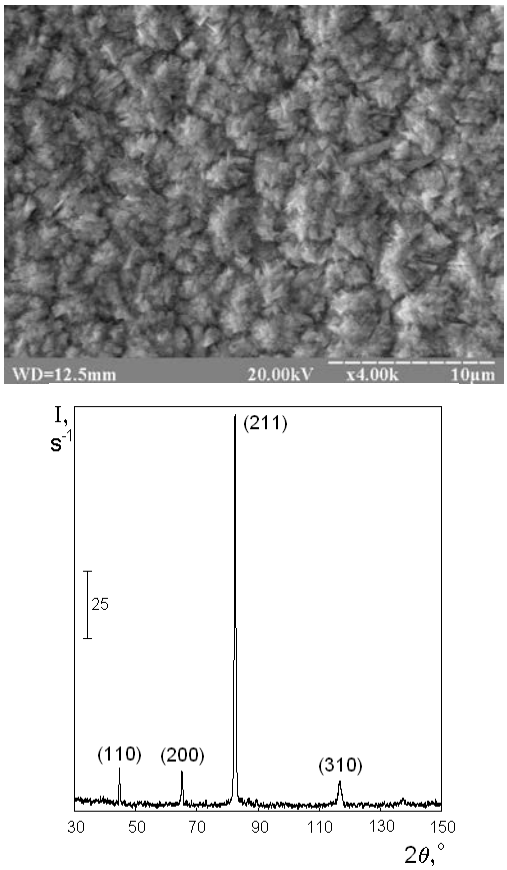


Fig. 5. *Surface morphology (a) and X-ray diffractogram (b) of electrodeposited Fe-Ni alloy (50 µm) electrodeposited from the electrolyte with 20 g/l of Cr*

5. Literature

1. Likhachev V.A., Restoration of worn machine parts by the method of cold iron-plating, Galvanotekhnika i Obrabotka Poverkhnosti. 14 (2006) 14-18. (In Russian)

2. Pleshka E.D., Iron coatings from multicomponent methyl sulfate chloride electrolyte, Surface Engineering and Applied Electrochemistry. 44 (2008) 264-270.

3. Kolesnyk Ie., Influence of metal ions in iron-plating solution on structure formation of electrodeposited iron-based coatings, Chimia. 67 (2013) 575.

4. Nakamura K., Umetani M., Hayashi T., Electrodeposition of iron-rich Ni-Fe alloys from sulphate and chloride baths, Surface Technology. 25 (1985) 111-119.

5. Kolesnyk Ie.V., Features of structure formation of electrodeposited alloys Fe-Ni, Scientific Bulletin of National Mining University. 137 (2013): 62-66. (In Russian)

6. Wang F., Watanabe T., Preparation and characterization of the electrodeposited Fe-Cr alloy film, Materials Science and Engineering A. 349 (2003): 183-190.

7. Kolesnyk Ie.V., Velychko M.T., Features of structure formation of electrodeposited Fe-Cr coatings, Metaloznavsto ta Termichna Obrobka Metaliv. 63 (2013) 64-68. (In Russian)

8. Sziráki L., Kuzmann E., El-Sharif M., et al., Electrochemical behavior of electrodeposited strongly disordered Fe-Ni-Cr Alloys, Electrochemistry Communications. 2 (2000) 619-625.

9. Sziráki L., Kuzmann E., Chisholm C.U., et al., Characterization of the passive films on electrodeposited Fe-Ni-Cr alloys in borate solution at pH 8.4, Central European Journal of Chemistry. 5 (2007) 931-950.

10. Adelkhani H., Arshadi M.R., Properties of Fe-Ni-Cr alloy coatings by using direct and pulse current electrodeposition, Journal of Alloys and Compounds. 476 (2009) 234-237.

11. Kolesnyk Ie.V. Joint effect of chromium and nickel on surface morphology and preferred crystal orientations of electrodeposited iron-based coatings, Metallofizika i Noveishie Tekhnologii. 37 (2015) 347-354.

12. Kolesnyk Ie.V., Bagliuk G.A. Comparative analysis of structure and properties of electrodeposited iron and Fe-Cr-Ni alloy coatings, Metaloznavstvo ta obrobka metaliv. 1 (2016) 23-28. (In Ukrainian)

13. Kolesnyk Ie.V. Phase composition of electrodeposited Fe-Zn alloys, Metallofizika i Noveishie Tekhnologii. 37 (2015) 257-264.

14. Kolesnyk Ie.V. The laws governing structure formation in Fe-Zn alloys electrodeposited from sulfate electrolytes, Surface Engineering and Applied Electrochemistry. 51 (2015) 235-239.

THE EFFECT OF FLUORIDE ON CORROSION BEHAVIOUR OF AUSTENITIC STAINLESS STEEL

RNDr. Viera Zatkalíková, PhD., Ing. Lenka Markovičová, PhD., Ing. Monika Oravcová

Department of Materials Engineering, Faculty of Mechanical Engineering, University of Žilina, Slovakia

viera.zatkalikova@fstroj.uniza.sk

Abstract: *Austenitic stainless steels are widely used for various industrial, construction and biomedical application because of their high resistance to uniform corrosion and suitable mechanical properties. However, they are prone to local corrosion in aggressive halides environments. In contrast of corrosion resistance research in chloride containing environments, there have been few investigations into the effect of fluorides on passivity breakdown and pitting corrosion of stainless steels. This article focuses on the effect of fluoride added to chloride solution on corrosion resistance of AISI 316L stainless steel. Evaluation is based on results of exposition immersion tests performed in 0.9 % NaCl, 0.9 % NaCl + 0.05 % NaF and 0.9 % NaCl + 0. 5 % NaF solutions (42 days) and on results of cyclic potentiodynamic polarization tests performed in the same solutions.*

Keywords: AUSTENITIC STAINLESS STEEL, PITTING CORROSION, FLUORIDE, IMMERSION TEST, CYCLIC POTENTIODYNAMIC TEST

1. Introduction

Despite their high resistance to uniform corrosion, austenitic stainless steels are prone to local pitting corrosion in halides containing environments. This corrosion form is typical for passivating metals and alloys. Aggressive ions present in solution can penetrate through the weakened places of surface passive film and cause its local breakdown and initiation of the pitting corrosion [1-3].

Chlorides are the most common aggressive anions present in industrial environments. However, often they are not the only aggressive components but tend to be mixed with fluorides. In contrast of corrosion resistance research in chloride containing environments, there have been few investigations into the effect of fluorides on passivity breakdown and pitting corrosion of stainless steels. Moreover, the results obtained are inconsistent and do not lead to the same conclusions [4-8].

The authors [4] studied corrosion resistance of unspecified stainless steel wires in artificial saliva with 0.05 and 0.2 wt. % fluoride additions. Based on the potentiostatic and potentiodynamic tests the authors found that the addition of fluoride decreased the corrosion resistance of all archwires tested. Contrary to these conclusions the authors [7] studied resistance of austenitic stainless steel (alloy 22) to local corrosion and they described inhibitive effect of fluoride anions at the concentration ratio of fluoride to chloride anions higher than two. The authors [8] evaluated the pitting behavior of AISI 304 stainless steel in neutral chloride solutions. It has been confirmed by potentiodynamic measurements that fluoride anions inhibit the chloride induced pitting corrosion but promote the uniform dissolution of the steel [8].

AISI 316L is Cr-Ni-Mo austenitic stainless widely used in various industrial and biomedical applications. This paper deals with the effect of fluoride anions (0.05 % NaF and 0.5 % NaF) added to chloride solution (0.9 % NaCl) on the pitting corrosion resistance of the above mentioned steel. Evaluation of the corrosion resistance is based on the results of exposure immersion tests (microscopic observation of attacked surfaces, mass losses of specimens) and on the results of the cyclic potentiodynamic polarization tests. Results of immersion tests were evaluated on the bases of corrosion rates calculated from corrosion losses during immersion and by morphology of pitting. Results of potentiodynamic polarisation tests were evaluated by pitting potentials.

2. Experimental material

AISI 316L stainless, steel with chemical composition listed in Table 1, was used as an experimental material.

Table 1: *Chemical composition of experimental material (wt. %)*

Cr	Ni	Mo	Mn	N
16.79	10.14	2.03	0.82	0.05
C	Si	P	S	Fe
0.02	0.31	0.03	0.001	balance

Microstructure of experimental material (optical metallographic microscope Neophot 32) in longitudinal section is shown in Fig. 1. It is created by polyedric austenitic grains with observable twins, which could be created by annealing or by rolling. Parallel lines arose by the rolling during the technologic process. Observed microstructure contains numerous carbides. $(Mo, Cr)_{23}C_6$ carbides [9] are localized along the above mentioned lines.

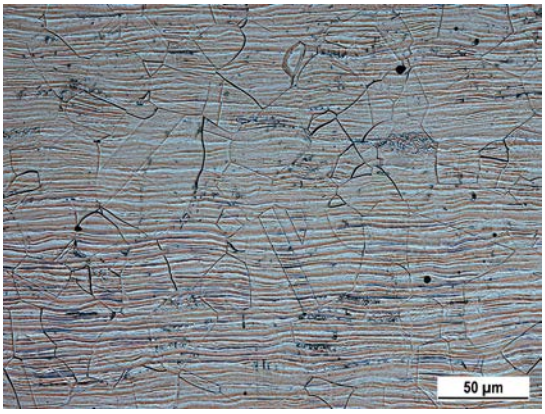


Fig. 1 *Microstructure of AISI 316L stainless steel in longitudinal section (Kalling's etch)*

3. Experimental conditions and methods

0.9 % (0.15 M) NaCl solution was used as the basic corrosion environment for both immersion and potentiodynamic polarisation tests. The basic solution was applied without fluoride and with two additions of sodium fluoride: 0.05 % NaF and 0.5 % NaF. All solutions were pH neutral, their specific conductivities are listed in Table 2.

Table 2: *Composition and specific conductivities of solutions*

Composition [wt. %]	**Specific conductivity χ [mS.cm^{-1}]**
0,9 % NaCl	15.44
0,9 % NaCl + 0,05 % NaF	16.32
0,9 % NaCl + 0,5 % NaF	24.4

Immersion tests

The specimen's shape for immersion tests was rectangular (30 mm x 80 mm x 1.5 mm). The specimen surface was not treated

(mechanically or chemically) only the edges were grinded by abrasive paper grain 600. The grease was removed by diethyl ether. The specimens were weighted out with accuracy ± 0.000 01 g (Mettler Toledo XS 205). Immersion tests were 42 days and they were carried out at elevated ambient temperature 37 ± 0.5 °C. The group of three parallel specimens was tested for each solution. After exposure the specimens were carefully brushed, washed by de-mineralized water, freely dried up and weighted out again [10, 11].

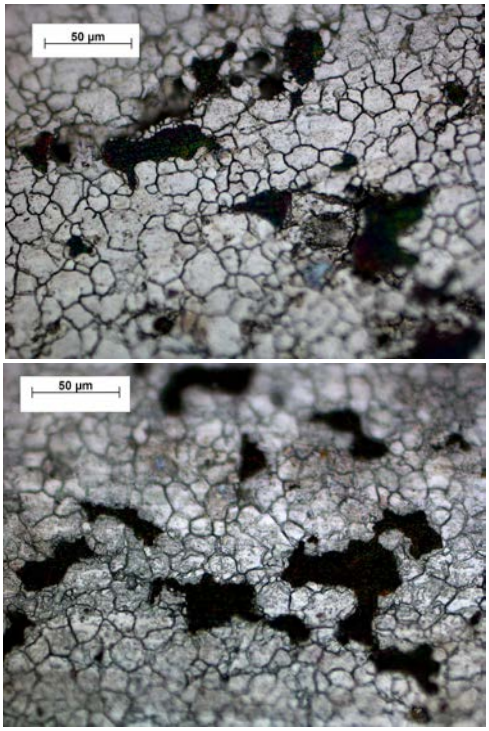
Pitted surfaces of specimens after immersion tests were observed by the optical microscope NIKON AZ 100. Average corrosion rates ($g.m^{-2}.day^{-1}$) were calculated from corrosion losses ($g.m^{-2}$) during the immersion tests.

Cyclic potentiodynamic polarization tests

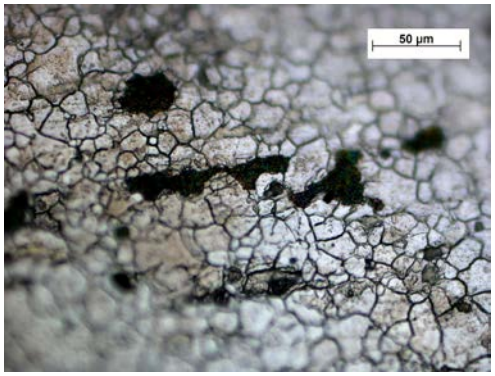
Cyclic potentiodynamic polarization tests were carried out in a three electrode cell of corrosion measuring system (VoltaLab 10 with VSP unit). Potentiodynamic polarization curves were obtained by the EC-LAB SOFT software. Potential between the sample and the electrolyte has been settled for 10 minutes before the polarization. Scan range was -0.3V – 1.2V vs the open circuit potential and the scan rate was 1mV/s. The surface of working electrode AISI 316Ti of 1 cm^2 area was not mechanically treated, only rinsed with diethyl ether before measurement. The saturated calomel electrode (SCE) was applied as the reference electrode and platinum foil as a counter electrode. All experiments were carried out at ambient temperature of 37 ± 0.5 °C**.** At least five experiment repeats were carried out for all specimens.

4. Experimental results and discussion

Tested specimens were locally damaged by pitting during immersion test. The corrosion failure was not visible to the naked eye it was visualized at a microscopic observation. As can be seen (Fig. 2), the pit's shape is generally irregular, pit's size varies. Edges of corrosion pits seem to copy austenitic grains and it points to possibility of combination of two forms of corrosion attack, pitting and intergranular corrosion [1-3, 9]. There is no marked difference between pits appearance according of fluoride content (Fig. 2), but the damaged area of specimens with the highest content of fluoride seems to be slightly smaller than in the other two cases.



a)
b)



c)

Fig. 2 *Typical shapes of pits after 42-days immersion test: a) 0.9 % NaCl, b) 0.9 % NaCl + 0.05 NaF, c) 0.9 % NaCl + 0. 5 NaF*

Average corrosion rates calculated from corrosion losses during the immersion tests in dependence on the fluoride content in solution are shown in Fig. 3. As we can see, average corrosion rates decrease with the increase of fluoride content. However the corrosion rate based on the corrosion loss cannot be generally considered as the essential factor of evaluation of pitting corrosion resistance because of non-uniform, local character of pitting. However, it helps make an idea about probable changes in the pitting corrosion kinetics [2, 10].

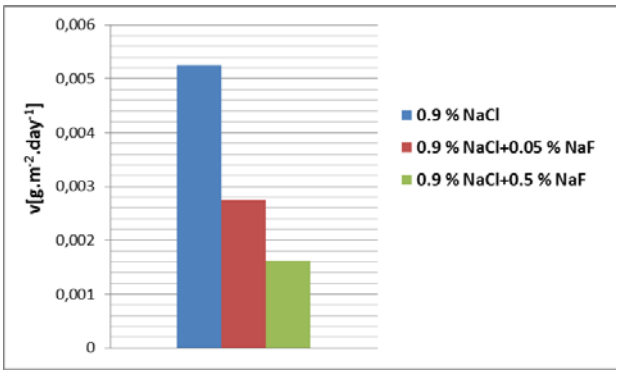


Fig. 3 *Average corrosion rates in dependence on fluoride content*

Cyclic potentiodynamic polarization curves enable determination of the pitting potential (E_p), which is an important electrochemical characteristic of the passive film quality and of the resistance to pitting. When the potential reaches this critical value, current density suddenly increases, denoting the breakdown of the passive film and the beginning of stable pit growth. The shift of E_p to more positive values on the polarization curve means the rise of stability to pitting [1, 2, 10, 11].

Cyclic potentiodynamic curves of the tested steel in three experimental solutions are shown in Fig. 4.

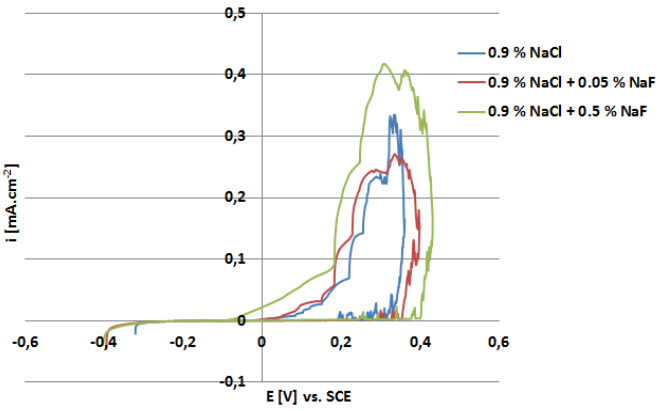


Fig. 4 *Cyclic potentiodynamic curves of AISI 316L working electrode in dependence on fluoride content in solution*

Curves are of typical lope shape with clearly observable pitting potential (located in the point of strong increase of current density). The pitting potentials E_p in dependence on fluoride content, are compared Fig. 5. E_p values (it means the resistance of passive film) increase with growing fluoride content in solution. The obtained results are consistent with authors [8], who consider fluorides the inhibitors of pitting corrosion in neutral chloride solutions.

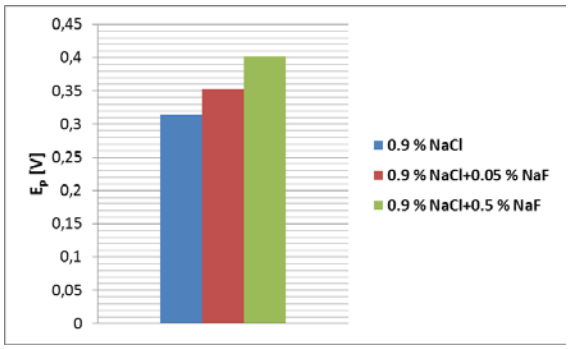


Fig. 5 *Comparison of the pitting potentials (E_p) in dependence on fluoride content in 0.9 % NaCl solution*

A fluoride inhibitive effect on local corrosion of stainless steel could be based on formation of stable metal-fluoride complexes (with higher equilibrium constants than for metal-chloride complexes) [7, 12] which may strengthen the surface passive film and prevent its breakdown.

5. Conclusions

Based on the results of performed experiments can be concluded:

- A surface of AISI 316L stainless steel was attacked by local pitting corrosion during 42 days immersion test in all experimental solutions. A corrosion failure was not visible to the naked eye it was visualized at a microscopic observation.
- Observed corrosion attack was reflected in mass losses during immersion tests. Average corrosion rates calculated from mass losses decreased with increase of fluoride content in solution.
- According to the pitting potential values determined from cyclic potentiodynamic curves, resistance of tested stainless steel to pitting corrosion increases with the growing fluoride content in 0,9 % NaCl solution.

Acknowledgements

The research was supported partially by Scientific Grant Agency of Ministry of Education, Science and Sport of Slovak Republic and Slovak Academy of Science grant VEGA No. 1/0683/15 and by project KEGA No. 044ŽU-4/2014.

References

1. SZKLARSKA-SMIALOVSKA, Z. *Pitting and crevice corrosion.* Houston, Nace, 590 p., (2005).
2. LIPTÁKOVÁ, T. *Bodová korózia nehrdzavejúcich ocelí. (Pitting corrosion of stainless steels.)* Žilina, EDIS – Žilinská univerzita, 67 p., (2009).
3. HADZIMA, B., LIPTÁKOVÁ, T. *Základy elektrochemickej korózie kovov (Fundamentals of electrochemical corrosion of metals)*, Žilina: EDIS - Žilinská univerzita, 116 p., (2008).
4. HERAVI, F., MOAYED, M. H., MOKHBER M. *Effect of Fluoride on Nickel-Titanium and Stainless Steel Orthodontic Archwires: An In-Vitro Study.* Journal of Dentistry of Tehran, vol. 12, 1, pp. 49–59, (2015).
5. GHOSH, R., SINGH, R.J., SINGH, D. D. N. *Role of fluoride in accelerating corrosion and pitting of steel in concrete environments.* Transactions- Indian Institute of Metals, vol. 56, 4, pp. 391-397, (2003).
6. BASTIDAS, J. M., FOSCA, C., CHICO, B., OTERO, E. *Corrosion behaviour of highly alloyed stainless steels in mixed chloride and fluoride aqueous solutions.* Materials and Corrosion, vol. 48, pp. 216-220, (1997).
7. CARRANZA, R. M., RODRÍGUEZ, M. A., BEBAK, R. B. *Inhibition of chloride induced crevice corrosion in Alloy 22 by fluoride ions.* Corrosion/2006 Conference and Exposition; 2006 March 12-16; San Diego, CA, USA, (2006).
8. YAMAZAKI, O. *Effect of fluoride ion on the pitting corrosion of type 304 stainless steel in neutral NaCl solution*. Zairyo-to-Kankyo, vol. 43, pp. 265-271, (1994).
9. PARDO, A., MERINO, M. C., COY, A. E., VIEJO, F., CARBONERAS, M., ARRABAL, R. *Influence of Ti, C and N concentration on the intergranular corrosion behavior of AISI 316Ti and 321 stainless steels.* Acta Materialia, vol. 55, pp. 2239-2251, (2007).
10. ZATKALÍKOVÁ, V. *Bodová korózia ocele AISI 316Ti pri rôznych prevádzkových podmienkach.* (*Pitting corrosion of AISI 316Ti at various operating conditions.*) PhD Thesis: ŽU v Žiline, Žilina, 77 p., (2008).
11. BABOIAN, R. *Corrosion Test and Standards: Aplication and Interpretation*, *ASTM Manual Series.* Philadelphia, USA, PA 19103, (1995).
12. GÁLVEZ, J. L., DUFOUR, J., NEGRO, C., LÓPEZ-MATEOS, F. *Hydrolysis of iron and chromium fluorides: mechanism and kinetics.* J. Hazard. Mater., vol. 154, 1-3, pp. 135-145, (2007).